

Copyright Undertaking

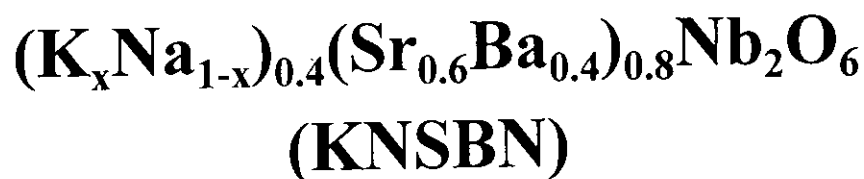
This thesis is protected by copyright, with all rights reserved.

By reading and using the thesis, the reader understands and agrees to the following terms:

1. The reader will abide by the rules and legal ordinances governing copyright regarding the use of the thesis.
2. The reader will use the thesis for the purpose of research or private study only and not for distribution or further reproduction or any other purpose.
3. The reader agrees to indemnify and hold the University harmless from and against any loss, damage, cost, liability or expenses arising from copyright infringement or unauthorized usage.

If you have reasons to believe that any materials in this thesis are deemed not suitable to be distributed in this form, or a copyright owner having difficulty with the material being included in our database, please contact lbsys@polyu.edu.hk providing details. The Library will look into your claim and consider taking remedial action upon receipt of the written requests.

Fabrication and Characterization of Sol-Gel Derived



Submitted by

Lai Brian

For The Degree of

Master of Philosophy in Physics

At

**The Hong Kong Polytechnic
University**

(February 2000)



Pao Yue-Kong Library
PolyU • Hong Kong

Acknowledgments

Firstly, I would like to thank my chief supervisor Dr. C. L. Mak for his help and fruitful discussions throughout the period of the research work. Thanks are also due to Dr. K. H. Wong for his enlightening suggestions. I wish to extend my special thanks to Dr. K. H. Pang for discussion and technical supports throughout the work. Moreover, it is my pleasure to thank Dr. Hamid TOUIR, Thin Films Group, Jobin Yvon-Sofie, France, for his help in carrying out the ellipsometry measurements. Last but not least, I would like to express my particular gratitude to my family and my teacher Mr. M. C. Chan for their support and encouragement.

Abstract

High quality potassium sodium strontium barium niobate powders and films with composition of $K_{0.2}Na_{0.2}Sr_{0.48}Ba_{0.32}Nb_2O_6$ (KNSBN) were prepared by sol-gel technique using methoxyethanol as the solvent. In the film fabrication, dip coating method was used and single crystal (100)Si wafers were employed as substrates.

The effect of different annealing temperature on the degree of crystallization of KNSBN was characterized by differential thermal analysis (DTA), thermogravimetry analysis (TGA), X-ray diffraction (XRD) and Raman spectroscopy. As a result, powders started to crystallize at temperatures as low as 600 °C and fully converted into tetragonal tungsten bronze (TTB) phase at temperatures higher than 1000 °C. On the other hand, films can be crystallized at a lower temperature of 500 °C and its orthorhombic tetragonal phase transition temperature occurred at 600 °C. These temperatures are lower than those of sol-gel derived strontium barium niobate (SBN).

The effects of sol concentration and thickness on the surface morphology of the films were measured by atomic force microscope (AFM). Small and spherical grains of uniform size distribution with no apparent grain agglomeration were observed at low sol concentration or for thin films. Increasing sol concentration or film thickness would enhance surface roughness. At the same time, the grain became bigger with a larger size distribution. As the sol concentration used is higher than 0.18 M, micro-cracks were observed on the film surfaces.

Optical properties of single layer KNSBN films were studied by ellipsometric measurements. The single layer films consisted of two different sub-layers. The upper layer of the films, composed of KNSBN and void, had a smaller refractive index and extinction coefficient than that of the lower layer which composed of KNSBN only. This indicated that the bottom layer had a higher degree of crystallinity. Besides, the refractive indices and extinction coefficients of the films were increased with the sol concentration increased. However, all the values obtained in our films were smaller than that of KNSBN single crystal. That means the density of the films were still less than that of single crystal.

Table of Contents

Acknowledgements	i
Abstract	ii
Table of Contents	iv
Table of Figures	ix
List of Table	xiv

C h a p t e r 1 Introduction

1.1 Background	1
1.2 Outline of the thesis	2
Reference 1	3

C h a p t e r 2 Theory

2.1 Characteristic of Potassium Sodium Strontium Barium Niobate	4
2.1.1 Structure of Potassium Sodium Strontium Barium Niobate	3
2.1.2 The origin of ferroelectricity	7
2.1.3 Phase transition	8
2.1.4 Other properties of KNSBN	9

2.5 Raman Spectroscopy	35
2.5.1 Historical background	35
2.5.2 Basic theory of Spontaneous Raman Scattering	36
2.5.3 Macroscopic Theory (electromagnetic view)	39
2.5.4 Microscopic Theory (quantum mechanic view)	40
2.5.5 Resonant light scattering	43
2.5.6 Conservation laws	43
2.5.7 Selection Rules	44
2.5.8 Sample identification by using Raman scattering	46
2.5.9 The interrelation between XRD & Raman Spectrum	46
2.6 Atomic Force Microscope	47
2.6.1 The principle of Atomic Force Microscope	47
2.6.2 AFM working process	48
2.7 Ellipsometry Measurement	50
2.7.1 Historical Background	50
2.7.2 Theory of ellipsometry	51
References 2	58

2.2 Preparation Method	11
2.2.1 Introduction	11
2.2.2 Sol-gel technique	15
2.2.2.1 Preparation of a homogeneous precursor solution	16
2.2.2.2 Deposition on the substrate	17
2.2.2.3 Mechanisms of hydrolysis and condensation	20
2.2.2.4 Annealing	22
2.2.3 Comparison between thin film and powders	23
2.3 Differential Thermal Analysis (DTA) & Thermogravimetry Analysis (TGA)	24
2.3.1 Principle of Differential Thermal Analysis (DTA)	24
2.3.2 Principle of Thermogravimetry Analysis (TGA)	26
2.3.3 Comparison of DTA and TGA	28
2.4 X-Ray Diffractometry	29
2.4.1 Background	29
2.4.2 Bragg Law	30
2.4.3 Miller indices	32
2.4.4 Application of X-ray diffraction	32
a) Determination of the crystal structure	33
b) Grain size measurement	33
c) Measuring the effects of constraints on the crystal structure	34

C h a p t e r 3 Experimental Aspects

3.1	Preparation of KNSBN Ceramics	63
3.1.1	Fabrication of KNSBN sol	63
3.1.2	Preparation of KNSBN powders from sol	64
3.1.3	Preparation of KNSBN films from sol	65
3.2	Thermal Analysis of KNSBN Powders	67
3.3	X-ray Diffraction Measurement	67
3.4	Raman Spectra Measurement	68
3.5	Surface Morphology	71
3.6	Optical Properties Measurement	72

C h a p t e r 4 Structural characterization

4.1	Use of improved solvent	73
4.2	Temperature effects	74
4.2.1	Powders	74
4.2.2	Films	80
4.3	Thickness effect	87
4.4	Concentration effect	94
	Reference 4	102

C h a p t e r 5 Optical characterisation

5.1	The optical properties of sol-gel derived KNSBN films	103
-----	---	-----

Reference 5		113
--------------------	--	------------

C h a p t e r 6 Conclusions

6.1	Conclusions	114
-----	-------------	-----

6.2	Suggestions for Future Work	116
-----	-----------------------------	-----

Table of Figures

Figure 2.1	Schematic diagram showing a projection of the tungsten-bronze-type structure on the (001) plane. The orthorhombic cell and the tetragonal cell are shown by solid lines and dotted lines, respectively.	5
Figure 2.2	The nature of the cation displacements along +c, relative to the mean oxygen planes, which explains the macroscopic polarization.	7
Figure 2.3	The classification of sample preparation methods.	13
Figure 2.4	Block diagram indicates the steps of sol-gel process.	15
Figure 2.5	Stages of the dip-coating process.	18
Figure 2.6	Detail of the liquid flow patterns in the deposition region. U is the withdraw speed, S is the stagnation point, δ is the boundary layer and h is the thickness of the fluid film.	18
Figure 2.7	Definition of hydrolysis, alcoxolation, oxolation and ololation.	21
Figure 2.8	Schematic diagram of classical DTA apparatus.	25
Figure 2.9	Schematic illustration of ΔT as a function of temperature.	26
Figure 2.10	Schematic single stage TG curve.	27
Figure 2.11	Geometry of X-ray diffraction.	30

Figure 2.12	Raman and Rayleigh scattering. For Stokes scattering, energy of the final state is less than the energy of the initial state when anti-Stokes scattering, the energy of the final state is greater than that of initial state. For Rayleigh scattering, the energy of initial and final states is the same.	37
Figure 2.13	Dispersion relationship of vibration mode of phonon showing the different between Raman and Brillouin scattering.	38
Figure 2.14	Raman scattering cause electronic transition. (a) intra-band transition and (b) interband transition.	42
Figure 2.15	Vector diagram for the conservation of momentum in Stokes scattering.	44
Figure 2.16	Schematic view of the force sensor for an AFM.	48
Figure 2.17	Optical path of ellipsometry.	51
Figure 2.18	Reflection and Refraction of one layer film.	52
Figure 3.1	The flow chart of synthesis route of KNSBN powders and films.	66
Figure 3.2	Experimental setup of Raman spectroscopy.	70
Figure 3.3	Schematic diagram of the atomic force microscope METRIS-2000.	72
Figure 4.1	DTA (in DSC mode) and TGA curves of $K_{0.2}Na_{0.2}Sr_{0.48}Ba_{0.32}Nb_2O_6$ powders.	75
Figure 4.2	XRD spectra of KNSBN powders annealing at different temperatures. ● is the orthorhombic BN phase and ■ is the orthorhombic SN phase.	77

Figure 4.3	Room temperature Raman spectra of KNSBN powders annealing at different temperatures. ● is the plasma line of the laser. The factor on the left of each spectrum $\times 6$ etc., means that the spectrum has been enlarged by six times compared to other spectra.	79
Figure 4.4	XRD spectra of 0.21M, 3 layers dip-coating KNSBN films annealing at different temperatures.	81
Figure 4.5	Room temperature Raman spectra for 3-layer dip-coated KNSBN films with sol concentration equals to 0.21M. Different annealing temperatures are indicated at the right of the figure. ● is the plasma line of the laser.	83
Figure 4.6	Surface morphology of 3 layers KNSBN films annealed at different temperatures. The sol concentration is 0.21M and the magnification of the optical image is 400X.	86
Figure 4.7	XRD spectrum of 10-layers KNSBN film with single annealing cycle. The sol concentration of dip coating is 0.03M, withdraw rate is 0.3 cm/sec and the annealing temperature is 700 °C for 2 hours.	87
Figure 4.8(a)	AFM image of KNSBN films with different no. of layers with single annealing cycle. The sol concentration used to dip-coating is 0.03 M and the scan area is 10 $\mu\text{m} \times 10 \mu\text{m}$.	90
Figure 4.8(b)	AFM image of KNSBN films with different no. of layers with single annealing cycle. The sol concentration used to dip-coating is 0.03 M and the scan area is 5 $\mu\text{m} \times 5 \mu\text{m}$.	91
Figure 4.9(a)	The relation between no. of layers and surface roughness. The scan area is 10 $\mu\text{m} \times 10 \mu\text{m}$	92
Figure 4.9(b)	The relation between no. of layers and surface roughness. The scan area is 5 $\mu\text{m} \times 5 \mu\text{m}$	92

Figure 4.10	The relation between no. of layer and grain size.	93
Figure 4.11	XRD spectra of single layer KNSBN films with sol concentration = 0.18 M for dip coating. The annealing temperature is 700 °C for 2 hours.	94
Figure 4.12(a)	AFM images of KNSBN single layer films with different sol concentration of (i) 0.03 M (ii) 0.06 M (iii) 0.09 M (iv) 0.12 M (v) 0.15 M and (vi) 0.18M. The scan area is 25 μm \times 25 μm .	96
Figure 4.12(b)	AFM images of KNSBN single layer films with different sol concentration of (i) 0.03 M (ii) 0.06 M (iii) 0.09 M (iv) 0.12 M (v) 0.15 M and (vi) 0.18M. The scan area is 10 μm \times 10 μm .	97
Figure 4.12(c)	AFM images of KNSBN single layer films with different sol concentration of (i) 0.03 M (ii) 0.06 M (iii) 0.09 M (iv) 0.12 M (v) 0.15 M and (vi) 0.18M. The scan area is 5 μm \times 5 μm .	98
Figure 4.12(d)	AFM images of KNSBN single layer films with different sol concentration of (i) 0.03 M (ii) 0.06 M (iii) 0.09 M (iv) 0.12 M (v) 0.15 M and (vi) 0.18M. The scan area is 2 μm \times 2 μm .	99
Figure 4.13	The relation between sol concentration and surface roughness. The scan area is (a) 25 μm \times 25 μm and (b) 10 μm \times 10 μm .	100
Figure 4.14	Relation between sol concentration and grain size. The data are based on the scan area of 5 μm \times 5 μm	101
Figure 5.1	The fitting model of KNSBN film used in the SE spectral analysis.	105
Figure 5.2	The spectra of the ellipsometric parameters I_s and I_c as function of photon energy, obtained from SE experiments for KNSBN films with sol concentration of (a) 0.03M, (b) 0.06 M, (c) 0.09M, (d) 0.12 M, (e) 0.15 M and (f) 0.18 M.	108

- Figure 5.3** The refractive index (n) of the KNSBN films, with sol concentration of 0.03 M, 0.06 M, 0.09M, 0.12 M, 0.15 M and 0.18 M obtained by the two layer amorphous model. 109
- Figure 5.4** The extinction coefficient (k) of the KNSBN films, with sol concentration of 0.03 M, 0.06 M, 0.09M, 0.12 M, 0.15 M and 0.18 M obtained by the two layer amorphous model. 110
- Figure 5.5** The relation between sol concentration and the fitted thickness of the films. 113

List of Tables

Table 1	Pyroelectric, piezoelectric and electro-optic properties of KNSBN, PLZT and LiNbO_3 single crystals.	9
Table 2	Comparison of the advantages, disadvantages and applications of typical ceramics single crystals, powders and films.	12
Table 3	Summary of the features of XRD spectra of KNSBN powders.	76
Table 4	Summary of the features of Raman spectra of KNSBN powders.	80
Table 5	FWHM of XRD diffraction peaks as a function of temperature.	82
Table 6	The variation of peak position of the Raman bands at different annealing temperatures.	84

Chapter 1

Introduction

1.1 Background

Ferroelectric materials have prominent dielectric, ferroelectric, piezoelectric and pyroelectric properties. They have been explored to manufacture various kinds of devices such as ferroelectric memories cells [1.1], piezoelectric or electro-acoustic sensors [1.2], pyroelectric detectors [1.3] and optical waveguide devices [1.4]. The application of these properties in a new generation of devices has driven the intensive studies on the synthesis, characterization and determination of processing-property relationships of ferroelectric materials.

Of various ferroelectric materials studied, potassium sodium strontium barium niobate (KNSBN) received a great deal of attention owing to its high pyroelectric figures of merit (FM_{RV}) and high threshold energy for optical damage. The FM_{RV} of $(K_{0.5}Na_{0.5})_{0.4}(Sr_{0.6}Ba_{0.4})_{0.8}Nb_2O_6$ is 8×10^{-13} Cm/J, which is about two to five times larger than La doped $PbZr_{1-x}Ti_xO_3$, one of the most commonly used pyroelectric materials [1.5, 1.6]. The threshold energy for laser damage of KNSBN crystals is 618 MW/cm² [1.6] which is almost 3 times larger than quartz. On the other hand, KNSBN has a very good electro-optics coefficient. For example, the effective linear electro-optics coefficient of $K_{0.2}Na_{0.2}Sr_{0.48}Ba_{0.32}Nb_2O_6$ is 59×10^{-12} m/V which is three folds larger than that of $LiNbO_3$ [1.6, 1.7], one of the most commonly used electro-optic materials. Therefore fabrication and characterization of KNSBN polycrystals are of great interest. Despite these important properties of the KNSBN ceramics, very few experimental work of preparing KNSBN powders or films has been

reported [1.8]. In this thesis we will demonstrate that both KNSBN powders and films of good structural quality can be fabricated by the sol-gel method.

Sol-gel technique is perhaps the most versatile, inexpensive and convenient method for preparing ferroelectric ceramics. Advantages of the sol-gel technique for powders and thin film processes include excellent homogeneity, ease of chemical composition control, high purity, low processing temperature, film uniformity over large area and versatile shaping. Furthermore, sol-gel process is a suitable method for fabricate high-quality films of a few microns thick which are difficult to prepare by physical deposition methods.

1.2 Outlines of the thesis

This thesis is divided into six chapters. In chapter 1, a brief introduction describing the previous work on this field is presented. The structural and some physical properties of KNSBN are given in Chapter 2. In addition, the details of the sol-gel processing will also be reviewed. The qualities of the samples have been examined and investigated by different characterization techniques (differential thermal analysis and thermogravimetry analysis, X-ray Diffraction, Raman spectroscopy, atomic force microscope and spectroscopic ellipsometry). The principles of these measurements are presented individually in five different sections of Chapter 2 respectively. After that, the preparation procedures as well as the experimental procedures of all the characterization measurements stated above are reviewed in Chapter 3. The results and discussion of these structural and optical characterization studies are presented in chapter 4 and 5 respectively. The last part of this thesis is the conclusion of this project. Some suggestions for further study are also recommended.

References 1

- [1.1] Orlando Auciello, James F. Scott and Ramesh, "The Physics of Ferroelectric Memories". *Physics Today*, 51:7, American Institute of Physics, New York, pp.22-27 (1998).
- [1.2] S. Trolier-McKinstry and R.E. Newnham, "Sensors, Actuators and Smart Materials". *Materials Research Bulletin*, 28:4, Pergamon Press, New York, pp.27-33 (1993).
- [1.3] F. Jin, G.W. Auner and R. Nail, "Giant effective pyroelectric coefficients from graded ferroelectric devices". *Applied Physics Letters*, 73, pp.2838-2840 (1998).
- [1.4] David K. Fork, Florence Armani-Leplingard and John J. Kingston, "Application of Electroceramic Thin Films to Optical Waveguide Devices". *Materials Research Bulletin*, 31:7, Pergamon Press, New York, pp.53-58 (1996).
- [1.5] Yuhuan Xu, "Perovskite-type ferroelectric: part II". *Ferroelectric Materials and Their Applications*, Elsevier Science Publishers B.V., Asterdam; New York : North-Holland, p.174 and 192(1991).
- [1.6] Yuhuan Xu, "Ferroelectric tungsten-bronze-type niobate crystals". *Ferroelectric Materials and Their Applications*, Elsevier Science Publishers B.V., Asterdam; New York : North-Holland, p.267(1991).
- [1.7] Yuhuan Xu, "Methods for measuring the physical properties of ferroelectric materials". *Ferroelectric Materials and Their Applications*, Elsevier Science Publishers B.V., Asterdam; New York : North-Holland, p.83(1991).
- [1.8] Yuhuan Xu, Ching Jih Chen, Ren Xu and John D. Mackenzie, "Ferroelectric Thin Films on Silicon and Fused Silica Substrates by Sol-Gel Process". E.R. Myers and A.I. Kingon, *Ferroelectric Thin Films Symposium*, San Francisco, 16-20th April, pp.13-18 (1990).

Chapter 2

Theory

2.1 Characteristic of Potassium Sodium Strontium Barium Niobate

Potassium sodium strontium barium niobate (KNSBN) is a well-known ferroelectric material having large electro-optic, pyroelectric and pizeoelectric coefficients [2.1]. Before studying this material, we would first try to understand its structural as well as other physical properties. In this section, we will discuss the structure of KNSBN, the origin of its ferroelectricity, the phase transition and some characteristics of this material.

2.1.1 Structure of Potassium Sodium Strontium Barium Niobate

Potassium sodium strontium barium niobate $(K_yNa_{1-y})_z(Sr_xBa_{1-x})_{1.2-z}Nb_2O_6$, which belongs to the class of oxygen octahedral ferroelectrics, has the crystallographic structure similar to that of the tetragonal tungsten bronze-type K_xWO_3 and Na_xWO_3 ($x < 1$) [2.2]. This tetragonal unit cell shown in Figure 2.1 composes of BO_6 octahedra linking together through their corners in such a manner that three different kinds of void are formed and run through the whole structure parallel to the c-axis. The lattice parameters of the unit cell are $a = b = 12.5 \text{ \AA}$ and $c = 3.95 \text{ \AA}$ which satisfy the equation $a = \sqrt{10} c$. The site occupancy formula of this material can be written as $(A1)_2(A2)_4(C)_4(B1)_2(B2)_8O_{30}$ and it provides three kinds of

site for the cations occupied. In the case of complete occupied KNSBN structure, Sr^{2+} and Ba^{2+} ions can at most occupy five of the six A sites (two A1 sites and four A2 sites) when the original unfilled A site(s) is(are) occupied by the Na^+ and K^+ ions [2.3]. Since Ba^{2+} and K^+ ions have larger atomic radius than Sr^{2+} and Na^+ ions respectively, Ba^{2+} and K^+ ions prefer the larger pentagonal A2 sites while Na^+ ions prefer smaller tetragonal A1 sites. Nb^{5+} ions occupy the ten B sites (eight B1 sites and two B2 sites) and the four C sites are left as empty due to the requirement of electroneutrality and crystallographic constrains [2.4, 2.5].

For completely occupied KNSBN structure that involve $\text{Nb}_2\text{O}_6^{2-}$ ($\text{Nb}_{10}\text{O}_{30}^{10-}$), the constrain of stoichiometric ratio of KNSB : Nb is very important. Since there are only 6 occupied sites for all K^+ , Na^+ , Sr^{2+} and Ba^{2+} ions to occupy when there are 10 occupy sites for the Nb^{5+} ions, the stoichiometric ratio of KNSB : Nb must be 6 : 10 or 1.2 : 2 for completely occupied structure. This suggest that, for completely occupied KNSBN, when the values of x and y in the formula $(\text{K}_y\text{Na}_{1-y})_z(\text{Sr}_x\text{Ba}_{1-x})_{1.2-z}\text{Nb}_2\text{O}_6$ are less than 1, the stoichiometric ratio of KN : SB must be z : 1.2-z (z range from 0 to 1.2) and not the others [2.6]. It also implies that break down of this constrains given non-fulfill or excess doped TTB KNSBN structure.

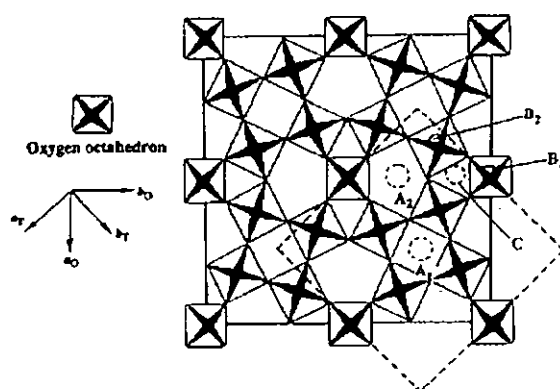
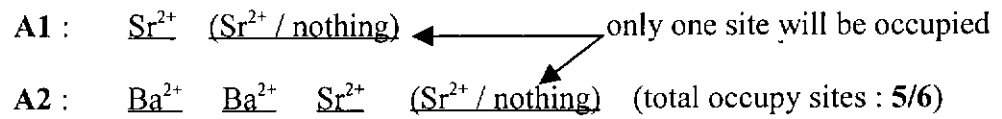


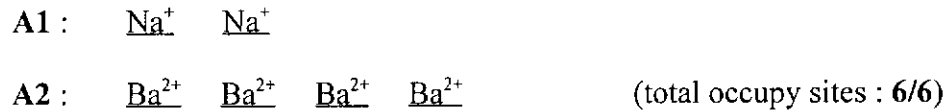
Figure 2.1 Schematic diagram showing a projection of the tungsten-bronze-type structure on the (001) plane. The orthorhombic cell and the tetragonal cell are shown by solid lines and dotted lines, respectively [2.4].

Another important point about KNSBN structure is that it has an intermediate structure between SBN and BNN with modified potassium ions [2.5]. It is easy to understand this by consider the occupy situation of SBN, BNN and KNSBN as follow :

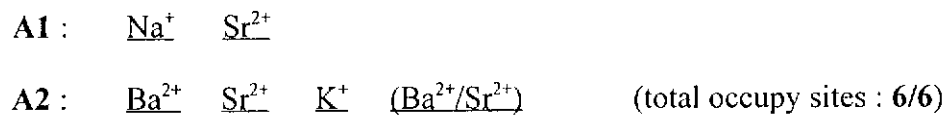
For **SBN**, let take $\text{Sr}_{0.6}\text{Ba}_{0.4}\text{Nb}_2\text{O}_6$ ($\text{Sr}_3\text{Ba}_2\text{Nb}_{10}\text{O}_{30}$) as an example. The occupied situation of A1 and A2 sites is



For **BNN**, let take $\text{Ba}_{0.8}\text{Na}_{0.4}\text{Nb}_2\text{O}_6$ ($\text{Ba}_4\text{Na}_2\text{Nb}_{10}\text{O}_{30}$) as an example. The occupied situation of A1 and A2 sites is



Then for **KNSBN**, let take $\text{K}_{0.2}\text{Na}_{0.2}\text{Sr}_{0.48}\text{Ba}_{0.32}\text{Nb}_2\text{O}_6$ ($\text{KNaSr}_{2.4}\text{Ba}_{1.6}\text{Nb}_{10}\text{O}_{30}$) as an example. The occupy situation of A1 and A2 sites is



Therefore it is easy to see that one or two Ba^{2+} ion(s) in A2 sites and one Na^+ ion in the A1 sites of BNN appear in the A1 and A2 sites of KNSBN. Also, some ions occupied in the A1 and A2 sites of SBN appear in that of KNSBN. The Sr^{2+} ion(s) occupied in both A1 and A2 sites and the Ba^{2+} ions occupied in A2 sites of SBN seem to fill up the vacant. Besides, the present of the K^+ ions occupied in the A2 sites of KNSBN modified its properties [2.6]. This structural property let us to expect that KNSBN contain partial properties of SBN and BNN.

2.1.2 The origin of ferroelectricity

The ferroelectric crystal of KNSBN classified as the polar class $4mm$ with the space symmetry group $P4bm$. When the crystal is put in the temperature below the Curie temperature (T_C), the material change its phase from paraelectric to ferroelectric. In this ferroelectric phase, all the metallic ions displaced along the tetragonal polar axis. These atomic displacements in these metallic ions relative to the centrosymmetric oxygen planes induce spontaneous polarization. This is the origin of ferroelectric character in tungsten-bronze KNSBN. Compare with SBN, KNSBN shows more signified ferroelectric behavior. Since only strontium ions, barium ions and niobium ions in SBN materials take place of atomic displacement but the present of potassium ions and sodium ions in KNSBN materials also involved in the displacement action. Figure 2.2 show the diagram that illustrates the origin of the macroscopic polarization in KNSBN [2.7].

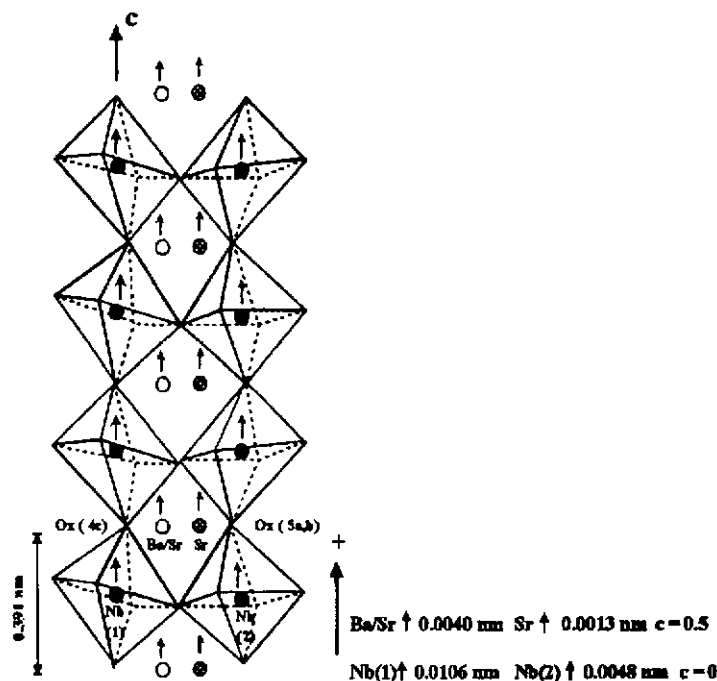


Figure 2.2 The nature of the cation displacements along $+c$, relative to the mean oxygen planes, which explains the macroscopic polarization [2.7].

2.1.3 Phase transition

When the materials are heated above a certain temperature range, the crystals become paraelectric and show no ferroelectric behavior. This temperature usually referred to as the Curie range. The Curie temperature of KNSBN is higher than other ferroelectric materials such as LiNbO_3 , BaTiO_3 , and SBN. For BaTiO_3 , the Curie temperature is 393K while it is 312K for $\text{Sr}_{0.75}\text{Ba}_{0.25}\text{Nb}_2\text{O}_6$ [2.8, 2.9]. Nevertheless, the Curie temperature of KNSBN is 475K [2.1]. This suggests that KNSBN would maintain its ferroelectric properties at a higher temperature.

Besides, the broadening (smearing) of the phase transition of a complete occupied KNSBN may be narrower than that of SBN. Since altogether only five of six interstitial A1 and A2 sites are filled by strontium and barium ions in SBN, the structure has a high degree of disorder due to these incompletely filled sites. As a result, the unit cells become dissimilar and the parameters specifying the ferroelectric properties of each crystal cell are different. This fluctuation smears the phase transition. However, all the A1 and A2 sites of complete occupied KNSBN are fully engaged by K^+ , Na^+ , Sr^{2+} and Ba^{2+} ions, therefore the disorder effect due to unfilled sites is not existed. Hence the effect of phase transition broadening becomes non-significant in KNSBN. Nevertheless, there should be still some disorder effect due to randomly fill of K^+ , Na^+ , Sr^{2+} and Ba^{2+} ions.

2.1.4 Other properties of KNSBN

Nowadays, KNSBN crystals have been used as electro-optic and pyroelectric detector materials. The advantages to select this material are that it contains high electro-optic, piezoelectric and pyroelectric coefficients and relative small dielectric coefficient. Table 1 shows the electro-optics, pyroelectric and piezoelectric coefficients of $(K_{0.5}Na_{0.5})_{0.4}(Sr_{0.6}Ba_{0.4})_{0.8}Nb_2O_6$, $Pb_{0.92}La_{0.07}(Zr_{0.62}Ti_{0.38})_{0.98}O_3$ and $LiNbO_3$ for comparison [2.1, 2.10, 2.11, 2.12, 2.13].

	KNSBN	PLZT	LiNbO ₃
Refractive index (n_0)	2.31	2.5-3.0	2.2860
Effective linear electro-optic coefficient (r_e)	$59 \times 10^{-12} \text{ m/V}$	$433 \times 10^{-12} \text{ m/V}$	$20 \times 10^{-12} \text{ m/V}$
Pyroelectric coefficient (ρ)	$2.7 \times 10^{-8} \text{ C/cm}^2\text{K}$	$6 \times 10^{-8} \text{ C/cm}^2\text{K}$	$8.3 \times 10^{-9} \text{ C/cm}^2\text{K}$
Piezoelectric coefficient (d_{33})	$70 \times 10^{-12} \text{ C/N}$	$710 \times 10^{-12} \text{ C/N}$	$6 \times 10^{-12} \text{ C/N}$
Dielectric constant (κ)	220	2590	30
Figure of merit ($\rho/\sqrt{\kappa}$)	$1.9 \times 10^{-9} \text{ C/cm}^2\text{K}$	$1.18 \times 10^{-9} \text{ C/cm}^2\text{K}$	$1.54 \times 10^{-9} \text{ C/cm}^2\text{K}$

Table 1 Pyroelectric, piezoelectric and electro-optic properties of KNSBN, PLZT and LiNbO₃ single crystals.

Another advantage of KNSBN is that, when the KNSBN crystals are doped with ions, semi-conducting ferroelectric (or photoferroelectric) KNSBN will be formed. These crystals have excellent controllable photo-conductive and photo-refractive effects. These crystals show sensitive photo-refractive properties and possess a great potential for applications in holographic memories, image storage devices and optical phase-conjugation devices [2.10].

Besides, the threshold energy for the laser damage of KNSBN crystals is quite high (618 MW/cm^2) . This makes KNSBN crystals attractive for high-power laser modulator applications [2.14].

2.2 Preparation Method

In the last section, we have discussed about some general characteristics of KNSBN. However, the actual properties of the material would strongly depend also on the final product from which is restricted by the fabrication method. In this section, we will compare the different forms of ferroelectric samples and different synthesis methods. Then we will explain how and why sol-gel method is selected to fabricate powders and films in our studies.

2.2.1 Introduction

Ferroelectric materials are usually synthesized in three different forms, namely, single crystal, powders and films. The advantages, disadvantages and general applications of these three different forms of ferroelectric materials are summarized in Table 2.

In general, single crystal have the best structural properties and hence the ferroelectric, piezoelectric and pyroelectric properties. It is because the lattice of single crystal is the most regular one, so most physical properties can be enhanced without any internal suppression. Nevertheless, single crystals normally have large size and are expensive to fabricate.

On the other hand, powder is easy to fabricate, low cost, and can be pressed into bulk form. The advantages of powders are good stress resistance, allowance of complex shape fabrication and some properties will be enhanced if the powders are in nano-meter particle size. These property-enhancements are due to the quantum effect of zero dimension. Nano-size powders can be used to synthesis 0-3 composite matrix for pyroelectric detector and nonlinear optics applications.

For the demand of the world market, devices with minimized size, large geometrical flexibility, low cost but with the same functional output as single crystal are essential. To meet these requirements, high quality films seem to be one of the solutions. There are two kinds of film: thin film and thick film. Thin films are usually used as low voltage devices whereas thick films are normally applied in high voltage one.

	Single Crystals	Powders	Films
Advantages	1. Good structural properties 2. Good electrical properties 3. Good magnetic properties	1. Low cost . Can be fabricated in bulk form of complex shape 3. Have Quantum effects of nano-powders	1. Low cost 2. minimized size . Large geometrical flexibility
Disadvantages	1. large size 2. high cost to fabricate	Less application	Weak singal given out when compare with single crystal
Applications	Any physical device	1. pyroelectric detector 2. nonlinear optics applications	1. thin films---low voltage devices 2. thick films---high voltage devices

Table 2 Comparison of the advantages, disadvantages and applications of typical ceramics single crystals, powders and films.

Normally, there are many methods for preparing ceramics samples and they can be classified into two main streams of physical or chemical ways. Physical methods include evaporation and sputtering. Chemical methods are subdivided into three groups, namely, gas-phase reactions, liquid precursor and mixed oxide route. For gas-phase reactions, it includes chemical vapor deposition (CVD), metallorganic chemical vapor deposition (MOCVD), directed metal oxidation and reaction bonding. For liquid precursor methods, the two main processes are sol-gel processing and polymer pyrolysis. For mixed oxide route methods, melt casting is one of this kind of method [2.15]. Figure 2.3 shown the classification of preparation methods.

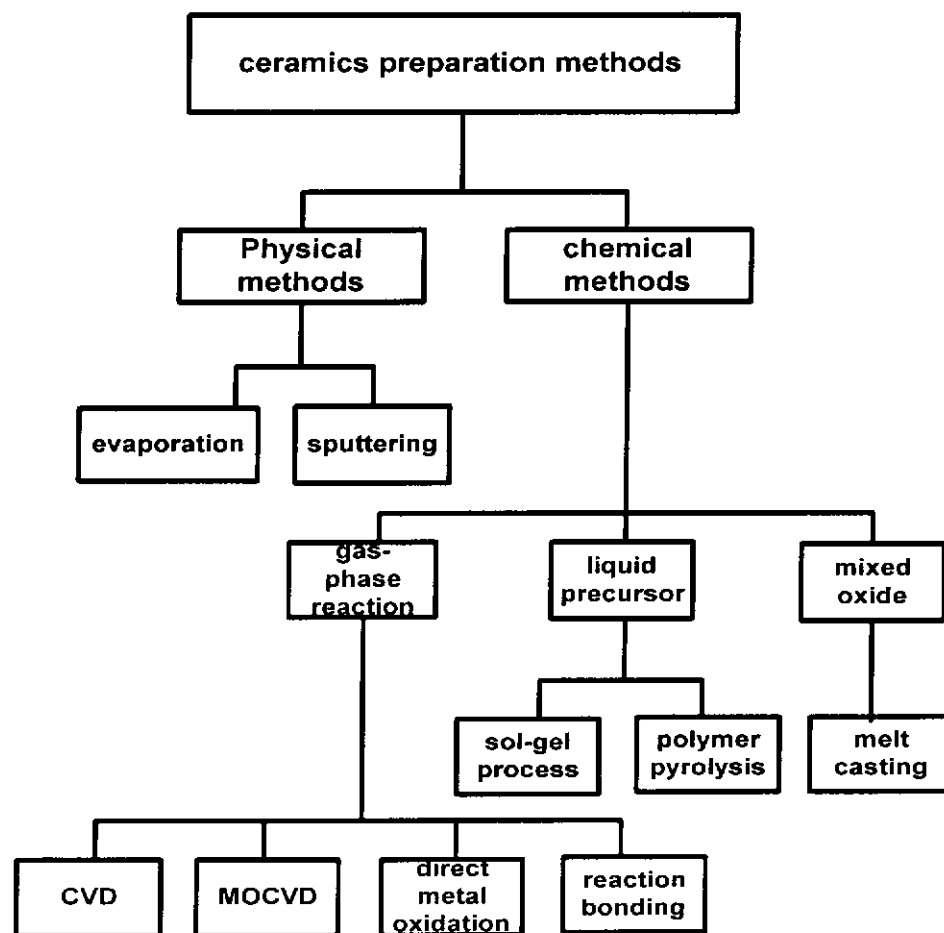


Figure 2.3 The classification of sample preparation methods

The most widely used deposition technique for synthesis ferroelectric thin films is physical vapor deposition processes. However, it is, in general, very difficult to controll the crystal structure, microstructure and uniformity of the films [2.15].

On the other hand, CVD or MOCVD techniques can overcome the problem of controlling the crystal structure. Nonetheless, it cannot control the stoichiometry of the complex compositions of typical ferroelectric materials [2.15].

Furthermore, the methods stated above can be used to fabricate films only. For powder preparations, one of the most convenient methods is mix-oxide route. However, this method needs high temperature, hence it will lead to large energy consumption and high cost [2.15].

Since both films and powders are needed in our studies, technique that can be used to synthesis both good quality films and nano-size powders is required. Among various preparation techniques, sol-gel processing seems to be the best way. Firstly, sol-gel method can be used to synthesis both powders and films. Secondly, the processing has the advantages of good homogeneity, easy composition control and low annealing temperature. It also allows to fabricating large area and crack-free thin films [2.16]. Finally, the equipment used for the sol-gel preparation is inexpensive, so it can overcome the problems associated with physical vapor deposition process and mix-oxide route.

2.2.2 Sol-gel technique

Sol-gel process is a wet-chemical method to fabricate metal oxide based ferroelectric materials. It involves two important stages of sol and gel that can be subdivided into four or five steps depend on whether the final product is film or powder [2.15]. Figure 2.4 indicates the different stages of sol-gel processing.

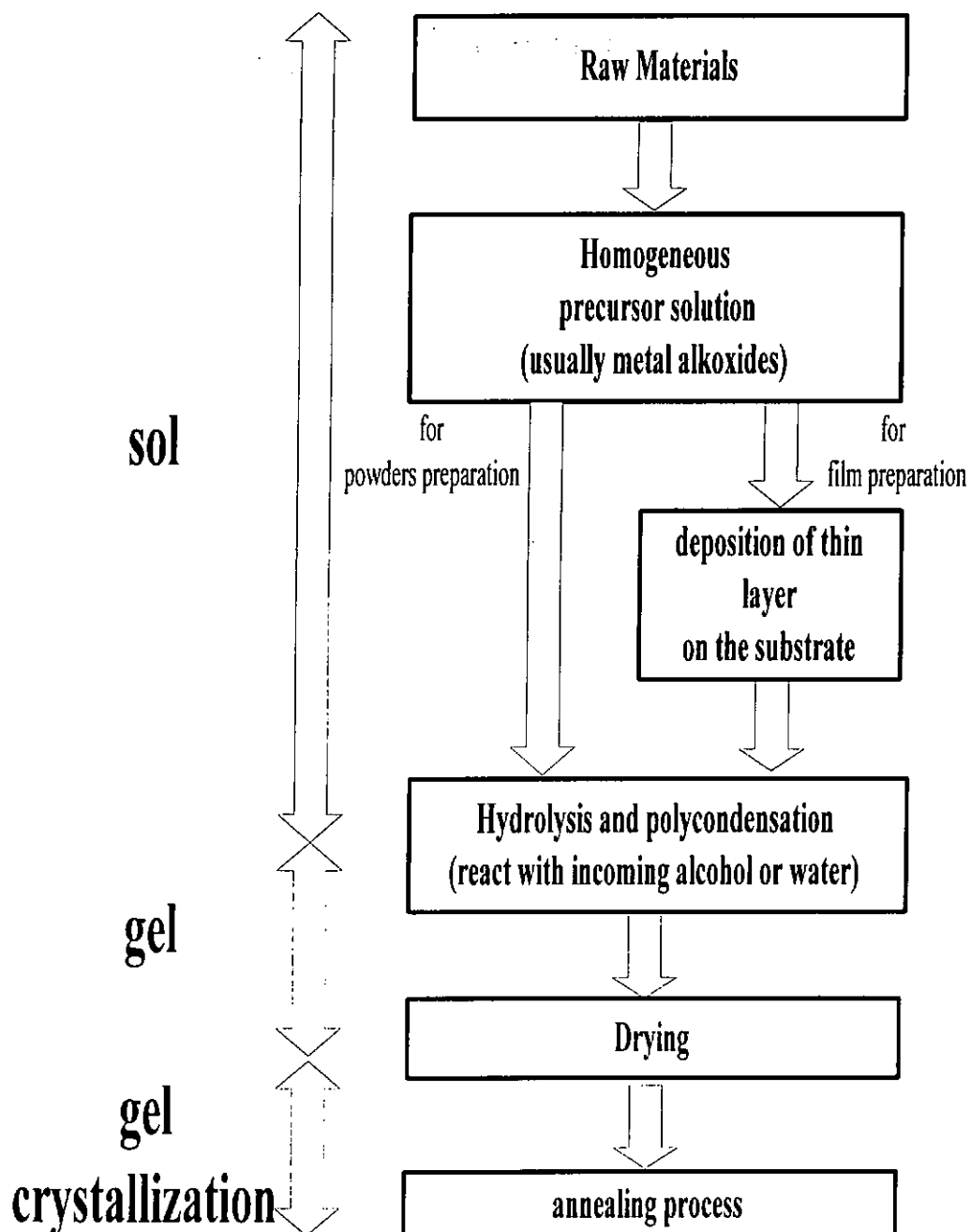
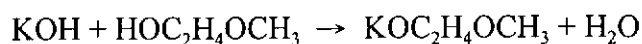
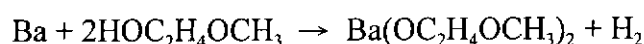


Figure 2.4 Block diagram indicates the steps of sol-gel process.

2.2.2.1 Preparation of a homogeneous precursor solution

There are two methods to prepare precursor solutions. One is to use inorganic precursor and the other metal alkoxide. Since it is easier to control the rate of hydrolysis and condensation in the case of metal alkoxides, this route is adopted in our studies. However, synthesis of metal alkoxide depends on the electronegativity of the metals. For highly electropositive elements with valences up to three, such as Na, K, Sr and Ba used in our study, they react directly with the alcohol, accompanied by liberating of hydrogen to form metal alkoxides. In particle, pure metal and metallic elements like Na or K are not to be selected as the raw materials because of the safety reason. Metal hydroxides are often used instead and water is liberated after the reaction.



On the other hand, for highly electronegative elements, the reaction usually involves their covalent halides with appropriate alcohol.



For synthesis multi-component oxides, individual metal alkoxide are first prepared separately. Then these alkoxides are mixed together with a common solvent, usually the parent alcohol. After reflux, a homogeneous solution is formed [2.17].

2.2.2.2 Deposition on the substrate

For this film fabrication, the prepared precursor solution are required to coat onto the substrates. This can be achieved by spin-coating or dip-coating techniques. Spin-coating method is more complicated and requires a spinner machine. Dip-coating method, on the other hand, is much simpler and needs no additional equipment. Throughout our work, we have used dip-coating to prepare all our film samples [2.18].

Dip-coating process can be divided into five stages: immersion, start-up, deposition, drainage, and evaporation as shown in Figure 2.5. For volatile solvents like alcohol, steps of start-up, deposition, drainage and evaporation normally process at the same time. When the substrate is immersed into the solution, some of the liquid paste onto the substrate. While the dipped film started to move up from the liquid surface, the liquid near the substrate boundary split into two kinds of motion. The inner layer moves upward with the substrate, while the outer layer returned to the bath. At this stage, there are totally six forces competed each other and these six forces govern the thickness of the films. Figure 2.6 shown the liquid patterns in the deposition region [2.19].

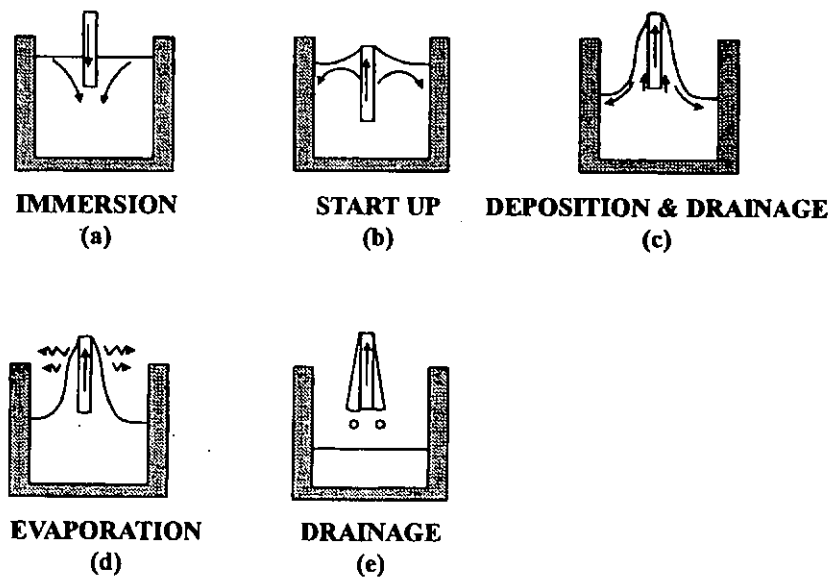


Figure 2.5 Stages of the dip-coating process.

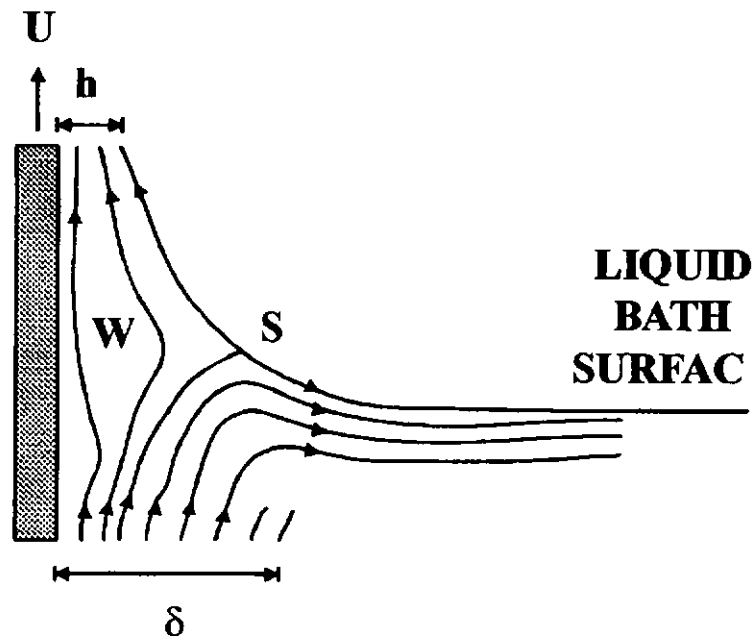


Figure 2.6 Detail of the liquid flow patterns in the deposition region. U is the withdraw speed, S is the stagnation point, δ is the boundary layer and h is the thickness of the fluid film.

When studying films, important parameter is the thickness of the film (h). For dip coating, the thickness is controlled by the force of (1) viscous drag upward on the liquid by the moving substrate, (2) force of gravity, (3) resultant force of surface tension in the concavely curved meniscus, (4) inertial force of the boundary layer liquid arriving at the deposition region, (5) surface tension gradient, and (6) the disjoining or conjoining pressure [2.19]. However, when the liquid viscosity (η) and substrate speed (U) are high enough, the major forces governing the film thickness are just the viscous drag and force of gravity. For coated liquid state at equilibrium, the viscous drag ($\propto \eta U/h$) and the gravity force (ρgh) balance each other, that is:

$$c_1 \left(\frac{\eta U}{h} \right) = \rho gh \quad (2.1)$$

rearranging this equation, the thickness of the film can be estimated as:

$$h = c_2 \left(\frac{\eta U}{\rho g} \right)^{\frac{1}{2}} \quad (2.2)$$

where the proportionality constant, c_2 , is about 0.8 for Newtonian liquids [2.19].

Some modification should be made before using equation (2.2) to estimate film thickness. The modification involve not too high substrate speed as well as liquid viscosity, shrinkage of the film due to evaporation and partial sintering and not pure Newtonian liquid of sol-gel solution. So, after modification, equation (2.2) becomes

$$h = 0.944 \left(\frac{\rho - \rho_\sigma}{\rho_f - \rho_\sigma} \right) \left(\frac{\eta U}{\gamma_{lv}} \right)^{\frac{1}{6}} \left(\frac{\eta U}{\rho_f g} \right)^{\frac{1}{2}} \quad (2.3)$$

where γ_{lv} is the liquid-vapor surface tension, ρ_f is the full density of final solid film, ρ is the density of the solution and ρ_σ is the density of the solvent [2.18].

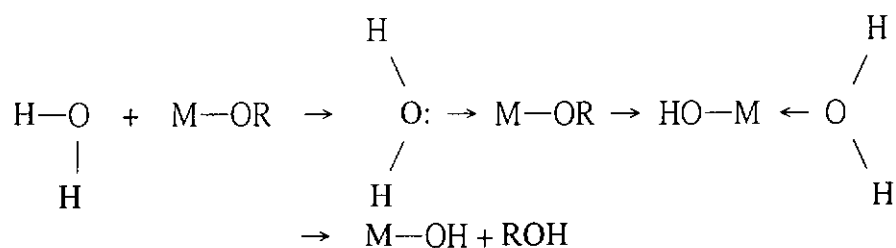
From equation (2.3), we can see that the thickness of the final film is proportional to $(\eta U)^{\frac{2}{3}}$, that is the viscosity of the solution (the concentration of the

solution) and the withdrawing speed of the substrate.

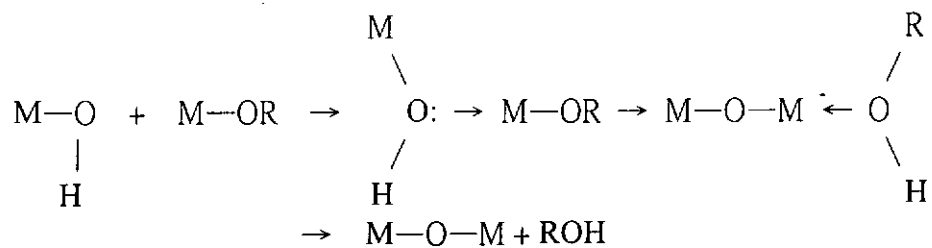
2.2.2.3 Mechanisms of hydrolysis and condensation

For both powders and films, the next processes are hydrolysis and condensation. The basic idea of both reactions can be easily described as follows [2.20]. When the metal alkoxide contacts with water, multi-steps reaction occurred. As a result, metal hydroxide or metal oxide together with alcohol or water will be given out.

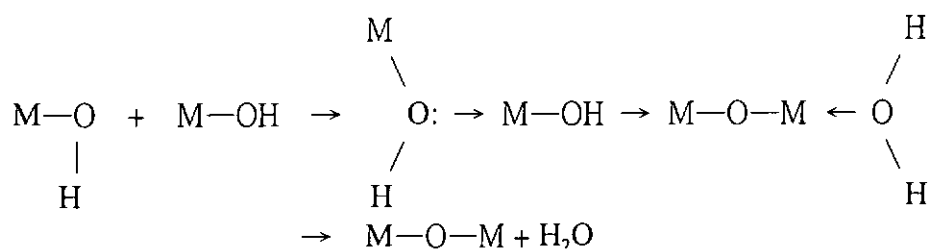
In the absence of catalyst, both hydrolysis and condensation are taken place by means of nucleophilic substitution (S_N). This is the reaction that the oxygen of the incoming water or metal hydroxide attacks the metal alkoxide --- nucleophilic addition (A_N). After then, the following reactions depend on whether it is a hydrolysis process or condensation process. If it is the hydrolysis process, the proton of the attacking molecule transfers to the metal alkoxide or hydroxo-ligand within the transition state. At last, the protonated species are removed as either alcohol (alcoxolation) or water (oxolation). If it is a condensation process, the product of the nucleophilic addition (A_N) will react with the starting agent, the metal hydroxide, and the product of M_2OH formed. This kind of reaction called olation. The mechanisms of hydrolysis, alcoxolation, oxolation and olation are shown in Figure 2.7.



hydrolysis

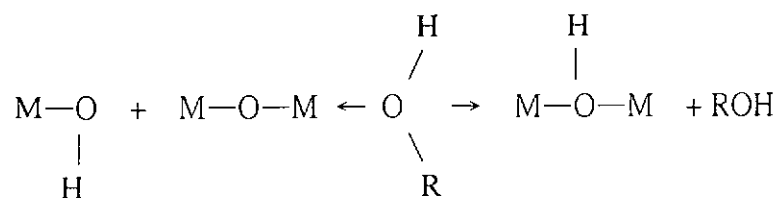


alcoxolation



oxolation

When $N-z > 0$, condensation can occur by olation:



olation

Figure 2.7 Defination of hydrolysis, alcoxolation, oxolation and olation.

The kinetics of the proton transfer mechanism is determined by the extent of coordination undersaturation of the metal, $N-z$, and the transfer ability of the proton. Larger values of $(N-z)$ and greater acidities of the proton would reduce the associated activation barriers and thus enhance the kinetics. On the other hand, the thermodynamics of olation depend on the strength of the entering nucleophile and the electrophilicity of the metal. The kinetics of olation are systematically fast partly because $(N-z) > 0$.

2.2.2.4 Annealing

The last step of sample preparation is annealing. It is the process that crystallizes the samples from amorphous gel. During the annealing process, structural evolution occurred. The evolution can be classified into three stages. First, when the annealing temperature reaches to a particular value, the gel has loss its weight and shrunk a little. This weight loss is due to the evaporation of the physical absorbed water and it leads to an endothermic reaction. The slight shrinkage of the gel is the result of increasing surface energy when weight loss occurred. As a result, the strain of the sample change to

$$\varepsilon = \frac{(1 - \nu)S\rho_s\Delta\gamma}{E} \quad (2.4)$$

where S is the surface area of the gel; ρ_s is the sketetal density; $\Delta\gamma$ is the change in specific surface energy; ν is the Poisson's ratio and E is the Young modulus of the sketeton [2.21].

When the annealing temperature continues to increase, the concurrent weight loss and shrinkage occurred at another region. This weight loss is mainly attributed by the removal of organic solvent. Also, at this stage, continued desorption and dehydroxylation occurred and this increase the surface energy, γ , by about two times of that of origin value. As the temperature continues to increase up to T_g , the sample melt and the shrinkage as well as weight loss occurred.

2.2.3 Comparison between thin films and powders

Although both powders and films are fabricated through the same process, it has slight difference. For films, the steps of dip-coating, hydrolysis and condensation, and drying are usually take place at the same time when the film is just withdrawn from the liquid surface. For powders, hydrolysis and condensation can only occur efficiency when a lot of water is added to the precursor solution. The reason for this difference is that, for the films, only little solution is attached on the substrate, so the water vapour in air is enough for activate the kinetics action of nucleophilic addition. However, for powders fabrication, the amount of precursor solution required is large. Therefore, plenty of water is needed for the mechanism to start.

2.3 Differential Thermal Analysis (DTA) & Thermogravimetry Analysis (TGA)

In previous sections we have introduced the structural properties and fabrication method of KNSBN. In this and the following sections, we will present some experimental techniques that were used in our study to characterise the KNSBN powders and films. First, we will introduce the differential thermal analysis (DTA) and thermogravimetry analysis (TGA) techniques. These methods are useful for measuring the thermal properties of the samples. Next, we will describe the theory of x-ray diffraction and Raman spectroscopy which are essential for measuring the structural characteristic of the samples. Then, the principle of atomic force microscope (AFM) and how it can yield information on the surface roughness and grain size will be discussed in section 2.6. Finally, the principle of variable angle spectroscopic ellipsometry (VASE) will be given in section 2.7. This VASE technique allows us to measure the optical properties of the thin films.

2.3.1 Principle of Differential Thermal Analysis (DTA)

Differential thermal analysis (DTA) is a technique that can detect the phase transition of the measured sample. The structure of a classical DTA is illustrated in Figure 2.8 [2.22]. The sample and a reference material are put in the center of the furnace that are at the ends of the thermocouple. The reference material selected must be thermally inert. That means the material exhibits no phase change over the temperature range of the experiment. When the temperature of the furnace is increased using the temperature controller, both the temperatures of the sample and reference material increases. The temperature difference of these two objects is measured through the computer. As the sample temperature reach a particular value

such that the sample has a phase change, for example, evaporate of solvent, crystallization or melting, thermal energy will be either absorbed or emitted. The temperature increment of the sample cannot be maintained at steadily rate. Therefore, the temperature difference between the sample and the reference material will have sudden change. Form the anomalies in DTA curve, we can obtain the crystallization or melting temperature. Figure 2.9 show the DTA curve of typical ceramic materials.

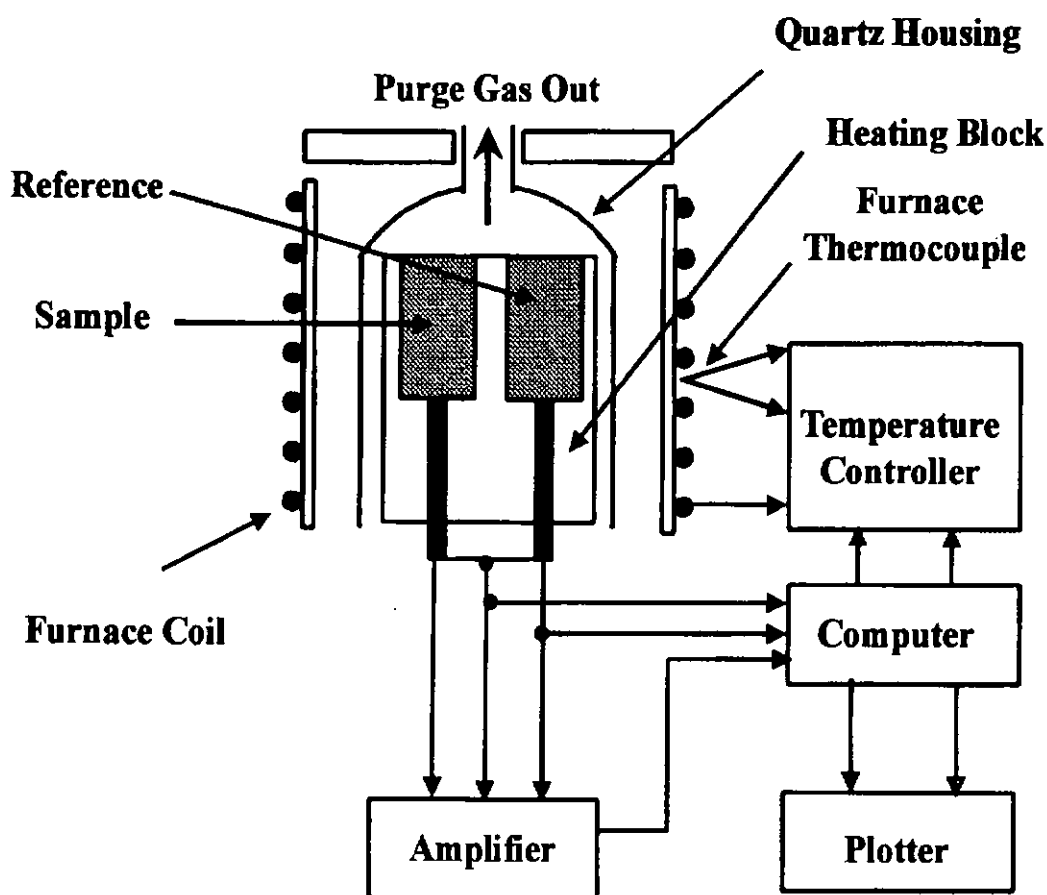


Figure 2.8 Schematic diagram of classical DTA apparatus.

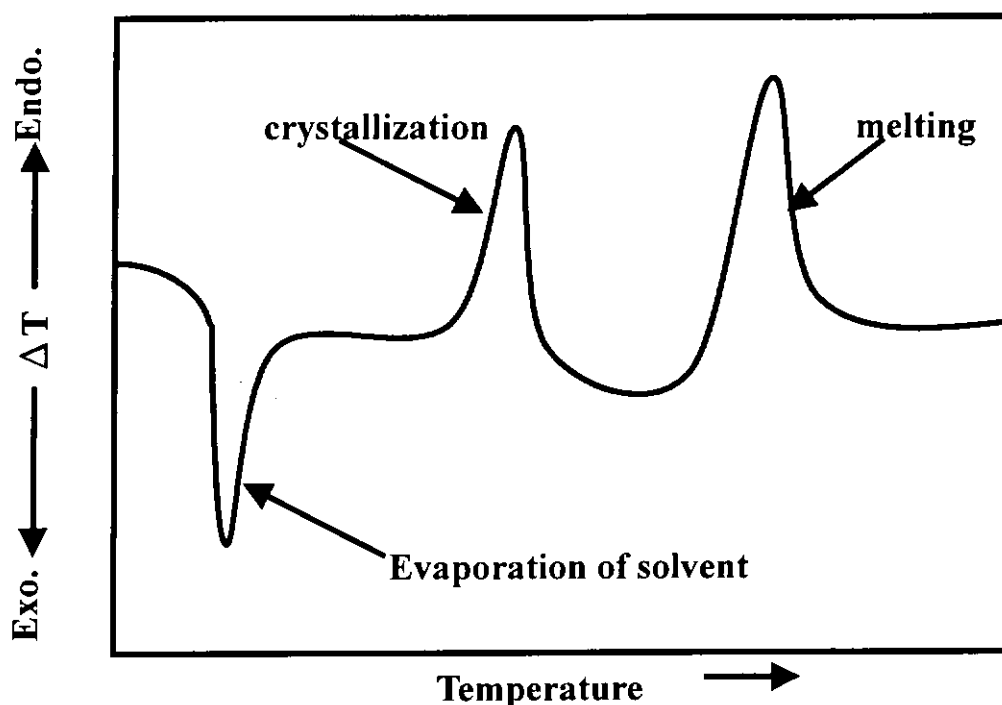


Figure 2.9 Schematic illustration of ΔT as a function of temperature.

2.3.2 Principle of Thermogravity Analysis (TGA)

Thermogravity Analysis (TGA) is another kind of thermal analysis that measures the mass change of a sample with increasing temperature. Some events, such as, melting, crystallization and glass transition, do not have mass change. On the other hand, desorption, vaporization, oxidation and decomposition have mass change [2.23]. The reason of this weight loss is very simple. When the sample is heated up to a particular temperature, the solvent and the water inside the sample have enough energy to evaporate. When the temperature further increased, the elements inside the material also have enough energy to decompose and will be gotten away from the sample. Different solvent and element require different energy for evaporation or deposition, therefore, more than one weight loss will be occurred.

TG curve represents the mass change as the function of temperature.

Normally, the vertical axis of the graph refers to the percentage change of the mass while the horizontal axis set as temperature. Figure 2.10 show a typical TG curve with one-stage reaction process. From the figure, we can see that the reaction is characterized by two turning points which correspond to two temperatures: T_i and T_f which are the procedural decomposition temperature and the final temperature respectively. These two temperatures tell us at which temperature the reaction start (T_i) and complete (T_f).

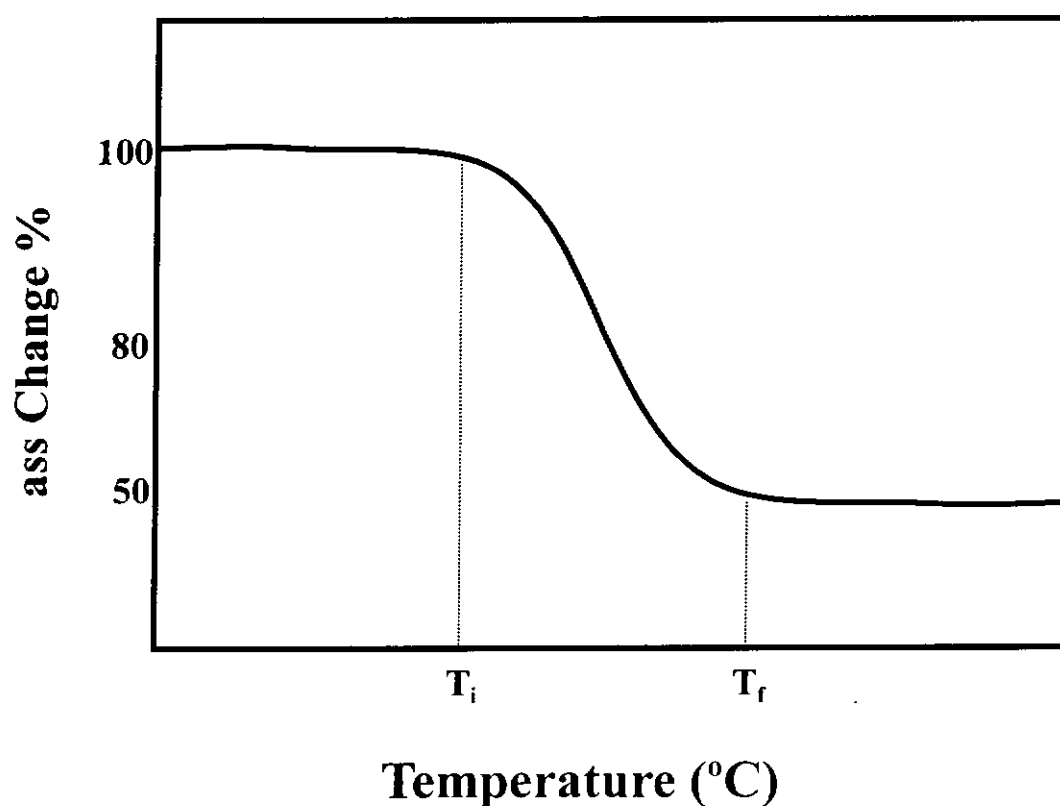


Figure 2.10 Schematic single stage TG curve.

2.3.3 Comparison of DTA and TGA

Although both DTA and TGA give us the information on the phase transition of the measured object, TGA has two drawbacks. TGA cannot detect the phase transition of crystallization and melting of the sample which is very important for structural analysis of the sample. In addition, the mass change characteristics of a material are strongly dependent on the experimental conditions such as the physical quantities of the sample, the shape and the nature of the sample holder and the pressure of the atmosphere in the sample chamber. Despite these disadvantages, TGA given a good choice for comparison of other thermal experiment result. As this reason, many TA instrument manufactures offer simultaneous TG-DTA apparatus so that the experimental conditions for TGA and DTA are identical. In this case, the given data can be directly compared [2.23].

2.4 X-Ray Diffractometry

X-rays diffractometry (XRD) is usually used in studying the structural properties of material. In this section, we will talk about the background and the principle of x-ray, and how it can be applied to determinate the crystal structure as well as the crystalline grain size.

2.4.1 Background

X-ray was first found by Wilhelm Conrad Röntgen in 1895 when he found his photographic plates, which were kept carefully in his laboratory, became fogged. Then he put the photographic plates to a high voltage gas-discharge tube. He found that this tube emitted a radiation that could penetrate anything and then he called it X-ray because he cannot determinate this radiation was a stream of particles or a train of waves [2.24].

Until 1912, Max von Laue suggested an idea to explain this phenomena. He proposed that when a collimated X-ray beam was fallen on a crystal that are made up of regular pattern of atoms. These atoms would set as the diffraction centers and the diffraction beam would result as constructive interference in particular directions. However, the mathematical interpretation to support this explanation was still complicated, while the knowledge of atomic arrangement was still not fully understand at that moment [2.25].

In 1914, Sir William Bragg and Sir Lawrence Bragg started to study the atomic structure of crystal by X-ray diffraction. They found that there were some planes which contributed by the atoms could reflect the X-ray beam like that of mirror. This discovery built up the concept of atomic plane and lead to a well-developed theory of X-ray diffraction. They proposed that the X-ray which have high energy and with wavelength in order of atomic spacing could scattering in all directions by the electrons inside a crystal when the beam was impinged on this crystal. Since this scattered beam signal was strong, we can easy to detect [2.25].

Nowadays, we know that X-ray is one kind of electromagnetic wave that can be produced by accelerating the electrons of a heated filament using a potential difference and strike a metal target. In general, x-ray can be used to determinate the structure of material or used in medicine application for body checking.

2.4.2 Bragg Law

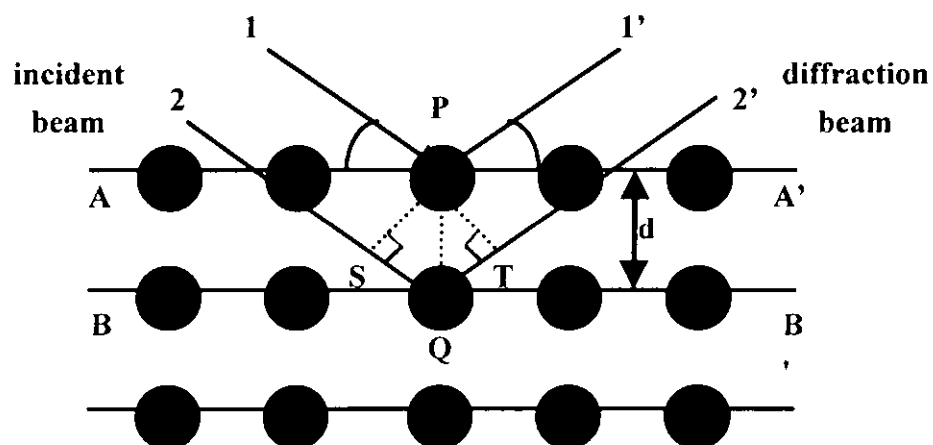


Figure 2.11 Geometry of X-ray diffraction.

From Figure 2.11, we can see that the optical path of beam 2-2' is longer than that of beam 1-1'. This path difference, δ , can be written as [2.26]:

$$\delta = SQ + QT = PQ \cos \phi_1 + PQ \cos \phi_2 \quad (2.5)$$

where ϕ_1 represents $\angle PQS$ and ϕ_2 represents $\angle PQT$. After simplify equation (2.5),

$$\delta = 2PQ \cos\left(\frac{\phi_1 - \phi_2}{2}\right) \cos\left(\frac{\phi_1 + \phi_2}{2}\right) \quad (2.6)$$

Since,

$$PQ = d ; \quad \phi_1 = \phi_2 \quad \text{and} \quad \phi_1 + \phi_2 = 180^\circ - 2\theta \quad (2.7)$$

therefore, the optical path difference can be written as

$$\delta = 2d \sin \theta \quad (2.8)$$

Since δ is independent of ϕ_1 and ϕ_2 , this equation can be applied to all reflected rays scattered from two adjacent planes. As a result, interference of the diffracted rays is occurred. The constructive interference only occurs when the path difference δ is equal to an integral number of wavelengths. That is :

$$n\lambda = 2d \sin \theta \quad (2.9)$$

where n is the order of the Bragg reflection and λ is the wavelength of X-ray. If we consider only the first order reflection, equation (2.9) can be rewritten as

$$\lambda = 2d \sin \theta \quad \text{or} \quad \frac{\lambda}{2d} = \sin \theta \quad (2.10)$$

Since $\sin \theta$ cannot exceed unity, the condition for diffraction at any observable angle 2θ is

$$\lambda \leq 2d \quad (2.11)$$

2.4.3 Miller indices

The interplaner spacing d stated in the above section can be related to 3 numbers called the Miller indices. These parameters are usually used to represent the direction of the crystal plane. For example, consider the case of a crystal with cubic structure [2.27],

$$d = \frac{a}{\sqrt{h^2 + k^2 + l^2}} \quad (2.22)$$

where (h,k,l) is the Miller indices of the crystal. Besides cubic structure, there are totally six more kinds of crystal lattice cells.

Typically, X-ray diffraction can occur for the unit cells having atoms only stated at the cell corners (with particular Miller indices). However, when some doped ions or impurities state at the face or interior unit cell position, these ions or impurities then act as extra scattering centers. As a result, the origin constructive interference at particular direction will become destructive. Hence, some peaks originally indicated in the X-ray spectra become absence. That is just one important application of X-ray diffraction measurement which can lead us to understand the structure of the crystal [2.28].

2.4.4 Application of X-ray diffraction

The main application of X-ray diffraction is material identification. Equipment called X-ray diffractometer just provides this kind of function. Typical material investigations include measurement of crystallographic orientation of single crystal, chemical composition identification, residual determination and crystal size visualization.

a) Determination of the crystal structure

Since the Miller indices of many kinds of structure are well-known, to compare the peak positions of the experimental X-ray spectra with the standard reference and indexing it to see whether the peaks are well-defined is a possible work. Hence, the orientation of the measured sample can be obtained [2.29].

b) Grain size measurement

Normally, for X-ray diffraction, only the signal at the exact Bragg's angle is strong enough for detection. The signal near the Bragg's angle is weak because of the cancellation of the reflective beam that diffracted from other crystal planes. However, for decreasing of the particle size, the number of atomic plane decreases and not all the reflected rays cancelled each other. As a result, some reflective rays superpose on the strong signal. Hence, peak broadening occurs. This effect is called the particle size effect of peak broadening [2.30].

The grain size of the crystal can be calculated as follows. According to the Scherrer formula [2.30], the particle diameter or the grain size (t) of the peak can be written as

$$t = \frac{c\lambda}{B \cos \theta} \quad (2.13)$$

where λ is the wavelength of X-ray, θ is the Bragg angle, c is the shape factor that usually takes a value of 0.9 and B is the full width half maximum intensity (FWHM) measured in radian. However, this equation only satisfies for the case of high-angle reflections from a narrow x-ray source. Warren, therefore, redefined B as $\sqrt{B_M^2 - B_S^2}$, where B_M is the breadth of the observed diffraction line at FWHM and B_S is the instrumental broadening or breadth of a peak from a specimen that

exhibits no broadening beyond inherent instrument peak width. Both of the broadening is assumed to have a Gaussian shape. After the modification, the equation of (2.13) becomes:

$$t = \frac{0.9\lambda}{\sqrt{B_M^2 - B_S^2} \cos \theta} \quad (2.14)$$

c) Measuring the effects of constraints on the crystal structure

Besides, XRD can also detect the effect of stress on the crystal. For instance, if the lattice constant of the substrate is smaller than the coated material, the cell of the sample might be forced to shrink and its lattice parameters would be altered. This change of the lattice pattern can be observed through the XRD spectrum for the enhancement of some peak intensities or for the shift of the peak positions [2.31].

2.5 Raman Spectroscopy

Beside X-ray diffraction, Raman spectroscopy is another technique that can be used to identify the structure of the measured samples. To understand the principle of Raman scattering, it must understand the historical background of light scattering first. Therefore, in this section, we talk about the historical background before the discussion of Raman scattering theory. Since Raman scattering can be divided into spontaneous and resonant scattering, we will initial discuss about the spontaneous scattering by mean of macroscopic view (electromagnetic approach) and microscopic view (quantum mechanic approach). Then we will simply introduce the resonant light scattering, the conservation laws of Raman scattering and application of how Raman scattering as sample identification tool will be presented. At last, we will compare the differences among XRD and Raman scattering

2.5.1 Historical background

Elastic light scattering was first investigated by Tyndall in 1868 [2.32]. He observed that white light was partly polarized when it was scattered by very fine particles, at 90° from the incident light. Lord Rayleigh followed his earlier work and treated the scattering of light by spherical particles. After making some assumptions, Rayleigh's law was built up in 1899 [2.33],

$$I_s = I \frac{9\pi^2 N \nu^2}{2\lambda^4 r^2} \left(\frac{\kappa - \kappa_0}{\kappa + 2\kappa_0} \right)^2 (1 + \cos^2 \phi) \quad (2.15)$$

where I is the intensity of the unpolarized incident light, N is the number of the scattering particles of volume ν , r is the distance to the point of observation, ϕ is

the angle through which the light with wavelength λ is scattered, κ is the relative permittivity of scattering light and κ_0 is the relative permittivity of the media. This law shows that the scattered light intensity is depended on λ^{-4} .

In 1922, Brillouin did some calculation on the spectrum of the light scattered by density waves in liquid, and first theoretically developed the subject of inelastic light scattering. After one year, Smekal extended this fundamental work to two quantized energy level system. As a result, the concept of elementary excitations would produce shift in the frequency of the scattered photon was predicated [2.34].

Inelastic light scattering was first observed experimentally by Raman in 1928. He observed that the light scattered by liquid benzene contains sharp sidebands in pairs symmetrically disposed around the incident frequency with shifts identical to the frequencies of some of the infrared vibrational lines. At the same year, Landsberg and Mandelstam observed similar phenomenon in quartz. These results concluded that inelastic scattering of light come from molecular and crystal vibrations and this phenomenon is known as Smekal-Raman effect or Raman scattering [2.34].

2.5.2 Basic theory of Spontaneous Raman Scattering

When the sample is irradiated by intense light, an incident photon of energy $\hbar\omega_L$ interacts with elementary excitations within the system and raises the energy of the system to an intermediate state of different energy. The system then relaxes to a lower stationary state with the emission of a photon. The energy of the final state may be less or greater than the energy of the initial state. The process is called Stokes or anti-Stokes scattering respectively. The frequency shift $|\omega_L - \omega_S|$, also called the Raman shift, is characteristic of the excitations that occur in the sample since $\hbar\omega_S$ refer to the excited energy of the molecule within the system [2.35]. Figure 2.12 shown different scattering when the photon incident and interacts with the sample.

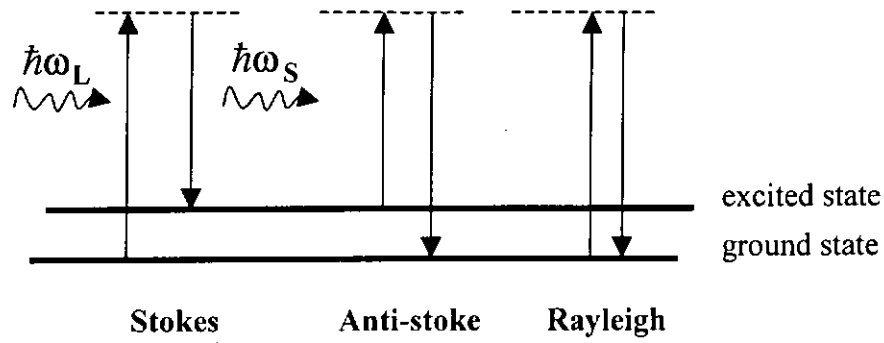


Figure 2.12 Raman and Rayleigh scattering. For Stokes scattering, energy of the final state is less than the energy of the initial state when anti-Stokes scattering, the energy of the final state is greater than that of initial state. For Rayleigh scattering, the energy of initial and final states is the same.

In general, Stokes and anti-Stokes scattering yield equivalent information, and since Stokes scattering intensities are normally stronger, Stokes spectra are often sufficient and preferred. However, anti-Stokes information is important when the temperature associated with particular mode of vibration phonon is need to be determined. Since the ratio of the frequency width of anti-Stoke peak ($d\omega_{\text{anti-Stokes}}$) to that of Stoke ($d\omega_{\text{Stokes}}$) with particular frequency (ω) can relate to the number of mode of vibration (n) by,

$$\frac{d\omega_{\text{anti-Stokes}}}{d\omega_{\text{Stokes}}} = \frac{n(\omega)}{n(\omega) + 1} \quad (2.16)$$

Here, according to the Bose-Einstein factor, we have

$$n(\omega) = \frac{1}{e^{\frac{\hbar\omega}{k_0 T}} - 1} \quad (2.17)$$

where k_0 is the Boltzmann's constant and T is the temperature associated to particular mode of vibration phonon. Therefore the temperature of particular mode of

vibration phonon can be found [2.36].

One difference between Raman scattering and Brillouin scattering is that Raman shift of normal material is in the range of 5 cm^{-1} to 4000 cm^{-1} while Brillouin shift is usually less than 5 cm^{-1} . This implies that Brillouin scattering can be used to measure the energy change of acoustic phonon near the center of Brillouin zone where Raman scattering can probe the energy change of optical mode instead. Figure 2.13 shown the dispersion relation of optical branch and acoustic branch [2.37].

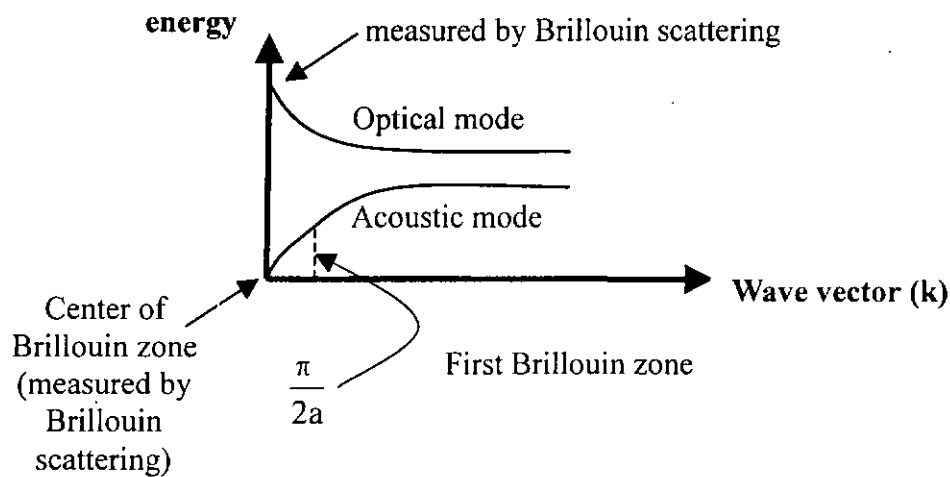


Figure 2.13 Dispersion relationship of vibration mode of phonon showing the different between Raman and Brillouin scattering.

2.5.3 Macroscopic Theory (electromagnetic view)

Raman scattering can be explained according to classical theory [2.38]. Strong light source with electric field strength (E) and angular frequency (ω_L) can be written as :

$$E = E_L \cos(\omega_L t) \quad (2.18)$$

where E is the vibrational amplitude of the light source. If a diatomic molecule is irradiated by this light, and for linear optic, an electric dipole moment P is induced,

$$P = \alpha E = \alpha E_L \cos(\omega_L t) \quad (2.19)$$

Here, α is the polarizability. Generally, α can be expanded in a Taylor series as a function of the nuclear displacement q :

$$\alpha = \alpha_0 + \left(\frac{\partial \alpha}{\partial q} \right)_0 q + \frac{1}{2} \left(\frac{\partial^2 \alpha}{\partial q^2} \right)_0 q^2 + \dots \quad (2.20)$$

The cross section of Raman effect is usually defined as [2.39]:

$$I_s = N \frac{\hbar \omega_s^4 \eta_s}{2m\omega_R c^4 \eta_L} \left(\frac{\partial \alpha}{\partial q} \right)^2 I_L dz d\Omega \quad (2.21)$$

where I_s is the intensity scattered at the Stokes frequency, ω_s , in the length interval dz and within solid angle $d\Omega$, N is the number density of scatterers, I_L is the incident intensity at the source frequency, ω_R is the material vibration radial frequencies, m is the reduced mass of vibration, η is the refractive indexes of the material and $d\alpha/dq$ is the normal mode derivative of the polarizability tensor. Therefore, for Raman effect, it is only necessary to consider the first derivative term of equation (2.20). It is a term correspond to one phonon spontaneous Raman effect when the higher derivative terms are correspond to more phonons spontaneous Raman effect. Also, treating the molecular vibration as simple harmonic motion, we have

$$q = q_0 \cos(\omega_R t + \phi) \quad (2.22)$$

Then combining equations (2.19), (2.20) and (2.22), the induced dipole moment can

be written as :

$$\begin{aligned}
 \mathbf{P} &= \left[\alpha_0 + \left(\frac{\partial \alpha}{\partial \mathbf{q}} \right)_0 \mathbf{q}_0 \cos(\omega_R t + \phi) \right] \mathbf{E}_L \cos(\omega_L t) \\
 &= \alpha_0 \mathbf{E}_L \cos(\omega_L t) + \frac{1}{2} \left(\frac{\partial \alpha}{\partial \mathbf{q}} \right)_0 \mathbf{q}_0 \mathbf{E}_L \cos[(\omega_L - \omega_R)t + \phi] + \\
 &\quad \frac{1}{2} \left(\frac{\partial \alpha}{\partial \mathbf{q}} \right)_0 \mathbf{q}_0 \mathbf{E}_L \cos[(\omega_L + \omega_R)t + \phi]
 \end{aligned} \tag{2.23}$$

The first term of (2.23) represents an oscillating dipole that radiated energy exactly the incident frequency (Rayleigh), while the second and the third terms represent the radiated energy of beat frequency $(\omega_L - \omega_R)$ and $(\omega_L + \omega_R)$, i.e. Stokes and anti-Stokes Raman shift respectively. Hence $\left(\frac{\partial \alpha}{\partial \mathbf{q}} \right)_0$ must not be zero for the vibration

that is Raman active; or the Raman effect depends on a change of induced dipole moment [2.35].

2.5.7 Microscopic Theory (quantum mechanic view)

To further understand the mechanism of light scattering, quantum-mechanical approach will be required. The Hamiltonian of the coupled radiation field and scattering medium, which refers to the energy of the scattering part, can be written as [2.40]:

$$\mathbf{H} = \mathbf{H}_e + \mathbf{H}_i + \mathbf{H}_{ei} + \mathbf{H}_p + \mathbf{H}_{ep} + \mathbf{H}_{ip} \tag{2.24}$$

where \mathbf{H}_e , \mathbf{H}_i and \mathbf{H}_p are the Hamiltonian of the electrons, the ions and photons respectively. \mathbf{H}_{ei} , \mathbf{H}_{ep} and \mathbf{H}_{ip} represent the electron-ion, electron-photon and ion-photon interaction respectively. It is customary to treat part of this equation exactly and the rest by perturbation theory. Under the adiabatic approximation, $\mathbf{H}_e + \mathbf{H}_i + \mathbf{H}_{ei}$ is renormalized into \mathbf{H}_e' . Then $\mathbf{H}_e' + \mathbf{H}_p + \mathbf{H}_{ep} + \mathbf{H}_{ip}$ can be solved to obtain the

exciton-polariton states. The photons, the photon-electron and the photon-ion interactions arising from the adiabatic approximation are then treated by perturbation theory. Generally, consideration of all parts of Hamiltonian is required, however, the main effect for Raman shift is due to the electron-photon interaction. Thus, to consider the electron-photon interaction and try to find out the kinetic energy of the electron that differ from which no photon interact with, the quantive result of Raman scattering can be obtained. For the electron-photon interactions, based on the expression for the energy inside the scattering medium (electromagnetic field energy), the electric-field operator $\hat{\mathbf{E}}(\mathbf{r})$ and the vector potential operator $\hat{\mathbf{A}}(\mathbf{r})$ are defined [2.40]:

$$\hat{\mathbf{E}}(\mathbf{r}) = \sum_{\mathbf{k}} \left[\frac{\omega(\mathbf{k})}{2V\epsilon_0\omega(\mathbf{k})} \right]^{\frac{1}{2}} \left(\mathbf{a}_{\mathbf{k}} e^{i\mathbf{k}\cdot\mathbf{r}} + \mathbf{a}_{\mathbf{k}}^{\dagger} e^{-i\mathbf{k}\cdot\mathbf{r}} \right) \hat{\mathbf{e}}_{\mathbf{k}} \quad (2.25)$$

$$\hat{\mathbf{A}}(\mathbf{r}) = \sum_{\mathbf{k}} \left[\frac{1}{2V\epsilon_0\omega(\mathbf{k})} \right]^{\frac{1}{2}} \left(\mathbf{a}_{\mathbf{k}} e^{i\mathbf{k}\cdot\mathbf{r}} + \mathbf{a}_{\mathbf{k}}^{\dagger} e^{-i\mathbf{k}\cdot\mathbf{r}} \right) \hat{\mathbf{e}}_{\mathbf{k}} \quad (2.26)$$

where $\mathbf{a}_{\mathbf{k}}^{\dagger}$ and $\mathbf{a}_{\mathbf{k}}$ are the operators of photon creation and annihilation respectively and the $\hat{\mathbf{e}}_{\mathbf{k}}$ is polarization vectors of the electric field. Then using equation (2.26), the kinetic energy of the electron, that is contributed by the momentum of electron itself and the vector potential of the external photon, can be found as follow :

$$\begin{aligned} & \frac{1}{2} \sum_{\mathbf{J}} [\mathbf{p}_{\mathbf{J}} + \mathbf{A}(\mathbf{r}_{\mathbf{J}})]^2 \\ &= \frac{1}{2} \sum_{\mathbf{J}} \mathbf{p}_{\mathbf{J}}^2 + \frac{1}{2} \sum_{\mathbf{J}} \mathbf{A}^2(\mathbf{r}_{\mathbf{J}}) + \frac{1}{2} \sum_{\mathbf{J}} \mathbf{p}_{\mathbf{J}} \mathbf{A}(\mathbf{r}_{\mathbf{J}}) + \frac{1}{2} \sum_{\mathbf{J}} \mathbf{A}(\mathbf{r}_{\mathbf{J}}) \mathbf{p}_{\mathbf{J}} \\ &= \frac{1}{2} \sum_{\mathbf{J}} \mathbf{p}_{\mathbf{J}}^2 + \mathbf{H}_{\text{er}}'' + \mathbf{H}_{\text{er}}' \end{aligned} \quad (2.27)$$

where \mathbf{J} runs over all electrons. Therefore the electron-photon Hamiltonian has two terms, \mathbf{H}_{er}'' (quadratic term) and \mathbf{H}_{er}' (linear term) in the electromagnetic field. These two terms describe the effect of Raman shift. The expression for \mathbf{H}_{er}'' and \mathbf{H}_{er}' in terms of $\mathbf{a}_{\mathbf{k}}^{\dagger}$ and $\mathbf{a}_{\mathbf{k}}$ are easily obtained from equations (2.25) and (2.26)

$$H_{cr}'' = \sum_J \frac{1}{2V\epsilon_0\omega_S^{1/2}\omega_L^{1/2}} (\hat{\mathbf{e}}_S \cdot \hat{\mathbf{e}}_L) e^{i(\bar{\mathbf{k}}_L - \bar{\mathbf{k}}_S) \cdot \hat{\mathbf{r}}} \quad (2.28)$$

$$H_{cr}' = \sum_J \frac{1}{(2V\epsilon_0)^{1/2}} \left[\begin{aligned} &\omega_L^{-1/2} a_{\mathbf{k}L} e^{i\bar{\mathbf{k}}_L \cdot \hat{\mathbf{r}}} \hat{\mathbf{e}}_L \cdot (\bar{\mathbf{p}}_J + \frac{1}{2}\bar{\mathbf{k}}_L) + \\ &\omega_S^{-1/2} a_{\mathbf{k}S}^+ e^{i\bar{\mathbf{k}}_S \cdot \hat{\mathbf{r}}} \hat{\mathbf{e}}_S \cdot (\bar{\mathbf{p}}_J - \frac{1}{2}\bar{\mathbf{k}}_L) \end{aligned} \right] \quad (2.29)$$

where $\hat{\mathbf{e}}_L$ and $\hat{\mathbf{e}}_S$ are the unit vector along the direction of incident light and scattered light respectively. Thus $\mathbf{k}_L - \mathbf{k}_S$ in equation (2.28) represent the wavevector \mathbf{q} . For scattering of light by crystal, the value of \mathbf{q} is small when compare with the Brillouin zone boundary wavevector. This implies that frequency change after scattering is very small and hence the initial and final band states after one scattering process (one electronic transition) are the same. So, it is an intra-band transition. This constrain is not present in the equation (2.29) and this suggest that scattering leads to different band states transition is allowed. This kind of transition is called inter-band transition and its plays a more important role than the quadratic part for contribute phonon scattering. Figure 2.14 shown this two kind of transitions.

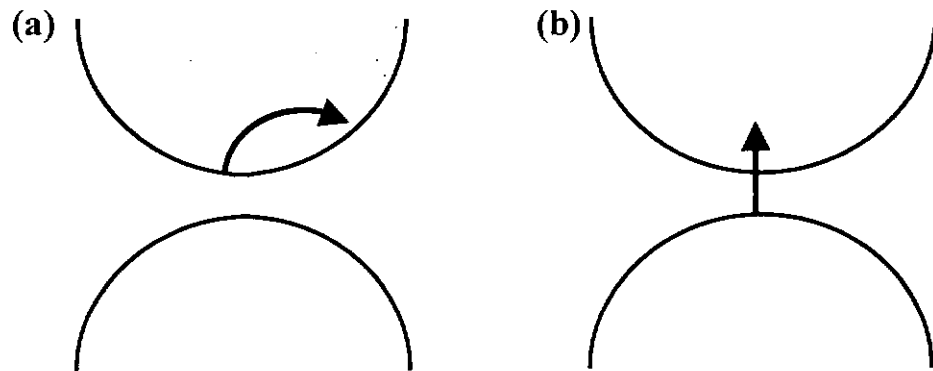


Figure 2.14 Raman scattering cause electronic transition. (a) intra-band transition and (b) interband transition.

2.5.5 Resonant light scattering

When an electron vibrates inside an atom, a harmonic oscillator formed. When the electric field of the incident light interacts with this electron, the electron is forced to vibrate and its natural frequency is changed from ω_0 to ω_i [2.41]. Since, for force vibration, the maximum amplitude of the oscillator is proportional to the factor of $[(\omega_0^2 - \omega_i^2)^2 + \omega_i^2 \Gamma^2]^{-1/2}$, where Γ is the oscillator damping constant, the maximum electric field or the polarization is proportion to that factor. That means, when $\omega_0 = \omega_i$ (resonant), the polarization becomes maximum. Also, because the polarization contributes the Raman effect in term of the second and third terms of equation (2.23), that is the first derivative term of polarization, and this first derivative term can relate to the cross section of Raman effect i.e. equation (2.21). Hence at resonant, the differential cross section of Raman effect will be very large. Although it is not so simple that only harmonic oscillation can explain the case in a solid (actually anharmonic term is required for modulation), this simplified concept is easy to be understood. There are two kind of resonant. When the incident radiation energy equal to an electronic transition, it is called incoming resonance. When the scattering radiation energy equal to an electronic transition, outgoing resonance occurred.

2.5.6 Conservation laws

The kinematics of Raman scattering processes are governed by conservation law of energy and momentum [2.4.2]:

$$\hbar\omega_s = \hbar\omega_L + \hbar\omega_R \quad (\text{conservation of energy}) \quad (2.30)$$

$$\mathbf{k}_s = \mathbf{k}_L + \mathbf{k}_R \quad (\text{conservation of momentum}) \quad (2.31)$$

where the subscript of s stand for scattering , subscript of L stand for incident light

and that of R is represent for phonon absorbed. Figure 2.15 show the vector diagram of conservation of momentum in Stoke scattering.

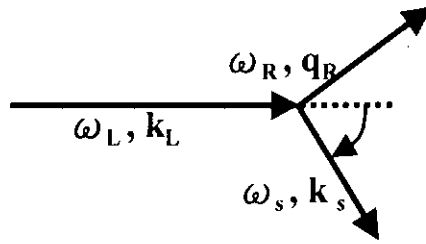


Figure 2.15 Vector diagram for the conservation of momentum in Stokes scattering.

The Raman excitation of typical visible light is in the range of $10 \leq \omega \leq 3000 \text{ cm}^{-1}$, that imply the vibration frequency is in the range of $3 \times 10^{11} \leq \omega/2\pi \leq 5 \times 10^{14} \text{ Hz}$. Thus the maximum value of $k_L = 2\pi n/\lambda$ is $1.3 \times 10^7 \text{ m}^{-1}$. For $q \sim 2k_L \sin \phi$ (from the approximation of cosine rule about figure 2.15), the range of wave-vector q can be written as $0 \leq q \leq 2.6 \times 10^7 \text{ m}^{-1}$. Therefore, for momentum conservation of phonons, q can be approximated to zero since it is two to three order of magnitudes smaller than the typical Brillouin zone edge ($\sim 10^{11} \text{ m}^{-1}$). Raman scattering is often described as a probe of zone center phonons [2.43].

2.5.7 Selection Rules

The polarization induced by the incident field E_L in the absence of any excitations of the scattering medium is

$$\mathbf{P} = \epsilon_0 \chi \mathbf{E}_L \quad (2.32)$$

where χ is the first-order susceptibility and it contributes the elastic scattering. When the excitations of the scattering or the inelastic scattering is involved, the equation

will be replaced by an equation of the form :

$$\mathbf{P} = \epsilon_0 (\chi \mathbf{E}_L + \chi \chi' \mathbf{E}_L) \quad (2.33)$$

here χ' is the second-order susceptibility that contributes the inelastic scattering.

The symmetry properties of the scattering cross section are determined by the symmetry properties of the second-order susceptibility for the excitation concerned. For detail discussion, group theory is required. However, Thompson scattering can give a simplified concept and will be shown as follow [2.44].

The radiation energy emitted (the scattering light energy along the direction $\hat{\mathbf{e}}_s$) per unit time by an electric dipole moment $\vec{\mathbf{M}}$ vibrating at the frequency ω is

$$\frac{dW_s}{d\Omega} = \frac{\omega^4}{(4\pi)^2 \epsilon_0 c^3} |\hat{\mathbf{e}}_s \cdot \vec{\mathbf{M}}|^2 \quad (2.34)$$

The dipole moment induced by an incident electric field $\mathbf{E}_L = \hat{\mathbf{e}}_L E_L$ is

$$\vec{\mathbf{M}} = \vec{\alpha} \cdot \hat{\mathbf{e}}_L E_L \quad (2.35)$$

By substitute (2.35) to (2.34) and dividing the radiation energy per unit time by the energy incident per unit area and unit time $W_L = \epsilon_0 c E_L^2$, we get the differential scattering cross section

$$\frac{d\sigma}{d\Omega} = \frac{\omega^4}{(4\pi_0 \epsilon)^2 c^4} |\hat{\mathbf{e}}_s \cdot \vec{\alpha} \cdot \hat{\mathbf{e}}_L|^2 \quad (2.36)$$

That means for some orientations, the differential scattering cross section become zero. That is happened when the dot product is equal to zero. This effect is due to the symmetric of the material that correspond to the term $\vec{\alpha}$. Therefore this rule is called the selection rule that the directions of incident and scattering light must be selected for non-zero, differential scattering cross section.

2.5.8 Sample identification by using Raman scattering

According to section 2.5.2, we know that when a laser interact with the sample, Raman scattering light of different intensities with different frequencies emitted out. The reason that it has energy changes is due to the absorption or re-emission of energy of the dipole moments stayed inside the lattice. These dipole moments are come from the interactions between the atoms of the material, that is the bonding linkage between the atoms. When these atoms absorbed or released energy, their relative atomic displacements or vibration motion change. As a result, the polarization or the bond strength of the material varies. The degree of polarization changes depends on the structure of the sample itself, which is the kind of atomic bonding. Since the degree of Raman shift is the information that incident the change of the polarization of the sample before and after interaction, Raman spectrum can lead us to understand the structural properties of the measured sample.

2.5.9 The interrelation between XRD spectrum and Raman spectrum

Although both XRD spectrum and Raman spectrum can used to identify the structural properties, they have few differences. For XRD, the source used to interact the sample is x-ray beam while it is, usually, laser in the case of Raman scattering. Another difference is that XRD spectrum show the diffraction result of x-ray beam after interacted with the sample while Raman spectrum indicates the results of change in polarization. Of course, the results of both measurements depend on the inter-structure of the interacted medium---the sample. Finally, Raman spectrum, beside identify the structural properties, is also useful in studying the energy spectrum of the sample.

2.6 Atomic Force Microscope

In addition to the crystallinity, the surface morphology of the film is also very important in structural characterization. In this section, we will introduce the principle of atomic force microscope (AFM) and how it can provide the information on the surface roughness and grain size of the films.

2.6.1 The principle of Atomic Force Microscope

The principle of the AFM is based on the inter-atomic force between the apex of a tip and atoms in a sample [2.45]. When the tip is scanned over the surface of the sample, the microscope will sense the inter-atomic force between the tip and the sample. The interaction is whether repulsive or attractive depends on which operation mode is used. When the repulsive mode is selected, the tip actually touches the sample, much like the stylus of a record player touches the surface of a record. However, the tip of the AFM is much sharper and the tracking force is much smaller: about one-millionth as great as for a record player. For these small forces, the tip can trace over individual atoms without damaging the surface of the sample. When AFM is operated in attractive mode, the feedback system of the microscope prevents the tip from touching and damaging the sample. However, the lateral resolution of the final image will be decreased. Therefore, most images obtained in this method are of micrometer-scale objects.

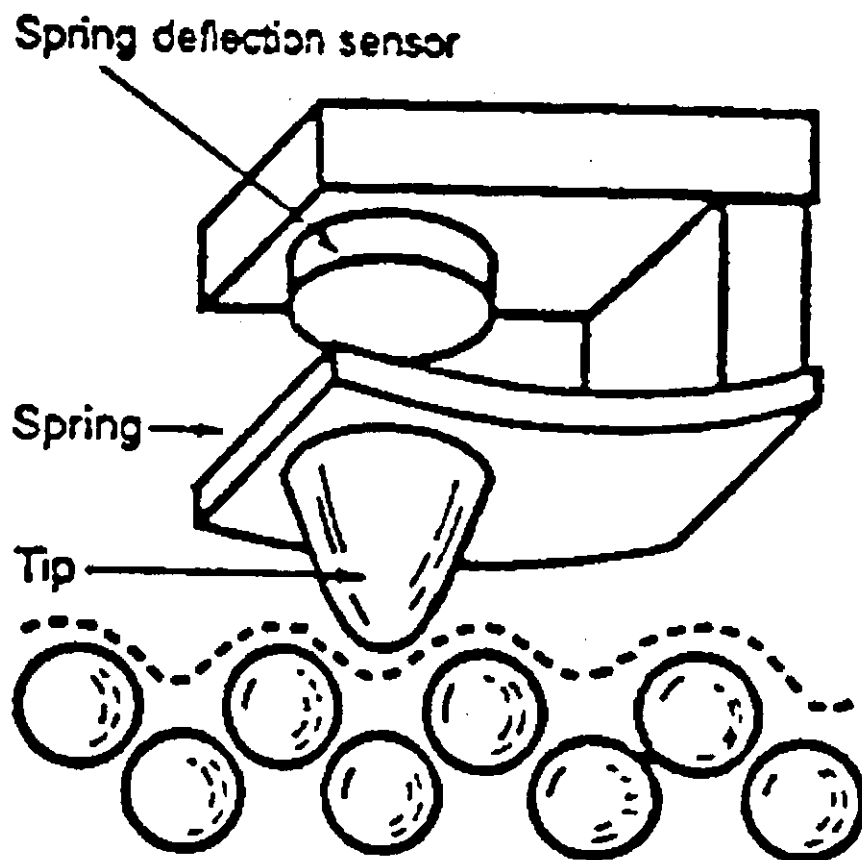


Figure 2.16 Schematic view of the force sensor for an AFM.

2.6.2 AFM working process

Figure 2.16 shown the schematic diagram of an AFM sensor. The tip of this AFM can be made of a small fractured diamond fragment attached to a spring in the form of a cantilever [2.45]. The small repulsive tracking forces between the tip and the sample, usually in the range of 10^{-6} to 10^{-9} N, are recorded by measuring minute deflections of the cantilever. A typical spring constant for a cantilever would be about 1 N/m. This means a deflection as small as 1 nm can be sensed when the tracking force as low as 10^{-9} N is applied between the tip and the sample. However, measuring this small deflection is impossible. Since the large mass of the cantilever

makes its vibrational frequency so low that it is strongly affected by vibrations in the laboratory. Nevertheless, the cantilever made by some material such as aluminum foil can decrease the sensitive of external vibrations because they have high resonant frequencies. Since higher the resonant frequency, the less sensitive the cantilever is to external vibrations, and the more stable it is for the atomic force microscope. The vibration of one end of the cantilever relative to the other in response to an external vibration of magnitude A and vibration frequency ν is approximately $A(\nu/\nu_r)^2$, where ν_r is the resonant vibration frequency of the cantilever.

The deflection of the spring in the force sensor can be measured with electron tunneling, an interferometer, or by the deflection of a laser beam reflected off a mirror mounted on the back of the spring. All that is required is an electrical signal that varies rapidly with the deflection.

2.7 Ellipsometry Measurement

Among different optical characterization methods, the technique we choose in our studies is ellipsometry which will measure the refractive index (n), extinction coefficient (k) and the film thickness (d). Based on the n and k obtained, the complex dielectric constant (ϵ_c) can be estimated. This section will be divided into two parts: (1) the background of ellipsometry and (2) the theory of ellipsometry measurement.

2.7.1 Historical Background

In 50's, with the development of computational calculation and the requirement of the semiconductor as well as complex circuit technique, ellipsometry started to develop. Afterwards, this technique expanded and was applied to the field of physics, chemistry, material science, micro-electric technique, thin film technique, surface and interface technique as well as biology. In 70's, ellipsometry had further developments. Some scientists started to improve the measuring rate and developed the spectroscopic ellipsometry (multi-wavelength measurement) instead of the monochromatic light ellipsometry. On the other hand, the image of focusing also changed. Initially the measured samples must be of single layer and homogenous with simple composition. However, at 70's, the ellipsometer could be used to measure the optical properties of multi-layers, non-homogenous and complex composite thin films. In 90's, the ellipsometry technique has rapid development for measuring different kinds of samples [2.46].

2.7.2 Theory of ellipsometry

Ellipsometry measures the variation of the reflected elliptical polarized light after a polarised light reflected from the sample surface [2.46]. The formula of reflection (Fresnel law), refraction (Snell law) and interference of the elliptical light hit on the interface between the media set as the basis concept of this measurement. The advantage of this measurement is that it can measure the refraction index (n) and the extinction coefficient (k) simultaneously, so that the Kramers-Kronig relation (K-K relation) is not required. Figure 2.17 shown the basic set-up of the ellipsometry.

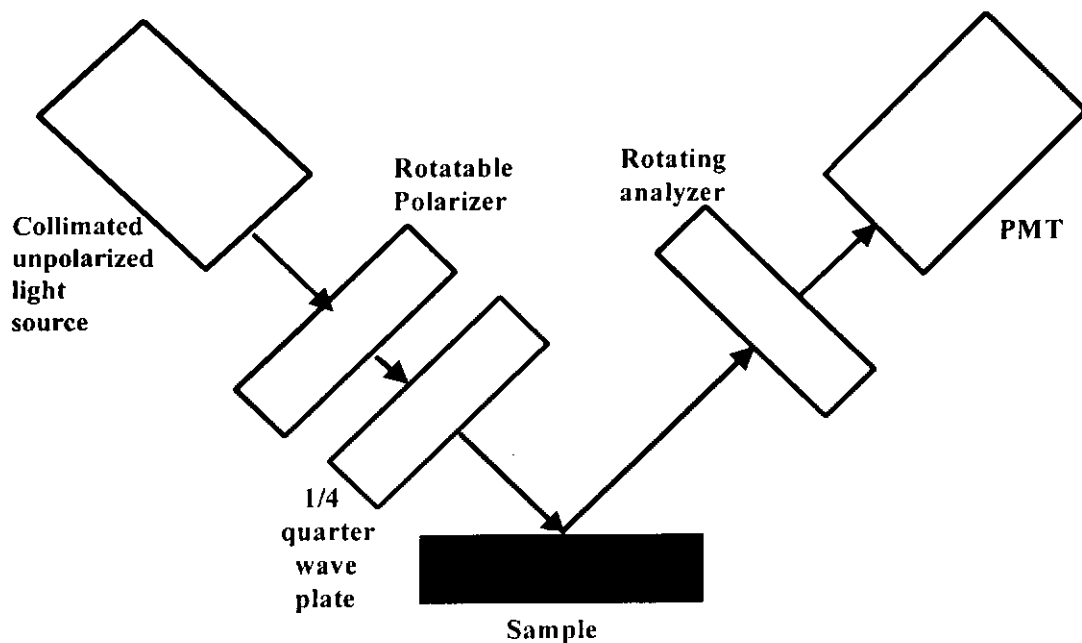


Figure 2.17 Optical path of ellipsometry

For ellipsometer, the unpolarized monochromatic light is produced by a light source. After passing through the rotatable polarizer, the unpolarized light becomes linear polarized. The direction of the polarization is determined by the angle of the polarizer. Therefore, rotating the polarizer can various the polarization direction of the light beam. Then linear polarized light will pass through the 1/4 quarter wave plate so that it becomes elliptically polarized. This phenomenon can be

explained as the double refraction of the linear polarized light inside the 1/4 quarter wave plate. As a result, two polarized light beam with phase difference of 90° are produced and the superposition of this two waves form the elliptical polarization of light. Since the degree of elliptical of the light depends on the direction of the linear polarization of light, rotation of the polarizer will change the shape of the elliptical polarized light beam. When the elliptical beam has been reflected from the sample, the directional angle and the shape of the ellipse varies. For normal case, rotation of the angle of the polarizer will result in changing the reflected light from elliptical polarization (before reflect from the sample) to linear polarization (after reflection) at a particular orientation. Therefore, rotation of the analyzer to a particular direction can prevent any light entering the detector.

For the change of the polarization of light after reflection, we can use the Fresnel laws, Snell laws and interference formula for analysis. Let us consider the simplest case that the sample has one layer of thin film on a semi-infinite substrate. Figure 2.18 show the reflection and refraction of this one layer sample.

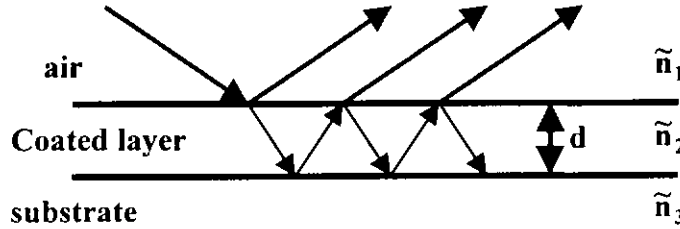


Figure 2.18 Reflection and Refraction of one layer film.

From Figure 2.18, the Fresnel reflection coefficients of the air-film interface are

$$r_{1p} = \frac{\tilde{n}_2 \cos \varphi_1 - \tilde{n}_1 \cos \varphi_2}{\tilde{n}_2 \cos \varphi_1 + \tilde{n}_1 \cos \varphi_2} \quad (2.37)$$

$$r_{1s} = \frac{\tilde{n}_1 \cos \varphi_1 - \tilde{n}_2 \cos \varphi_2}{\tilde{n}_1 \cos \varphi_1 + \tilde{n}_2 \cos \varphi_2} \quad (2.38)$$

while the Fresnel reflection coefficients of the film-substrate interface are

$$r_{2p} = \frac{\tilde{n}_3 \cos \varphi_2 - \tilde{n}_2 \cos \varphi_3}{\tilde{n}_3 \cos \varphi_2 + \tilde{n}_2 \cos \varphi_3} \quad (2.39)$$

$$r_{2s} = \frac{\tilde{n}_2 \cos \varphi_2 - \tilde{n}_3 \cos \varphi_3}{\tilde{n}_2 \cos \varphi_2 + \tilde{n}_3 \cos \varphi_3} \quad (2.40)$$

Here \tilde{n}_1, \tilde{n}_2 and \tilde{n}_3 are the refractive indexes of air, film and substrate respectively.

The angle φ_1 is the incident angle while φ_2 and φ_3 are the refraction angles as both of them are real numbers (the detail will be discussed later). The footnotes of p and s here stand for the polarization components perpendicular to the incident plane and along the incident plane respectively. Notice that r_{1p} , r_{1s} , r_{2p} and r_{2s} normally are complex numbers. Since, according to the refraction laws, the relation between φ_1 , φ_2 and φ_3 can be written as

$$\tilde{n}_1 \sin \varphi_1 = \tilde{n}_2 \sin \varphi_2 = \tilde{n}_3 \sin \varphi_3 \quad (2.41)$$

Here, \tilde{n}_1 and $\sin \varphi_1$ are real numbers for the media while \tilde{n}_2 and \tilde{n}_3 usually are complex numbers as well as $\sin \varphi_2$ and $\sin \varphi_3$. Hence φ_2 and φ_3 are complex and cannot be seen as simple refraction angles. From Figure 2.18, we can see that the total reflection light beam is the result of the superposition of all light beam reflected from different layers. Therefore, after considering the interference effect of the light, the total reflection coefficients can be calculated as

$$R_p = \frac{r_{1p} + r_{2p} e^{-2i\delta}}{1 + r_{1p} r_{2p} e^{-2i\delta}} \quad (2.42)$$

$$R_s = \frac{r_{1s} + r_{2s} e^{-2i\delta}}{1 + r_{1s} r_{2s} e^{-2i\delta}} \quad (2.43)$$

where

$$\delta = \frac{2\pi}{\lambda} d \tilde{n}_2 \cos \varphi_2 \quad (2.44)$$

Hence, λ is the wavelength of the light travelling in air and d is the film thickness.

Since ellipsometry is the method using the wave property of light, both amplitude

and phase difference of the light before and after reflection is necessary for consideration. Define the parameter of ψ and Δ as

$$\tan \psi e^{i\Delta} = \frac{R_p}{R_s} \quad (2.45)$$

such that $\tan \psi$ stands for the ratio of relative decay polarization amplitude and Δ is the phase difference of the polarized light before and after reflection. Both ψ and Δ are measured as angle.

In the experiment, the wavelength of the incident light (λ) as well as the incident angle (ϕ_1) are known, if we know \tilde{n}_1 (usually equal to 1 for air) and \tilde{n}_3 (refractive index of the substrate), then both ψ and Δ can be set as the function of the film thickness (d) and the refractive index of the film (\tilde{n}_2), that is

$$\psi = \psi(d, \tilde{n}_2) \quad ; \quad \Delta = \Delta(d, \tilde{n}_2) \quad (2.46)$$

Thus, by measuring the value of ψ and Δ , we can find out the film thickness and refractive index of the measured film.

From Figure 2.17, when the polarizer and analyzer are rotated to an orientation that no signal is detected by the detector, at that time let P and A are the angle of the polarizer and analyzer respectively, the relationship between A and P and Δ are

$$A = P \quad (2.47)$$

$$\begin{aligned} \Delta &= 270^\circ - 2P, \quad \text{when } 0 \leq P \leq 135^\circ \\ &= 630^\circ - 2P, \quad \text{when } P > 135^\circ \end{aligned} \quad (2.48)$$

where A is the angle between 0° to 90° , as P is the angle between 0° to 180° . Therefore after recording the values of A and P , we can know the values of ψ and Δ

and hence the value of \tilde{n}_2 and d can be known. Let us consider some special cases.

(1) transparent film

In this case, \tilde{n}_2 only contains the real part. Therefore there are only 2 unknown parameters of n_2 and d . In principle, since we have measured the values of ψ and Δ , we can solve the equation stated above to find out n_2 and d .

(2) Substrate only

In this case, $d = 0$ and therefore the equations of (2.42) and (2.43) can be simplify to

$$R_p = \frac{\tilde{n}_3 \cos \varphi_1 - \tilde{n}_1 \cos \varphi_3}{\tilde{n}_3 \cos \varphi_1 + \tilde{n}_1 \cos \varphi_3} \quad (2.49)$$

$$R_s = \frac{\tilde{n}_1 \cos \varphi_1 - \tilde{n}_3 \cos \varphi_3}{\tilde{n}_1 \cos \varphi_1 + \tilde{n}_3 \cos \varphi_3} \quad (2.50)$$

Let \tilde{n}_3 equal to $n - ik$, then n and k can be solved as

$$n^2 = k^2 + \sin^2 \varphi_1 \left[1 + \frac{\tan^2 \varphi_1 (\cos^2 2\psi - \sin^2 2\psi \sin^2 \Delta)}{(1 + \sin 2\psi \cos \Delta)^2} \right] \quad (2.51)$$

$$k = \frac{\sin^2 \varphi_1 \tan^2 \varphi_1 \sin 4\psi \sin \Delta}{2n(1 + \sin 2\psi \cos \Delta)^2} \quad (2.52)$$

here \tilde{n}_1 is equal to 1. Although n and k of the substrate can be easy found out at the same time, the oxide layer coated on the substrate can affect the measuring result. Thus, to get rid the oxide layer is a very important step before measurement.

(3) absorption film layer

In this case, all the values of n , k and d are unknown. However, we only have two

equations (2.46), therefore, in principle, the three unknown parameters cannot be solved simultaneously. By using different incident angle, a new set of equations (2.46) will be resulted, then the three unknown parameters can be solved.

To measure ψ and Δ under different wavelength of incident light, ellipsometry spectrum can be obtained. There are two kinds of measuring techniques, namely, extinction method and intensity method. For extinction method, it is similar to that described in Figure 2.17. However it has one disadvantage. When this method is selected to use, the $1/4$ quarter wave plate must be change continuously if a large range of spectrum is to be measured. Since the $1/4$ quarter wave plate normally sensitive for a particular wavelength only.

For intensity method, the optical alignment is different from that of Figure 1.17. The $1/4$ quarter wave plate is taken away and the angle of the polarizer is fixed at a particular position, usually at $+45^\circ$. When the analyzer is being rotated, the intensity of the reflected beam (I) changes with the position of the analyzer angle (θ). The relationship between I and θ is:

$$I = I_o [1 + \cos 2\chi \cos 2(\theta - \alpha)] \quad (2.53)$$

where I_o is the average light intensity, χ is the parameter depended on the shape of the elliptical polarized light and α is the angle tiling of the major axis. By using this method, the light before incident onto the sample is linear polarized while changed to elliptical polarized after reflection. For different angle of analyzer, different intensity of reflection beam can be detected. Hence the I - θ curve can be formed. As a result, χ and α can be obtained. However, instead of plotting out the I - θ curve, a simple technique can be used. The idea of this method is to find out the maximum and minimum intensities with the related angles of analyzer. Since,

according to the equation (2.53), the detected light is set as maximum when

$$\theta_{\max} = \alpha \quad (2.54)$$

$$\text{that is } I_{\max} = I_o + I_o \cos 2\chi \quad (2.55)$$

and the detected light set as minimum when

$$\theta_{\min} = \alpha \pm 90^\circ \quad (2.56)$$

$$\text{that is } I_{\min} = I_o - I_o \cos 2\chi \quad (2.57)$$

Also, by (2.55) and (2.57), we can find out the value of χ by

$$\cos 2\chi = \frac{I_{\max} - I_{\min}}{I_{\max} + I_{\min}} \quad (2.58)$$

therefore, χ and α can be found out. By using the relation between (χ, α) and (ψ, Δ) , we get

$$\tan \Delta = \pm \frac{\tan 2\chi}{\sin 2\alpha} \quad (2.59)$$

$$\cos 2\psi = -\cos 2\chi \cos 2\alpha \quad (2.60)$$

Beside the refractive index and thickness, another important parameter of the film is its dielectric constant. From the definitions of reflectivity coefficient $r(\omega)$, $n(\omega)$ and $k(\omega)$, (n, k) is related to the complex dielectric (ϵ, ϵ_c) as following [2.47]:

$$\begin{aligned} n^2 - k^2 &= \frac{\epsilon}{\epsilon_0} \\ \text{and } 2nk &= \frac{\epsilon_c}{\epsilon_0} \end{aligned} \quad (2.61)$$

By obtaining n and k , the dielectric constant of the film can be found out.

References 2

- [2.1] H.R. Xia, C.J. Wang, H.Yu, H.C. Chen and M. Wang, "Polarization and Dipole Moments of Manganese-Modified Potassium Sodium Strontium Barium Niobate Crystals". *Japanese Journal of Applied Physics Part I*, 36, pp.2179-2182 (April,1997).
- [2.2] Yuhuan Xu, "Ferroelectric tungsten-bronze-type niobate crystals". *Ferroelectric Materials and Their Applications*, Elsevier Science Publishers B.V., Asterdam; New York : North-Holland, p. 247 and 263 (1991).
- [2.3] H.C. Chen and Y.H. Xu, "New ferroelectric crystal with tungsten-bronze-type --- $(K_{1-x}Na_x)_{0.4}(Sr_{1-y}Ba_y)_{0.8}Nb_2O_6$ ". *Physics*, 10, pp.729 (1981).
- [2.4] Yuhuan Xu, "Ferroelectric tungsten-bronze-type niobate crystals". *Ferroelectric Materials and Their Applications*, Elsevier Science Publishers B.V., Asterdam; New York : North-Holland, p. 248 (1991).
- [2.5] A.A. Savvinov, I.G. Siny and R.S. Katiyar, "Anomalies in the Raman Spectra of KNSBN with the Tungsten-Bronze Structure". *Journal of the Korean Physical Society*, 32, pp. S617-S620 (February 1998).
- [2.6] H.R. Xia, K.X. Wang, B.Y. Zhao, C.H. Chen, X.L. Lu, Q.Z. Jian, P.J. Sun, and L.J. Hu, "Study of Raman spectra for ferroelectric tungsten bronze-type crystals SBN and KNSBN". *Acta Physica Sinica*, 45, pp.232-237 (1996).
- [2.7] L.A. Bursill and Peng Ju Lin, "Chaotic states observed in strontium barium niobate". *Philosophical Magazine B*, 54, pp. 157-170 (1986).
- [2.8] Maureen L. Mulvihill, Kenji Uchino, Zhuang Li and Wenwu Cao, "In-situ observation of the domain configurations during the phase transitions in barium titanate". *Philosophical Magazine B*, 74, No.1, pp. 25-36 (1996).
- [2.9] H.C. Chen, D.L. Sun, Y.Y. Song and Q.Z. Jiang, "Growth and properties of a new TB type photorefractive crystal". *Journal of Crystal Growth*, 128, pp.880-885 (1993).

- [2.10] Yuhuan Xu, "Methods for measuring the physical properties of ferroelectric materials". *Ferroelectric Materials and Their Applications*, Elsevier Science Publishers B.V., Asterdam; New York : North-Holland, p. 61 (1991).
- [2.11] Yuhuan Xu, "Methods for measuring the physical properties of ferroelectric materials". *Ferroelectric Materials and Their Applications*, Elsevier Science Publishers B.V., Asterdam; New York : North-Holland, pp. 83-85 (1991).
- [2.12] Yuhuan Xu, "Perovskite-type ferroelectric: part II". *Ferroelectric Materials and Their Applications*, Elsevier Science Publishers B.V., Asterdam; New York : North-Holland, p. 174 (1991).
- [2.13] Yuhuan Xu, "Lithium niobate and lithium tantalate". *Ferroelectric Materials and Their Applications*, Elsevier Science Publishers B.V., Asterdam; New York : North-Holland, p. 231 (1991).
- [2.14] Yuhuan Xu, "Ferroelectric tungsten-bronze-type niobate crystals". *Ferroelectric Materials and Their Applications*, Elsevier Science Publishers B.V., Asterdam; New York : North-Holland, p. 267 (1991).
- [2.15] M.N. Rahaman, "Ceramic Fabrication Processes: An Introduction Overview". *Ceramic Processing and sintering*, Marcel Dekker, Inc., New York, pp.5-17 (1995).
- [2.16] M.N. Rahaman, "Sol-Gel Processing". *Ceramic Processing and sintering*, Marcel Dekker, Inc., New York, pp.207 (1995).
- [2.17] M.N. Rahaman, "Sol-Gel Processing". *Ceramic Processing and sintering*, Marcel Dekker, Inc., New York, pp.208-214 (1995).
- [2.18] M.N. Rahaman, "Sol-Gel Processing". *Ceramic Processing and sintering*, Marcel Dekker, Inc., New York, pp.256-257 (1995).
- [2.19] C. Jeffrey Brinker and George W. Scherer, *Sol-gel Science ----- the Physics and Chemistry of Sol-Gel Processing*, Academic Press, London, pp. 788-794 (1990).

- [2.20] J. Livage, M. Henry and C. Sanchez, "Sol-Gel Chemistry of Transition Metal Oxides". *Progress in Solid State Chemistry*, 18, pp.286-288 (1988).
- [2.21] C.J. Brinker, G.W. Scherer and E.P. Roth, "Sol→Gel→Glass: II. Physical and Structural Evolution during Constant Heating Rate Experiments". *Journal of Non-Crystalline Solids*, 72, pp.350-356 (1985).
- [2.22] T. Hatakeyama and F.X. Quinn, "Differential Thermal Analysis and Differential Scanning Calorimetry". *Thermal Analysis: Fundamentals and Applications to Polymer Science*, John Wiley & Sons, Chichester, pp. 5-7 (1994).
- [2.23] T. Hatakeyama and F.X. Quinn, "Therogravimetry". *Thermal Analysis: Fundamentals and Applications to Polymer Science*, John Wiley & Sons, Chichester, pp. 38-39 (1994).
- [2.24] M. Nelkon and P. Parker, "Photo-electricity, Energy Levels, X-rays, Wave-Particle Duality". *Advanced Level Physics*, 6th edition, Heinemann Educational Books Ltd., London, p.867 (1987).
- [2.25] Albert Franks, "The First Hundred Years". Alan Michette and Stawka Pfauntsch, *X-Rays: The First Hundred Years*, John Wiley & Sons, England, pp.3-8 (1996).
- [2.26] M.F.C. Ladd and R.A. Palmer, "Preliminary Examination of Crystals by Optical and X-ray Methods". *Structure Determination by X-ray Crystallography (3rd edition)*, Plenum Press, New York, pp.134-137 (1994).
- [2.27] C. Suryanarayana, M. Grant Norton, "EXPERIMENTAL MODULE 1--- Crystal Structure Determination I: Cubic Structures". *X-Ray Diffraction: A Partical Approach*, Plenum Press, New York and London, p.98 (1998).
- [2.28] C. Suryanarayana, M. Grant Norton, "Lattices and Crystal Structures". *X-Ray Diffraction: A Partical Approach*, Plenum Press, New York and London, pp.52-54 (1998).

-
- [2.29] C. Suryanarayana, M. Grant Norton, "EXPERIMENTAL MODULE 8--- Identification of an Unknown Specimen". *X-Ray Diffraction: A Partical Approach*, Plenum Press, New York and London, p.237 (1998).
- [2.30] C. Suryanarayana, M. Grant Norton, "EXPERIMENTAL MODULE 6--- Determination of Crystallite Size and Lattice Strain". *X-Ray Diffraction: A Partical Approach*, Plenum Press, New York and London, p.207-213(1998).
- [2.31] C. Suryanarayana, M. Grant Norton, "EXPERIMENTAL MODULE 6--- Determination of Crystallite Size and Lattice Strain". *X-Ray Diffraction: A Partical Approach*, Plenum Press, New York and London, p.213-215(1998).
- [2.32] William Hayes and Rodney Loudon, "Basic Features and Formal Theory of Light Scattering". *Scattering of Light by Crystals*, John Wiley and Sons, New York, p.2 (1978).
- [2.33] William Hayes and Rodney Loudon, "Basic Features and Formal Theory of Light Scattering". *Scattering of Light by Crystals*, John Wiley and Sons, New York, p.2 (1978).
- [2.34] William Hayes and Rodney Loudon, "Basic Features and Formal Theory of Light Scattering". *Scattering of Light by Crystals*, John Wiley and Sons, New York, p.3 (1978).
- [2.35] John R. Ferraro and Kazuo Nakamoto, "Basic Theory". *Introductory Raman Spectroscopy*, Academic Press, London, pp.14-15 (1994).
- [2.36] William Hayes and Rodney Loudon, "Basic Features and Formal Theory of Light Scattering". *Scattering of Light by Crystals*, John Wiley and Sons, New York, p.7(1978).
- [2.37] William Hayes and Rodney Loudon, "Basic Features and Formal Theory of Light Scattering". *Scattering of Light by Crystals*, John Wiley and Sons, New York, p.15 (1978).
- [2.38] John R. Ferraro and Kazuo Nakamoto, "Basic Theory". *Introductory Raman Spectroscopy*, Academic Press, London, pp.15-16 (1994).

-
- [2.39] Fred P. Milanovich, “ Stimulated Raman Scattering (Nonlinear Optical Properties)”. Weber, Marvin J., *CRC Handbook of Laser Science and Technology*, CRC Press, Boca Raton, p.238.
- [2.40] William Hayes and Rodney Loudon, “Basic Features and Formal Theory of Light Scattering”. *Scattering of Light by Crystals*, John Wiley and Sons, New York, p.33-37(1978).
- [2.41] William Hayes and Rodney Loudon, “Basic Features and Formal Theory of Light Scattering”. *Scattering of Light by Crystals*, John Wiley and Sons, New York, p.9(1978).
- [2.42] William Hayes and Rodney Loudon, “Basic Features and Formal Theory of Light Scattering”. *Scattering of Light by Crystals*, John Wiley and Sons, New York, p.11-13(1978).
- [2.43] William Hayes and Rodney Loudon, “Basic Features and Formal Theory of Light Scattering”. *Scattering of Light by Crystals*, John Wiley and Sons, New York, p.15(1978).
- [2.44] Rodney Loudon, “The scattering of light by atoms”. *The quantum theory of light*, Clarendon Press, Oxford, pp.271-273 and 290-293 (1973).
- [2.45] P.K. Hansma, V.B. Elings, O. Marti and C.E. Barcker, “Scanning Tunneling Microscopy: Application to Biology and Technology”. *Science*, American Association For The Advancement of Science, Washington, 242, pp.209-216 (1988).
- [2.46] Dang Mo, “spectroscopic ellipsometry”, *Solid state optics*, High Level Education Publishing Ltd., Beijing, pp.135-141 (1996).
- [2.47] Dang Mo, “Macroscopic description of optical properties ”, *Solid state optics*, High Level Education Publishing Ltd., Beijing, pp.9-11 (1996).

Chapter 3

Experimental Aspects

The object of this chapter is to describe the experimental procedures of the fabrication process and characterization of KNSBN powders and films in detail. The content includes (1) preparation of KNSBN sol, powders and films, (2) experimental procedure for DTA and TGA measurement of KNSBN powders, (3) XRD spectra measurement, (4) Raman spectroscopic measurement, (5) AFM study and optical characterization.

3.1 PREPARATION OF KNSBN CERAMICS

3.1.1 Fabrication of KNSBN sol

As strontium metal, barium metal and sodium ethoxide can directly react with the 2-methoxyethanol spontaneously, they were selected as the starting agents to prepare KNSBN solution. The first step was to prepare the metal alkoxides. The solvent, 2-methoxyethanol, which also acted as the sol stabilizer, was distilled for about 1 hour before reacted with the starting agents. The process of distillation could get rid all the water molecules from the alcohol. Using 2-methoxyethanol as the solvent, the alkoxides and the KNSBN sol formed were less susceptible to hydrolysis. After distillation, strontium metal, barium metal and sodium ethoxide were dissolved and refluxed individually in the pure 2-methoxyethanol for about 2 hours. As a result, strontium methoxyethanoxide, barium methoxyethanoxide and sodium methoxyethanoxide were formed respectively. Then, niobium(V) chloride and

potassium hydroxide were used to prepare the other two alkoxides. The calculated amount of potassium hydroxide was dissolved in 2-methoxyethanol before niobium(V) chloride was added. The potassium hydroxide here had two functions. It was used to get rid the chloride ions by forming potassium chloride precipitate in the solution. On the other hand, the residual KOH was used to form the potassium alkoxide. Of course, the niobium ions inside the solution would react with the alcohol to form niobium alkoxide. The precipitate (KCl) was then separated from the final solution of niobium and potassium alkoxides by filtration. Since part of KCl formed would re-dissolve in the solution at room temperature and the chloride ions then might compete with 2-methoxyethoxy group to attach to the niobium atom, precipitate separation has to be done at reflux temperature. After the successful preparation of the individual metal alkoxide solution, they were mixed together according to the stoichiometric ratio of $K : Na : Sr : Ba : Nb = 0.2 : 0.2 : 0.48 : 0.32 : 2$. The final KNSBN sol was clear yellowish brown in colour without any suspension of particles. The whole experiment was done in the atmosphere of dry argon to prevent pre-hydrolysis of solution with the water molecules in air. The mixed solution was then divided into six parts and each was refluxed to concentrate the solutions to different concentration of 0.03M, 0.06M, 0.09M, 0.12M, 0.15M and 0.18M.

3.1.2 Preparation of KNSBN powders from sol

To synthesis KNSBN powders, part of the KNSBN sol with 0.03M was selected for hydrolysis. Small volume of water together with 2-methoxyethanol was added to the sol. Then the solution was stirred to activate the reaction. After complete hydrolysis, the unwanted water molecules and alcohol were removed by drying the gel in oven at 100 °C for 60 hours. Pieces of yellowish brown loosely packed solid were obtained. The solid was ground into fine powders by using mortal and pestle. Then the

ground powders were put into a high temperature furnace for annealing at different temperatures ranging from 500 °C to 1200 °C for 2 hours. The heating rate of the furnace was set at 10 °C/min.

3.1.3 Preparation of KNSBN films from sol

To fabricate KNSBN films, dip-coating technique was used. Initially, area of $1 \times 2 \text{ cm}^2$ (100)Si wafers, which were used as the substrate of the films, were cleaned and etched. Then the upper edge of the wafer was pasted to a rod that was attached to a XYZ motorized translator. After then, the Si wafers were dipped into different homogeneous solutions with different sol concentration. The withdrawn rate was controlled by the motorized translator. The as-deposited amorphous films were then dried in air for about half an hour and were annealed at different temperature from 400 °C to 800 °C for 2 hours with a heating rate of 1 °C/min. The slow heating rate was chosen to make sure that the samples were not damaged by the internal stress built up inside the films due to the rapid heating process. To fabricate multi-layers films, the procedure of dip-and-dry was repeated after each of the annealing. In our study, three series of the films were fabricated, namely, (1) different annealing temperature (400 °C, 500 °C, 600 °C, 700 °C and 800 °C): 3 dip-coated layers with sol concentration of 0.21M, withdraw rate of 0.3 cm/sec and annealing time of 2 hours; (2) different coated layers (1-layer, 2-layer, 5-layer and 10-layer) with single annealing cycle: films with sol concentration of 0.03M, withdraw rate of 0.3 cm/sec and annealing temperature of 700 °C for 2 hours; and (3) different sol concentration: 1-layer films with sol concentration of 0.03M, 0.06M, 0.09M, 0.12M, 0.15M, and 0.18M, withdraw rate of 0.3 cm/sec and annealed at 700 °C for 2 hours. Figure 3.1 shows the schematic diagram of fabrication of KNSBN powders and films.

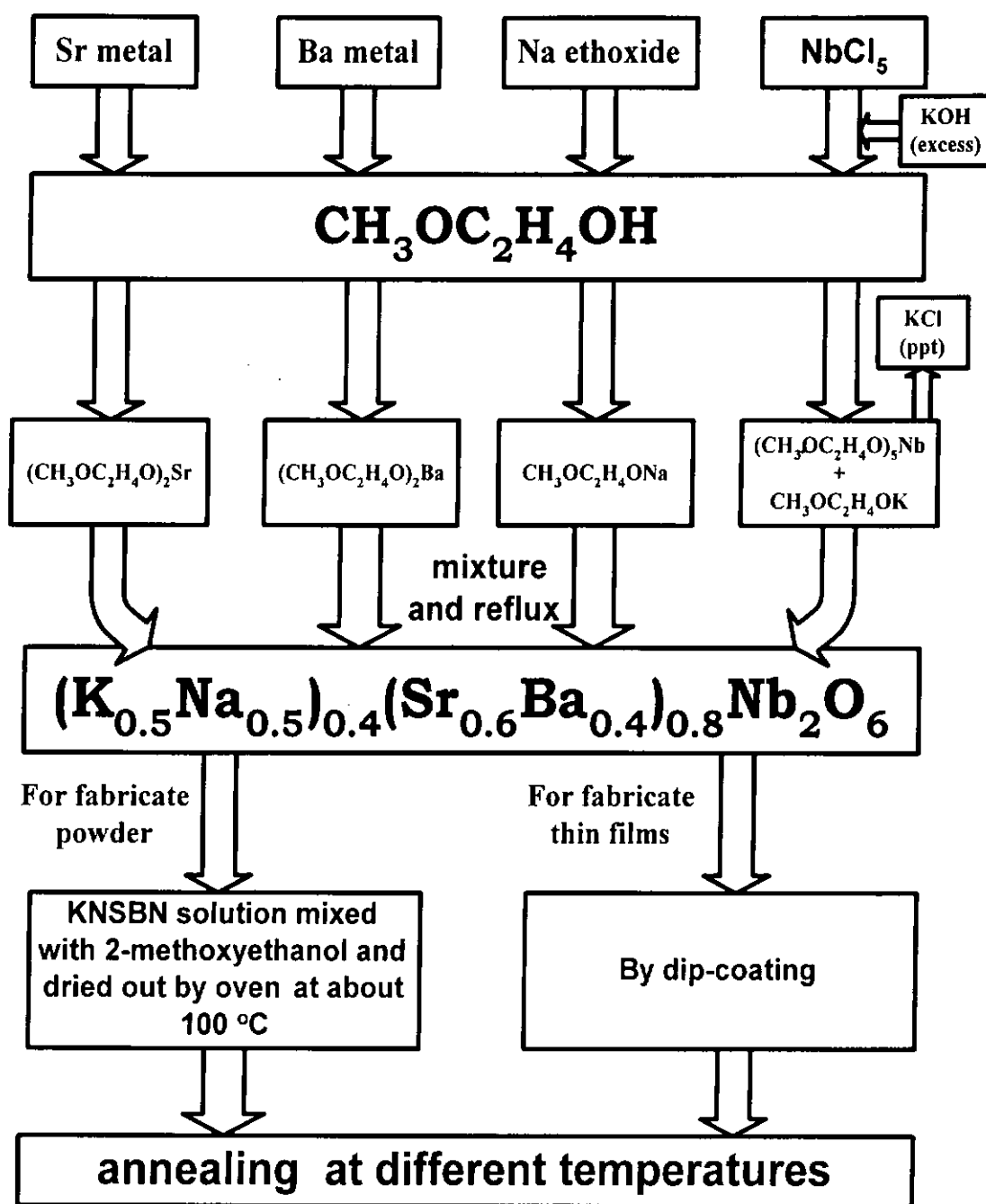


Figure 3.1 The flow chart of synthesis route of KNSBN powders and films.

3.2 THERMAL ANALYSIS OF KNSBN POWDERS

In order to study the crystallization behaviors, amorphous KNSBN powders were used. The weight change in the annealing process was studied by thermogravimetry (TG, Rheometric Scientific, Model: TG 1000+) while the energy change of the powders as the temperature varied was analyzed by differential thermal analysis (DTA, Perkin-Elmer). Both measurements were kept at a heating rate of 10°C/min.

3.3 X-RAY DIFFRACTION MEASUREMENT

All experimental data of XRD spectra were obtained from a x-ray diffractometer (Philip Model PW3710). The tube anode is Cu and the wavelength of emitted X-ray are 1.54060 Å and 1.54439 Å with intensity ratio of 0.5. The power of the diffractometer is 140 kW. The divergence slit used was 0.25° and the receiving slit was 0.1mm. Monochromator was employed to filter out the unwanted signal arisen from other x-ray wavelengths. For the scan mode of θ -2 θ , all the powders and films were scanned continuously from 2 θ = 20° to 60° with the step size of 0.02 and integral time of 1 second.

For powder measurement, the powders were held on a home-made sample holder. The holder was made by attaching several pieces of smaller slide glass together on a cleaned glass slide so that a hole is formed in the middle of the clean glass slide. Therefore, the powders can be held firmly during the measurement.

For film measurement, a Si wafer was pasted to one end of a glass slide and the film was attached on the other side of the slide so that both the Si wafer and the sample attached were at the same level. The glass slide with the Si wafer and the film was mounted on the sample mount which was fixed to the diffractometry.

3.4 RAMAN SPECTRA MEASUREMENT

Figure 3.2 is a schematic representation of the set-up for our Raman measurements. Raman spectra for both powders and films were excited by a CW argon gas laser (Coherent Innova 70) with laser line of 514.5 nm. The argon gas laser was selected because the advantages of well polarization, well collimated, high power output with short wavelength and excellent power stability. The power of the laser after passing the interference filter was set at 200mW and 300mW for powders and thin film measurement respectively, so that laser annealing of the samples could be avoided. All measurements were done at room temperature.

The laser light was first reflected by two plane mirrors to alter it to a convenient direction. This configuration could also used to make sure that the incident beam would be at right angle to that of scattering beam. Furthermore, an interference filter (Oriel Model no. 52680) with bandwidth of 10nm was employed to filter the unwanted laser plasma lines. After passing through the filter, the laser beam was focused by a convex lens of focal length equal to 175 mm. This lens could increase the power density of the light irradiated onto the sample. As the intensity of the scattered light is proportion to the intensity of the exciting light, increasing the power density of incident light would obtain a strong signal for detection. The measured sample was held on the sample holder and was positioned at about 45° with the incident light. It prevented the reflected beam, the Rayleigh line, entered into the collimating lens and the monochromator. Since the intensity of the Rayleigh scattering light is much stronger than that of the Raman scattering light, the latter would be overwhelmed by the former when both scattering light were collected at the same time. A camera lens (Canon FD85mm 1:1.8) was used for collimating the scattered light which was detected and analyzed by the double grating monochromator (Spex 1403). A short focal length camera lens was selected as the collimator because shorter focal length

leads to a larger solid angle subtended by the collimator. Hence more scattered light would be collected. Finally, a collecting lens ($f = 150\text{mm}$) was used to focus the parallel scattered beam onto the entrance slit of the double spectrometer. The focal length of the collecting lens was determined by f-number of the first mirror inside the spectrometer. The relationship between the focal length and diameter of these two optical instruments can be presented as :

$$\frac{d_c}{f_c} = \frac{d_{fm}}{l} \quad (3.1)$$

where d_c and f_c are the diameter and focal length of the collecting lens respectively. d_{fm} is the diameter of the first mirror inside the spectrometer and l is the distance between the entrance slit and the first mirror.

The scattered light with mixed wavelengths was dispersed by a double grating spectrometer. The final light spectrum was detected by a cooled photomultiplier tube (PMT, Hamamatus R943-2). A photomultiplier cooler (Hamamatus C4877) was used to cool down the PMT so that the thermal noise could be minimized.

For powders, they were pressed and held into a small crucible which was pasted onto the sample mount. For films, the films were pasted directly onto the sample mount. After focusing, the scanning process could be started. The voltage of the PMT used was 2000 V. The signal controlled by a personal computer. The spectral range to be scanned, the scanning rate, scanning steps, and the accumulation time were selected prior to each scan. The slit width of the monochromator were selected so that the resolution of the spectra was 1 cm^{-1} .

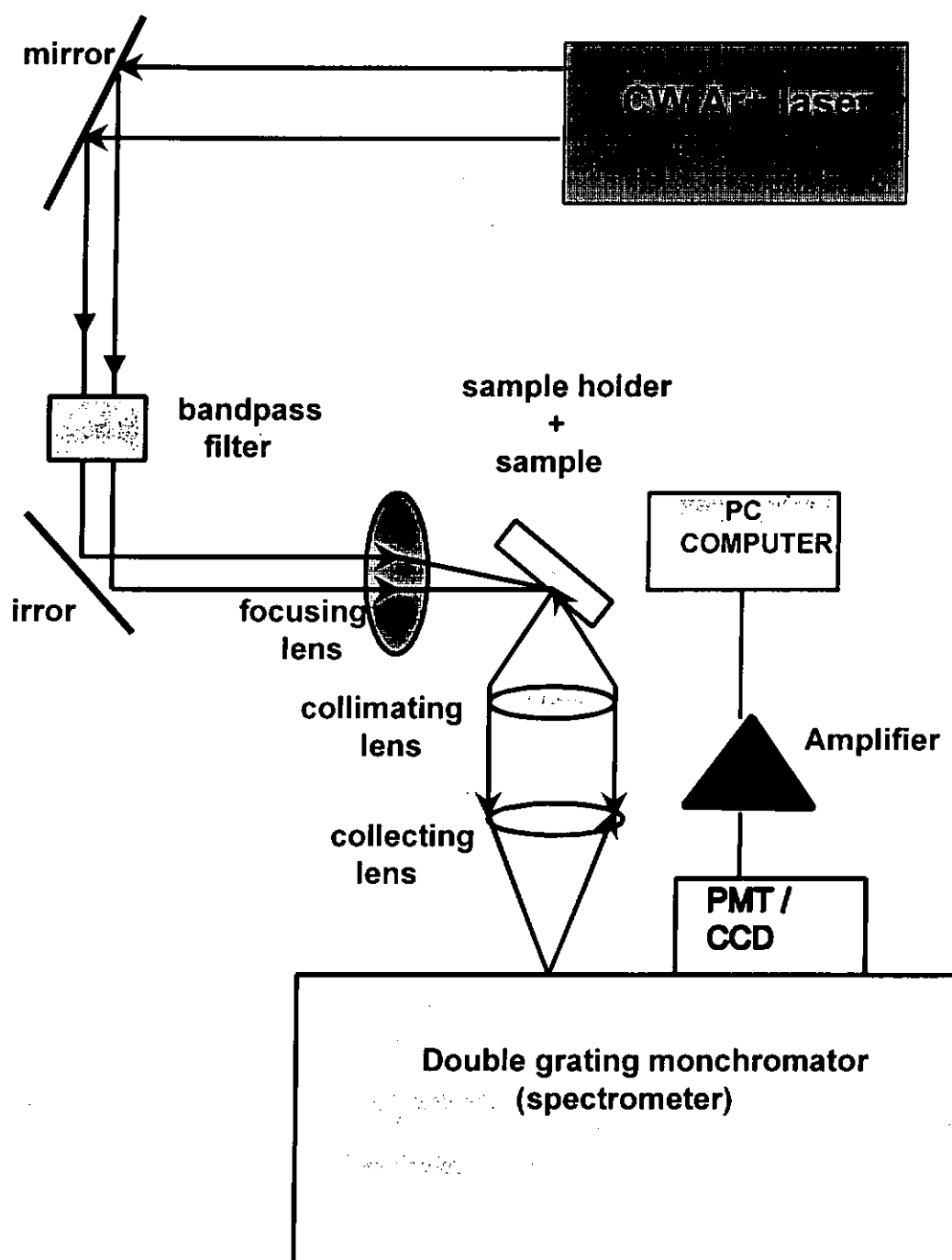


Figure 3.2 Experimental setup of Raman spectroscopy.

3.5 SURFACE MORPHOLOGY MEASUREMENTS

The surface morphology of the samples were measured by atomic force microscope METRIS-2000. The schematic diagram of AFM with this module was shown in Figure 3.3. The scan area are $25\text{ }\mu\text{m} \times 25\text{ }\mu\text{m}$, $10\text{ }\mu\text{m} \times 10\text{ }\mu\text{m}$, $5\text{ }\mu\text{m} \times 5\text{ }\mu\text{m}$ and $2\text{ }\mu\text{m} \times 2\text{ }\mu\text{m}$ respectively. A silicon nitride probe was attached to the probe mount by adhesive. The silicon nitride probe was selected because contact attractive mode was chosen for measurement. Then the probe mount was inserted into the probe mount holder and the probe was aligned in the position under the light spot produced by a very low power laser beam. Therefore, the probe could be viewed with an optical microscope through the top aperture. An attenuation filter was placed at the top aperture to remove over 90 percent of laser reflection light that could cause any danger. After then, the measured samples were attached to the sample mount by adhesive and inserted into the sample mount holder. On the other hand, the calibration sample of regular grating of 62.5 lines/min was inserted into the sample mount, in a suitable position, for calibration of the PZT scanner. The sample then was brought in close proximity with the probe and the sample area which was interested was posited under the tip of the probe. The ambient light was shielded on the head to block any stray light from the working environment. The detector was aligned with the reflected laser beam from the probe. The configure parameters of the software and the electronic controller were set for contact attractive mode operation and the images was acquired by the PZT scanner together with the feedback system.

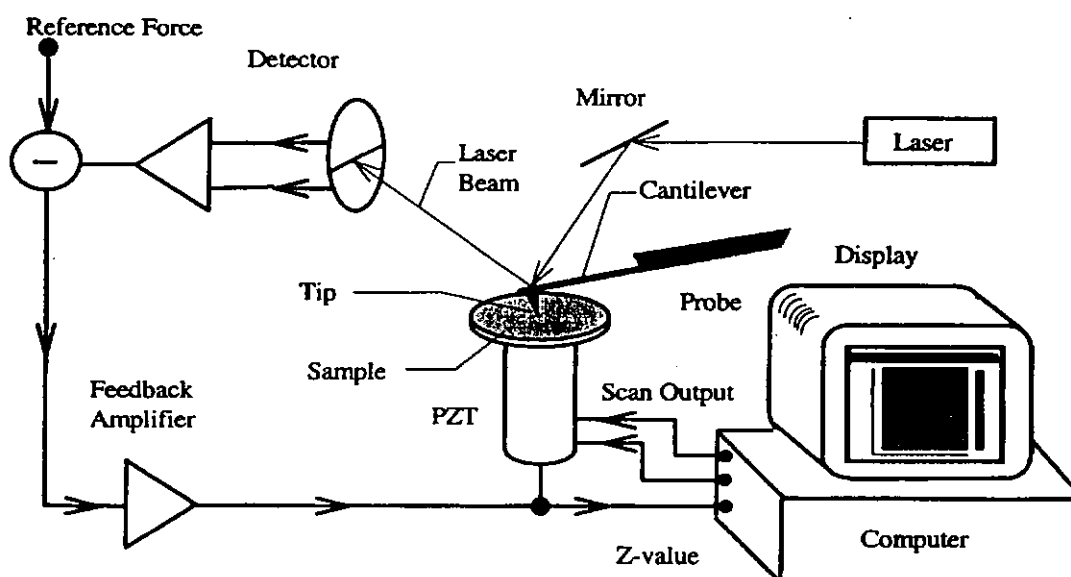


Figure 3.3 Schematic diagram of the atomic force microscope METRIS-2000.

3.6 OPTICAL PROPERTIES MEASUREMENT

The optical properties of the sol-gel derived films of different concentration were measured through spectroscopic phase modulated ellipsometer (UVISEL HR460). The samples were put at the stage and the stage was adjusted to a level that the amplitude of the DC signal (S_0) was at maximum. The incident angle of 70° and incident light of energy range of 1.6eV to 5.0 eV were chosen for our measurement. The refractive index, the extinctive coefficient and hence the complex dielectric function of the samples were obtained.

Chapter 4

Structural Characterisation

4.1 Use of improved solvent

Previously, ethanol was used as the solvent for the preparation of metal alkoxide, which created difficulties in the preparation process. The formation of the ethoxides from metal and ethanol took a long time to complete. Besides, these ethoxide sol required careful handling because of their readiness to hydrolysis during expose to air. Chamber filled with dry argon or nitrogen was needed in order to prevent pre-hydrolysis of the ethoxides. In addition, a chelating agent was added to stabilize the solution and to get rid of any precipitate formed.

In this work, we have shown that methoxyethanol is a superior solvent in preparing the alkoxide sols. The methoxyethoxy-group has more partial negative charges than that of ethoxy group. This makes methoxyethanol a better nucleophilic solvent than ethanol. As a consequence, this results in a much easier alkoxides formation. In addition, no chelating agent is needed to stabilize the solution. Furthermore, owing to the steric hindrance of the more bulky ligands in the case of methoxyethanol, the rate of hydrolysis and condensation are much more under control than that in the case of ethanol. This property allows both the metal methoxyethoxides to be more stable in air and much easier to handle than those do ethoxides.

4.2 Temperature effects

4.2.1 Powders

To study the crystallization behaviors of sol-gel KNSBN, the precursor sols were dried at 100 °C to obtain the dried gels for DTA and TG measurement. Figure 3.1 shows the DTA and TGA curves of $K_{0.2}Na_{0.2}Sr_{0.48}Ba_{0.32}Nb_2O_6$ powders with the heating rate of 10 °C/min. Four anomalies are found at 100 °C, 320 °C, 450 °C and 604 °C on the DTA curve while only two anomalies at 100 °C and 320 °C are observed in the TGA curve. Amorphous powders prepared from precursor solutions still contain a certain amount of water and solvent that are either from precursor or as the by-product of the alcoholysis as well as condensation reactions. As the temperature increased to about 70 °C, which is close to the boiling point of water (100 °C) and 2-methoxyethanol (125 °C), both water and 2-methoxyethanol start to evaporate. As a result, energy is absorbed with a large weight reduction. Hence, an endothermic peak in the DTA curve and a large drop in TGA curve are obtained. As the temperature further increased to ~300 °C, the remained solvent and organic ligand undergoes combustion. In this case, heat is released as well as the weight of the sample is reduced due to the removal of the organic groups. This accounts for the exothermic peak and another large weight drop found in the DTA and TGA curves respectively. This combustion process is completed at ~380 °C.

As the temperature further increased to > 400 °C, an anomaly at 450 °C is observed. Since no weight loss is observed at this temperature, this exothermic peak could not be due to evaporation or combustion. Furthermore from XRD data, we also know that the sample was not crystallized until ~600 °C (Figure 4.2). So this peak is not arisen from crystallization of KNSBN. Furthermore, similar peak in the sol-gel derived

SBN was not observed [4.2]. The main difference between the KNSBN and SBN system is that vacant A sites exist in SBN but not in KNSBN structure. We suggest that this anomaly may be due to a phase transition of the very fine crystallite of the sample. These fine crystallites cannot be detected by XRD because the nuclei size is too small although the number of nuclei can be very large. Finally, an exothermic peak is observed at about 604 °C in the DTA curve. Similarly to the third anomaly, no weight drop is found at this temperature range. Compare to the DTA/TGA data of SBN powders [4.2], we believe that this peak is due to the crystallization of the KNSBN powders. Compare to SBN powder, this crystallization temperature is lower by ~30 °C.

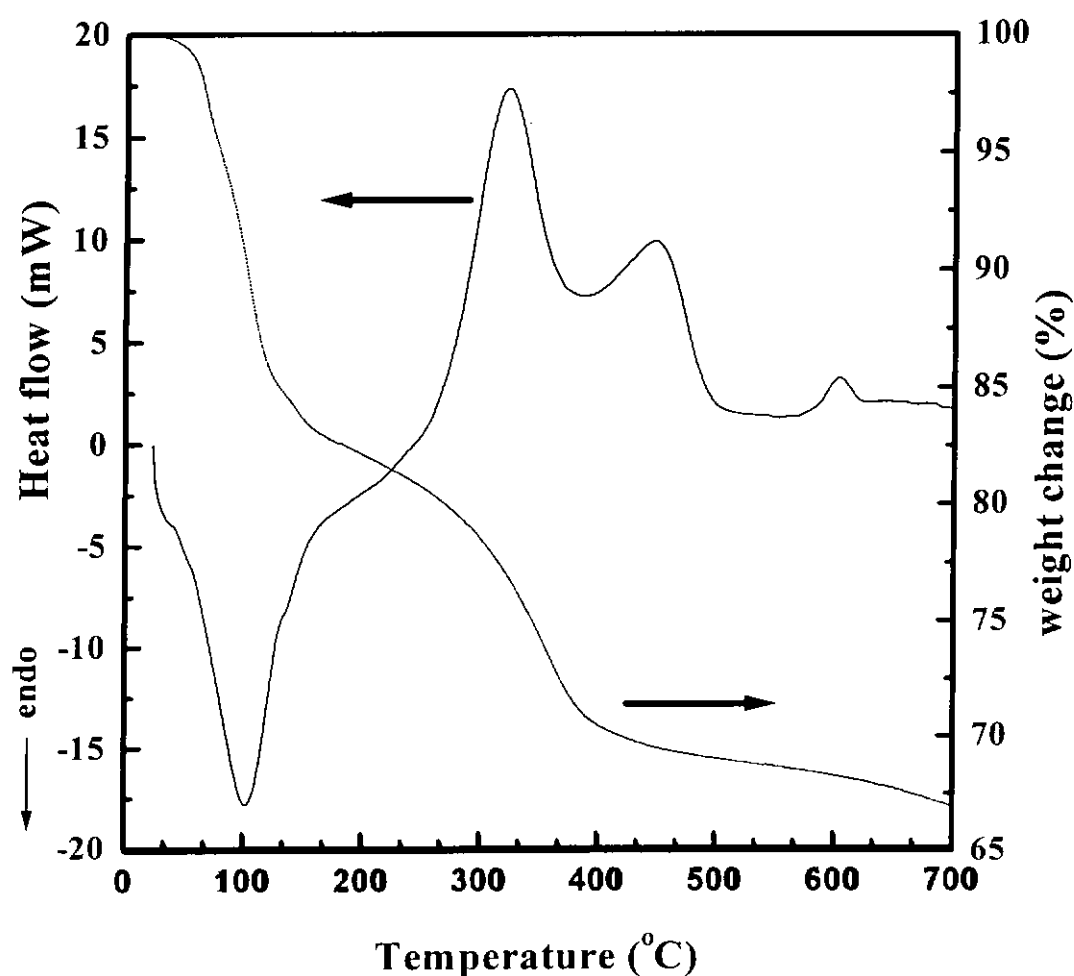


Figure 4.1 DTA (in DSC mode) and TGA curves of $\text{K}_{0.2}\text{Na}_{0.2}\text{Sr}_{0.48}\text{Ba}_{0.32}\text{Nb}_2\text{O}_6$ powders.

Figure 4.2 shows the XRD spectra of the sol-gel derived KNSBN powders with different annealing temperatures. When the annealing temperature is low, ($T_a \leq 500\text{ }^{\circ}\text{C}$) only a broad profile, with full width half maximum (FWHM) = 3.8° , appears at $2\theta = 27.6^{\circ}$ indicating that the sample is still in an amorphous phase. As the temperature increased to $600\text{ }^{\circ}\text{C}$, the sample starts to crystallize with the observation of some diffraction peaks which represent the different orientations of the TTB phase KNSBN crystalline planes [4.1, 4.3]. This crystallization temperature seems to be consisted with the data from DTA result. However, two additional small peaks, at diffraction angle $2\theta = 28.5^{\circ}$ and 29.1° , are also observed in the spectra. These two unwanted peaks are originated from the orthorhombic BN and SN phase [4.2]. This indicates that at low annealing temperature, KNSBN powders consist of both TTB phase KNSBN powder and orthorhombic phase BN and SN powder, i.e. a mixed phase structure. These peaks become weaker as the annealing temperature increased to $1000\text{ }^{\circ}\text{C}$. At $1200\text{ }^{\circ}\text{C}$, the two orthorhombic peaks disappear, indicating that the powder is completely converted into the TTB phase KNSBN structure. Table 3 summarizes the feature of XRD spectra at different annealing temperature.

Temperature ($^{\circ}\text{C}$)	Observation	Explanation
500	Broad profile with peak position of $2\theta = 27.6^{\circ}$ & FWHM = 3.8°	Amorphous phase
600	Characteristic KNSBN peaks as well as peaks at $2\theta = 28.5^{\circ}$ and $2\theta = 29.1^{\circ}$ appeared	Mixed phases of orthorhombic phase SN and BN phases as well as TTB phase KNSBN structure
800	The orthorhombic peaks still present	Mixed phases of orthorhombic phase SN and BN phases as well as TTB phase KNSBN structure
1000	The orthorhombic peaks turns weak	Orthorhombic phase SN and BN transfer to TTB phase KNSBN
1200	The orthorhombic peaks disappear	Complete TTB phase KNSBN structure

Table 3 Summary of the features of XRD spectra of KNSBN powders.

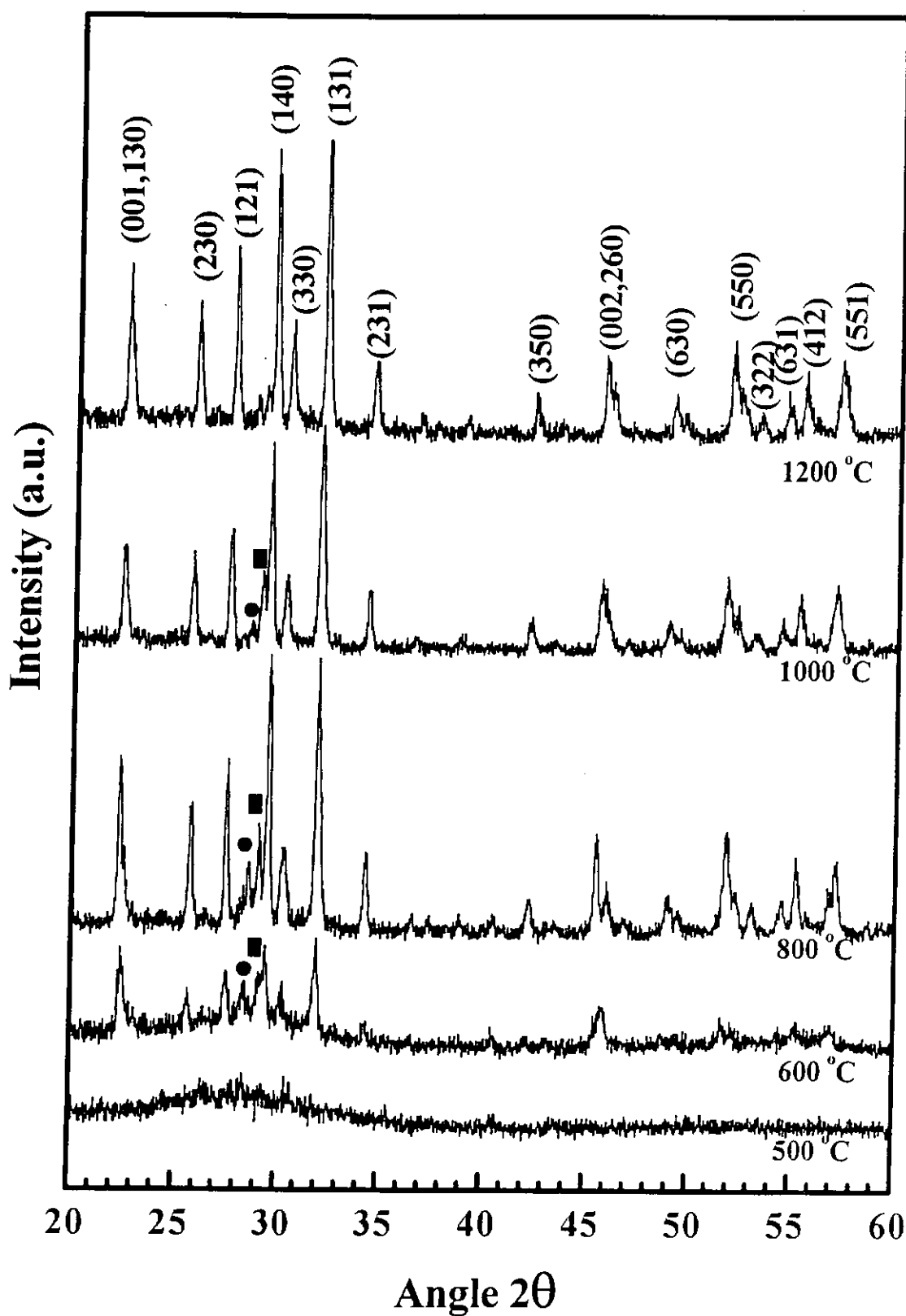


Figure 4.2 XRD spectra of KNSBN powders annealing at different temperatures. ● is the orthorhombic BN phase and ■ is the orthorhombic SN phase.

Figure 4.3 shows the Raman spectra of KNSBN powders annealed at different temperatures. When the annealing temperature is 500 °C, a very broad peak at $\sim 640\text{ cm}^{-1}$ (FWHM = 165.3 cm^{-1}) is observed. This indicates that the samples are still amorphous in nature. This is consistent with the DTA as well as XRD data. As the temperature increased to 600 °C, crystallization starts with the observation of two weak and broad $A_1(\text{TO})$ phonons at about 266 cm^{-1} and 650 cm^{-1} . According to the spectrum given by Amzallag et. al. [4.4], these two peaks represent the deformation vibration of the niobium oxides framework. In addition to these two broad peaks, small peaks at 185 cm^{-1} , 429 cm^{-1} , 580 cm^{-1} and 688 cm^{-1} are also observed. These peaks are assigned as the phonon peaks of orthorhombic SN/BN peaks [4.2]. Similar to XRD data, these results confirm that the powders are in a mixed phase structure. At higher annealing temperature (800 °C), the two peaks at 266 cm^{-1} as well as 650 cm^{-1} are enhanced while the orthorhombic SN/BN phonon peaks get weaker. Furthermore, an additional peak at 730 cm^{-1} is observed. This peak represents the edge shared octahedral NbO_6 stretching mode of the species [4.5]. At 1000 °C, the Raman peak at 650 cm^{-1} shifts its position to about 646 cm^{-1} . This shifting of the peak indicates that the orthorhombic SN phase of the sample (phonon mode at 650 cm^{-1}) turns weak and the TTB phase KNSBN structure (with phonon mode at 646 cm^{-1}) dominated [4.2, 4.6, 4.7]. As the annealing temperature increased to 1200 °C, Raman spectrum similar to KNSBN single crystal is obtained [4.7]. Similar to XRD spectra, this indicates that crystallization process of TTB phase KNSBN completed with the annealing temperature higher than 1000 °C. Table 4 summarizes the changes of Raman spectra as a function of temperature.

Therefore, from both the Raman and XRD data, we suggest that at annealing temperature as low as 600 °C, KNSBN starts to crystallize with a mixed phase structure and fully convert into TTB phase with temperature larger than 1000 °C.

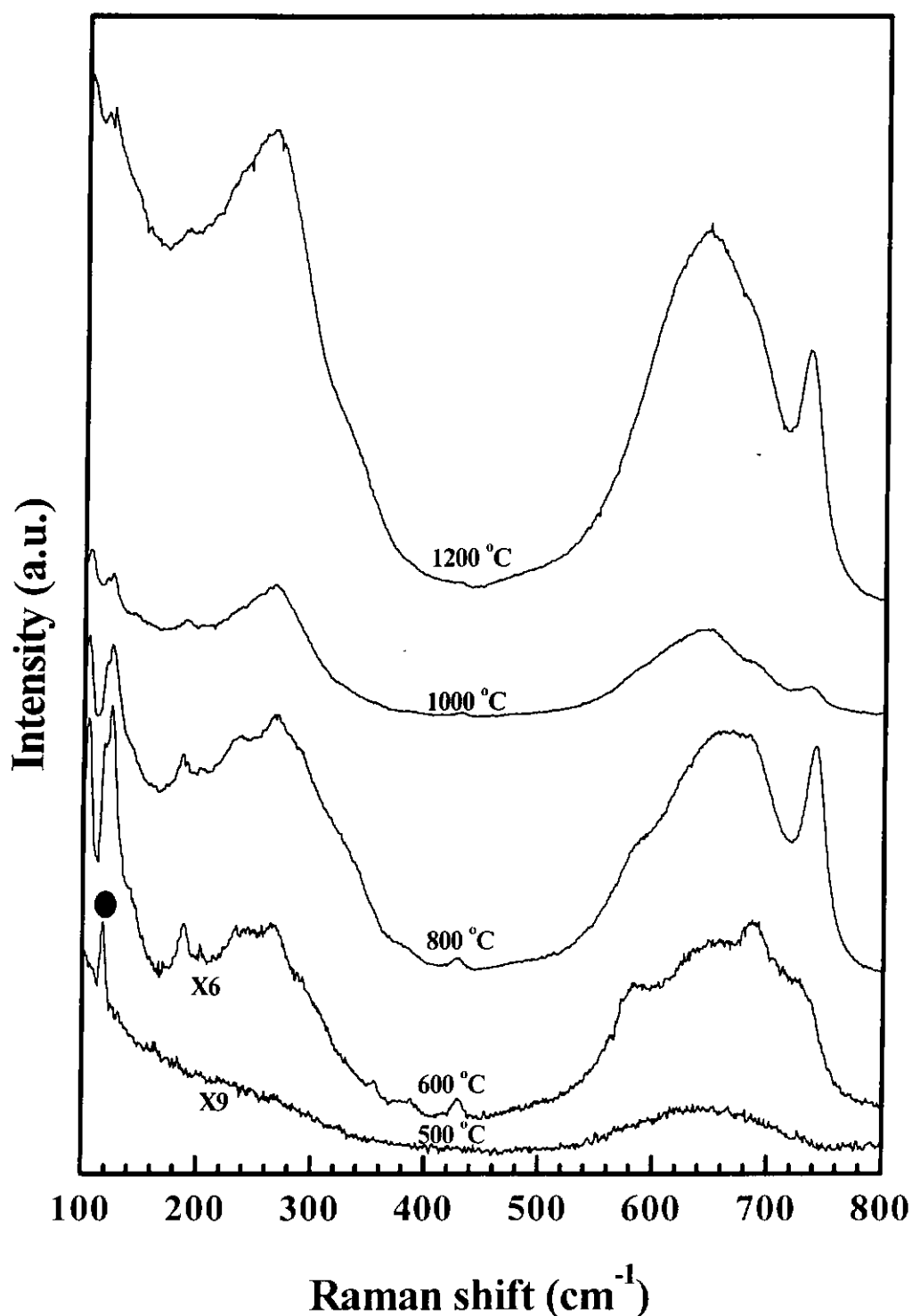


Figure 4.3 Room temperature Raman spectra of KNSBN powders annealing at different temperatures. ● is the plasma line of the laser. The factor on the left of each spectrum $\times 6$ etc., means that the spectrum has been enlarged by six times compared to other spectra.

Temperature (°C)	Observation	Explanation
500	A very broad peak observed	Amorphous phase
600	Broad phonons at 266 cm^{-1} and 650 cm^{-1}	Both TTB phase KNSBN and orthorhombic phase BN & SN start to crystallize
800	KNSBN peaks get stronger SN/BN peaks get weaker	Mixed phase of orthorhombic SN/BN and TTB phase KNSBN structure
1000	Shift of the peak from 650 cm^{-1} to 646.2 cm^{-1}	SN and BN phase turns to TTB phase KNSBN structure
1200	Strong KNSBN peaks remain	Complete formation of TTB phase KNSBN structure

Table 4 Summary of the features of Raman spectra of KNSBN powders.

4.2.2 Films

Figure 4.4 is the XRD patterns of the sol-gel KNSBN films deposited on (100)Si, with different annealing temperatures. The sol concentration used is 0.21M with 0.3 cm/sec drawing rate. The number of dip coated layers is three. For each dip-coated layer, it was air dried for about 20 minutes. The total thickness of the films is estimated to be ~300 nm using ellipsometry. At low annealing temperature ($\leq 550\text{ }^{\circ}\text{C}$), only a broad profile appears at $2\theta = 27.6^{\circ}$ (FWHM = 7°). Similar to the KNSBN powders, this broad profile is due to the presence of amorphous KNSBN structure [4.8]. When the temperature is raised to $600\text{ }^{\circ}\text{C}$, sharp characteristic KNSBN peaks are observed, indicating that the samples start to crystallize. As the temperature increases to $\geq 700\text{ }^{\circ}\text{C}$, the peaks become narrower which indicates that the amorphous phase completely transfer to the TTB phase KNSBN structure. Table 5 shows the change of the FWHM of the XRD diffraction peaks as a function of temperature. The FWHM get

narrower with increasing temperature i.e. the crystallinity improved with annealing temperature. Nevertheless, the annealing temperature, beside affecting the degree of crystallization, also affects the interface of the substrate and film.

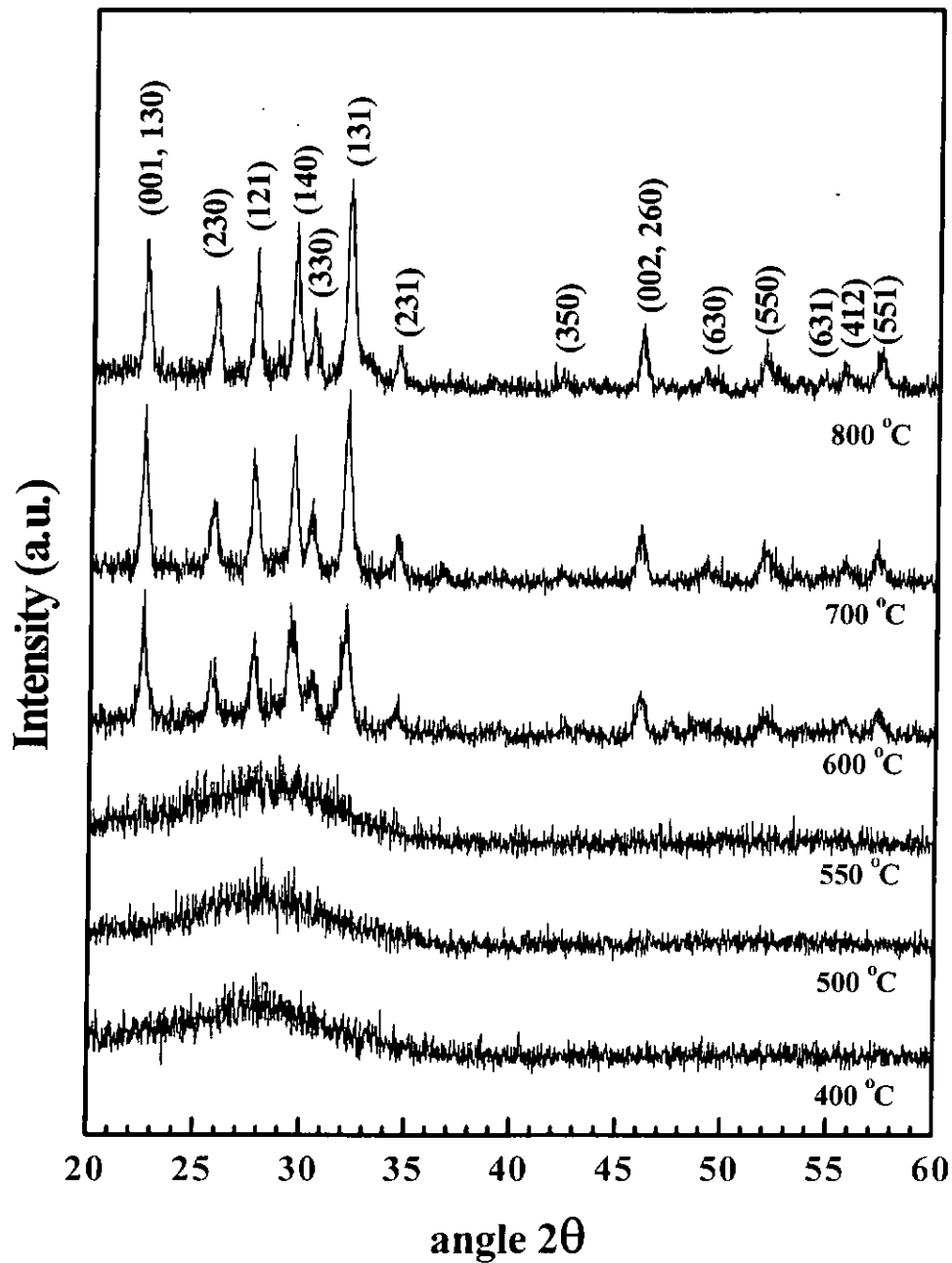


Figure 4.4 XRD spectra of 0.21M, 3 layers dip-coating KNSBN films annealing at different temperatures.

Diffraction peak	FWHM (degree) at 600 °C	FWHM (degree) at 700 °C	FWHM (degree) at 800 °C
(001, 130)	0.36°	0.40°	0.37°
(121)	0.40°	0.37°	0.34°
(140)	0.86°	0.35°	0.34°
(131)	0.51°	0.39°	0.39°

Table 5 FWHM of XRD diffraction peaks as a function of temperature.

The Raman spectra of these films are shown in Figure 3.5. At low annealing temperature, only a strong and sharp peak corresponding to the phonon peak of single crystal Si substrate is observed at 523 cm^{-1} . When the temperature is raised to 500 °C, three additional broad peaks with Raman shift at 267 cm^{-1} , 671 cm^{-1} and 821 cm^{-1} and a broad background are observed. These peaks indicate the presence of orthorhombic SN structure [4.6]. The broad feature underneath of these Raman bands is a result of the structure of the amorphous niobium oxides [4.5]. As the temperature increased to 550 °C, the peak of 671 cm^{-1} shifts to lower wave-number side and becomes sharper in shape. The shifting of the peak can be expressed as the transformation of orthorhombic SN phase (671 cm^{-1}) to TTB phase KNSBN phase (640 cm^{-1}) [4.6, 4.7]. More significant shift in the phonon peak can be observed when the temperature raise to 600 °C. At this temperature, the peak of 821 cm^{-1} (orthorhombic SN phase) disappears and both the peaks at 267 cm^{-1} and 671 cm^{-1} become sharper and more pronounce. The peak position of the 671 cm^{-1} phonon mode shifts to 640 cm^{-1} . Different from powders, no 731 cm^{-1} peak is observed in our film. As the temperature increase above 700 °C, no significant change is observed indicating that the crystallization process becomes completed. Table 6 summarizes the change of features as a function of temperature.

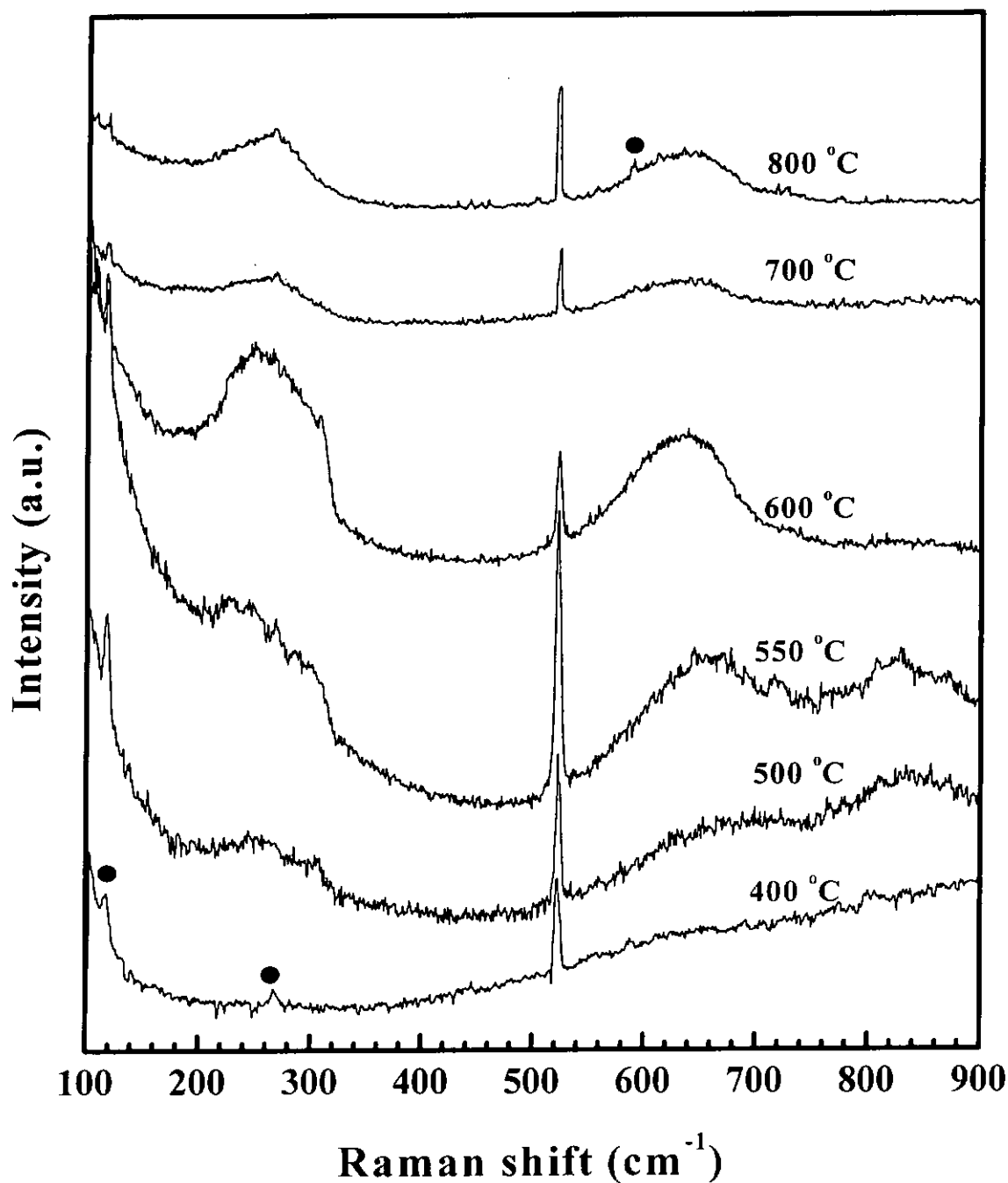


Figure 4.5 Room temperature Raman spectra for 3-layer dip-coated KNSBN films with sol concentration equals to 0.21M. Different annealing temperatures are indicated at the right of the figure. ● is the plasma line of the laser.

Temperature (°C)	Peak positions of the Raman bands (cm ⁻¹)	Explanation
400	No peak	Amorphous phase
500	(1) 267 (2) 671 (3) 821	Start to crystallize (1) corresponding to TTB KNSBN phase, (2) and (3) corresponding SN phase.
550	267, 664 and 821	Start to transfer SN phase to TTB KNSBN structure
600	267, 640	Orthorhombic SN phase disappear
≥ 700	267, 640	Complete crystallization, pure TTB phase KNSBN

Table 6 The variation of peak position of the Raman bands at different annealing temperatures.

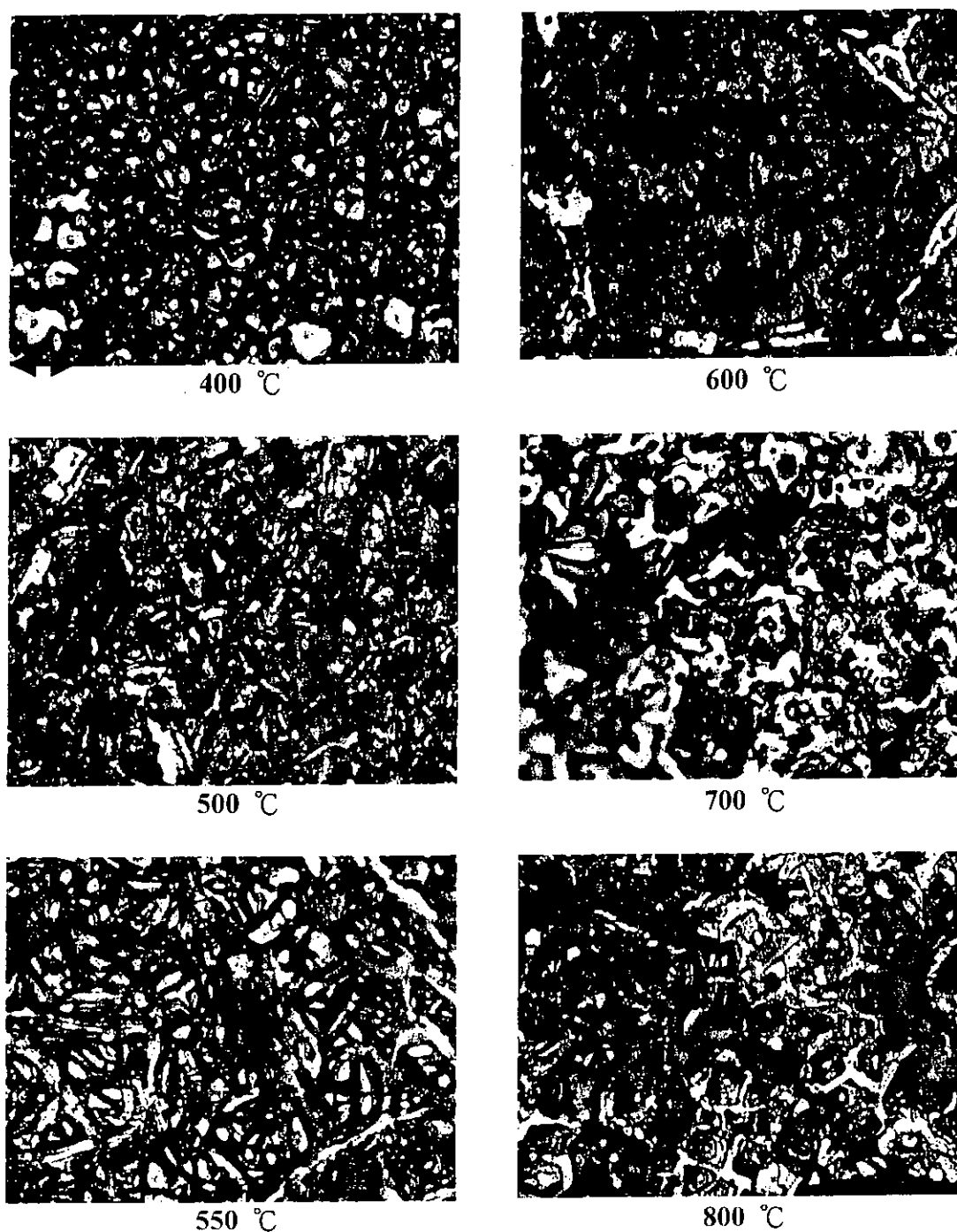
From the Raman data, we conclude that the KNSBN films start to crystallize at an annealing temperature as low as 550 °C and complete the phase transformation at temperatures ≥ 600 °C. In comparison, these temperatures are lower than these of SBN by 50 °C which is about the same as obtained in DTA data.

Compare with powders, the orthorhombic-tetragonal phase transition temperature (film : ≥ 550 °C , powder : ≥ 1000 °C) and the crystallization temperature for the films (film : ≥ 500 °C, powder : ≥ 600 °C) are lower. The reason for this phenomenon is due to the substrate effect. For the films, (100)Si is cubic structure of which the lattice constants have the relation of $a = b = c$. So, KNSBN, with a tetragonal structure and lattice constants of $a = b \neq c$, are more favorable to grow on the (100)Si substrate than the orthorhombic SN or BN structure which are distorted tetragonal structure. Hence the orthorhombic-tetragonal phase transition temperature of the film

is lower than that of powders. Similar, this substrate forms an initial lattice (nucleation site) for the coated sol to crystallize. Therefore the energy required for forming crystallized grains is less than that of powders i.e. the thermal energy need to complete the crystallization process is less for the films.

For both Raman and XRD spectra, we observed that higher annealing temperature results in higher degree of crystallization. However, higher annealing temperature will also enhance larger interfacial interaction between substrate and films. For Si, with temperature higher than 800 °C, Si will start to diffuse into the KNSBN films. From Raman as well as XRD data, we reveal that for annealing temperature ≥ 700 °C, the films already have a good crystallinity. Therefore, in the remaining experiments, we will fix our annealing temperature to be 700 °C.

The change of the surface morphology of these films with different annealing temperature was observed by optical microscope. Figure 4.6 shows the 400X optical microscope images of the KNSBN films with different annealing temperature. In general, no crack is observed in all of the films. When the annealing temperature is 400 °C, dense and uniform micro-regions of size $50 \mu\text{m}^2$ are observed. As the temperature increase, these micro-regions become larger. The increasing of the micro-region size with annealing temperature can be explained as more energy provided for the growth of grain as the annealing temperature increased. This grain growth process will result in increasing of the surface roughness. This hypothesis is confirmed with those for the PZT film.



* \longleftrightarrow represented $100\ \mu\text{m}$ for both vertical and horizontal axis

Figure 4.6 Surface morphology of 3 layers KNSBN films annealed at different temperature. The sol concentration is 0.21 M and the magnification of the optical image is 400X.

4.3 Thickness effect

KNSBN films of 1-layer, 2-layer, 5-layer and 10-layer with single annealing cycle were measured through XRD (Figure 4.7) and AFM (Figure 4.8 (a) and (b)). The sol concentration is 0.03M, withdraw rate is 0.3 cm/sec and the annealing temperature is 700 °C for 2 hours. Base on the ellipsometer data (chapter 5), the average thickness of each single dip-coated layer is estimated to be ~30 nm. In this case, the thickness of the 10-layer film is therefore ~300 nm.

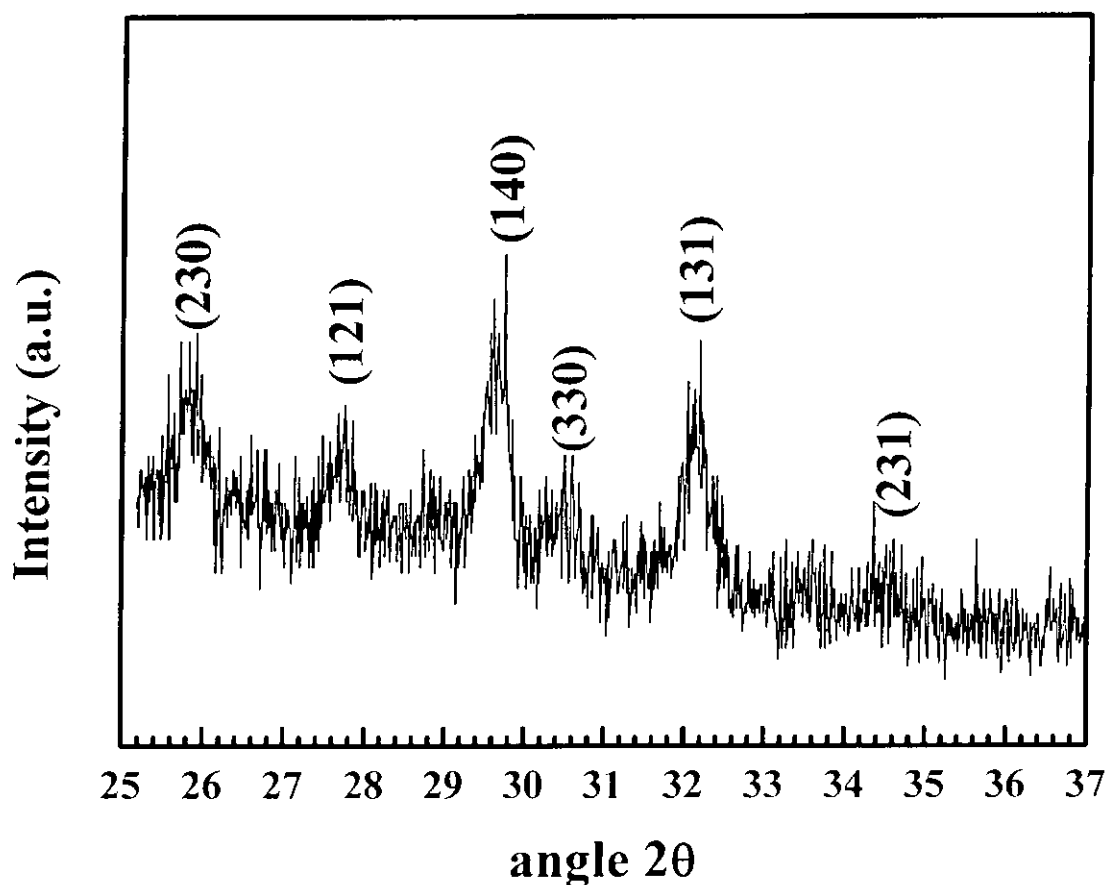


Figure 4.7 XRD spectrum of 10-layer KNSBN film with single annealing cycle. The sol concentration of dip coating is 0.03M, withdraw rate is 0.3 cm/sec and the annealing temperature is 700 °C for 2 hours.

From Figure 4.7, the orthorhombic SN or BN phases are not observed. This implies that, for 10-layer KNSBN film, completely crystallized TTB structure can be obtained in single annealing cycle. However, the thickness of the 5-layer, 2-layer and 1-layer films are too thin, their corresponding XRD spectra are too weak to be detected. As well crystallized TTB phase KNSBN can be obtained in 10-layer film, we believe that the TTB phase KNSBN should be also obtained in 5-layer, 2-layer and 1-layer films.

Figure 4.8(a) and (b) shows the AFM images of these films for scanning area of $10\ \mu\text{m} \times 10\ \mu\text{m}$ and $5\ \mu\text{m} \times 5\ \mu\text{m}$ respectively. The surface of the films are, in general, dense and crack free. Surface profiles reveal root-mean square roughness value of 15 and 50 nm for 1-layer and 10 layer film ($5 \times 5\ \mu\text{m}^2$ scan are) respectively. Thicker films show an irregular grain growth with severe grain agglomeration. As film thickness decreases, the film surfaces show an improved top layer quality with more uniformly distribution grain size of $\sim 100\ \text{nm}$. The shape of the grain is more spherical with no sign of grain agglomeration. Figure 4.9(a) and (b) shows the relationship between the number of layers (thickness) and the root mean square roughness (R_q) of the films. The root mean square roughness, R_q , are calculated from the formula

$$R_q = \sqrt{\frac{1}{N} \sum_i^N (Z_i - Z_{\text{avg}})^2} \quad (4.1)$$

where Z_i is the height of the scanned surface at particular point;

Z_{avg} is the average height of this surface; and

N is the total number of points that were scanned.

Figure 4.10 shows the relationship between number of layers (i.e. thickness) and the grain size. The grain size is measured from the cross-section profiles of the

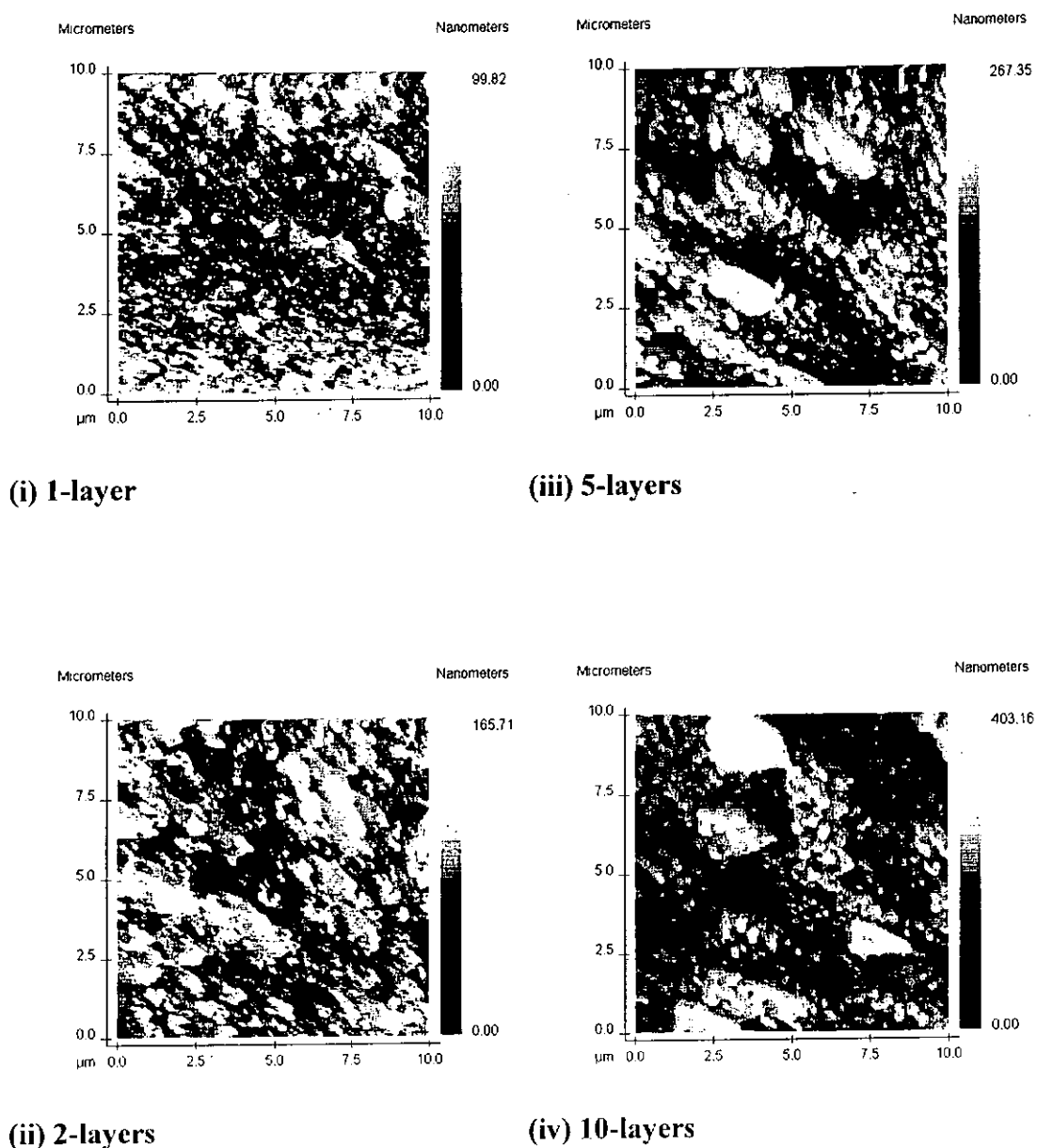
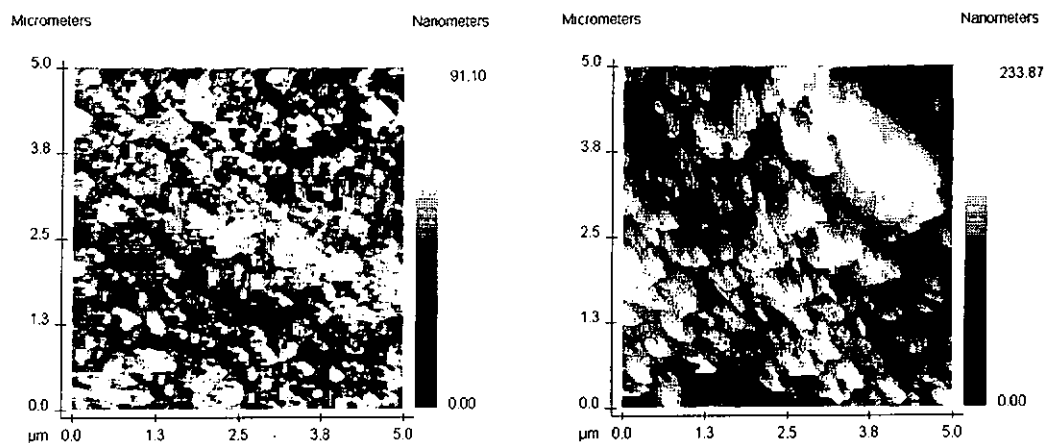
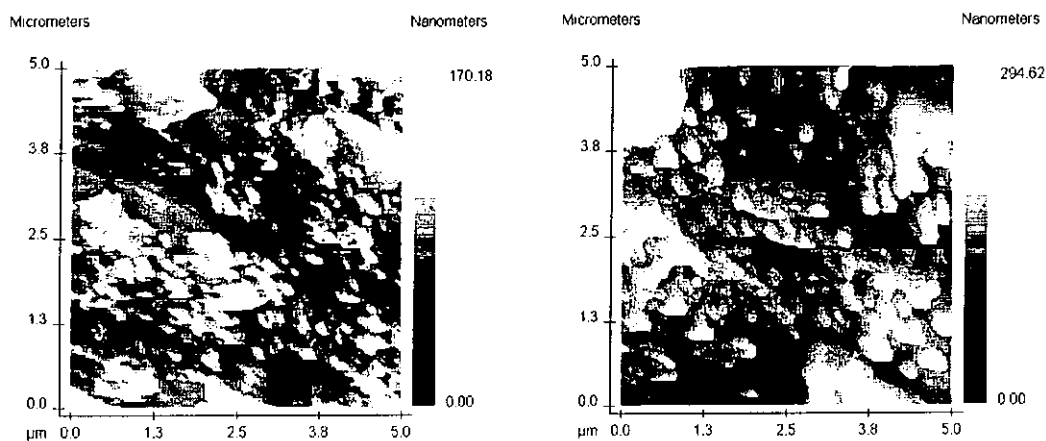


Figure 4.8(a) AFM images of KNSBN films with different number of layers of single annealing cycle. The sol concentration used is 0.03 M and the scan area is 10 μm × 10 μm.



(i) 1-layer

(iii) 5-layers



(ii) 2-layers

(iv) 10-layers

Figure 4.8(b) AFM images of KNSBN films with different number of layers of single annealing cycle. The sol concentration used is 0.03 M and the scan area is 5 μm × 5 μm.

AFM images. From Figures 4.9 and 4.10, we know that as the thickness of the film increases, the surface roughness and the grain size increase. Between subsequence layer, the films were only dried in air, hence a lot of sol as well as precursor remained. In the final annealing process, the thicker layer had a larger amount of sol to be evaporated or undergone combustion with the release of H_2O and CO_2 vapour. As a result, more porous will be resulted and this would lead to a rougher surface. On the other hand, the increase of the grain size can be explained as the decrease of the constraint along the vertical dimension. This results in more space for grain growing. The increase of the thickness (number of layers) implies increase of the volume for growth of the grain. Hence, as the thickness of the film increases, the grain size increases. Besides, the more spherical shape of the grain as the thickness increased can be expressed as the absent of the grain agglomeration and coarsening which can be occurred in the case of irregular grain growth of the thinner films [4.9]. This causes the microstructure of the thinner films to become more homogeneous with smaller surface roughness.

Compare to layer-by-layer growth process [4.10] in which each subsequence layer has its only annealing cycle, the films obtained by this multi-layer growth process seem to have a poorer structural properties. The layer-by-layer growth process resulted in a progressively improved crystalline structure from bottom to top. An increased grain size, lower surface roughness and decreased porosity could be obtained. On the other hand, with this multi-layer growth process, the grain size seems enlarged and the surface roughness is increased. This amplification in surface roughness will hinder the film for device applications. This result suggests that the layer-by-layer growth process will be better than the multi-layer growth process.

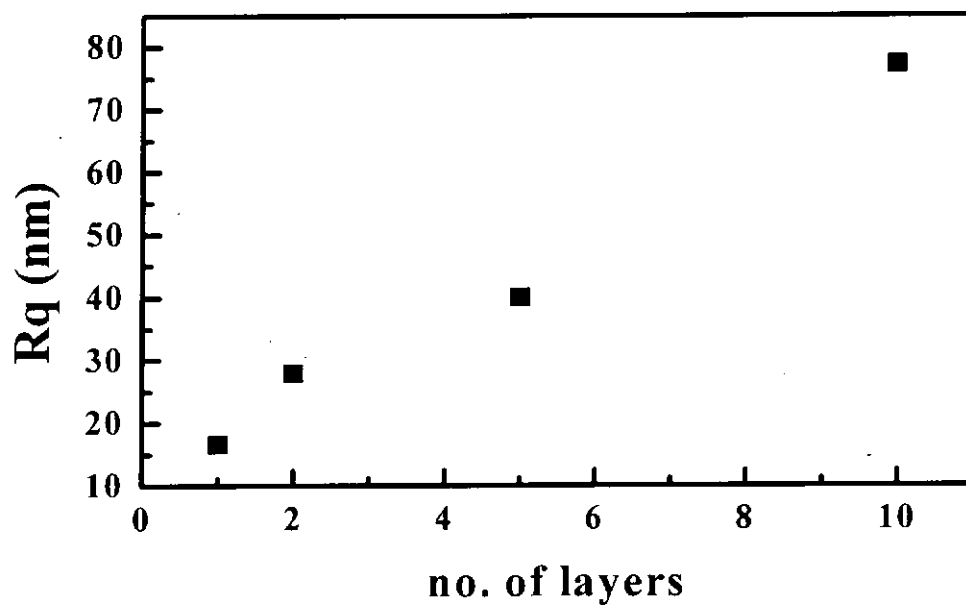


Figure 4.9(a) The relation between number of layers and surface roughness. The scan area is $10\ \mu\text{m} \times 10\ \mu\text{m}$.

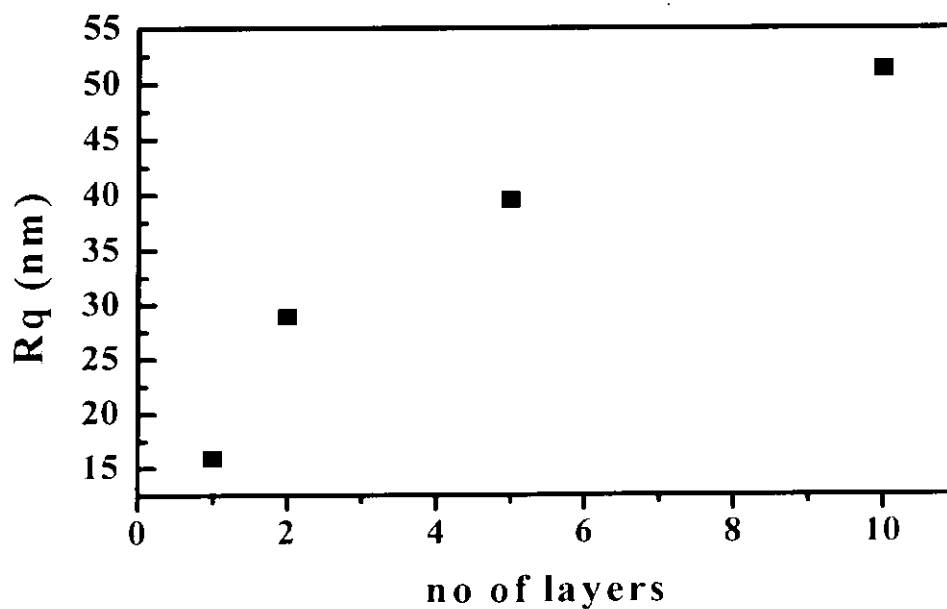


Figure 4.9(b) The relation between number of layers and surface roughness. The scan area is $5\ \mu\text{m} \times 5\ \mu\text{m}$.

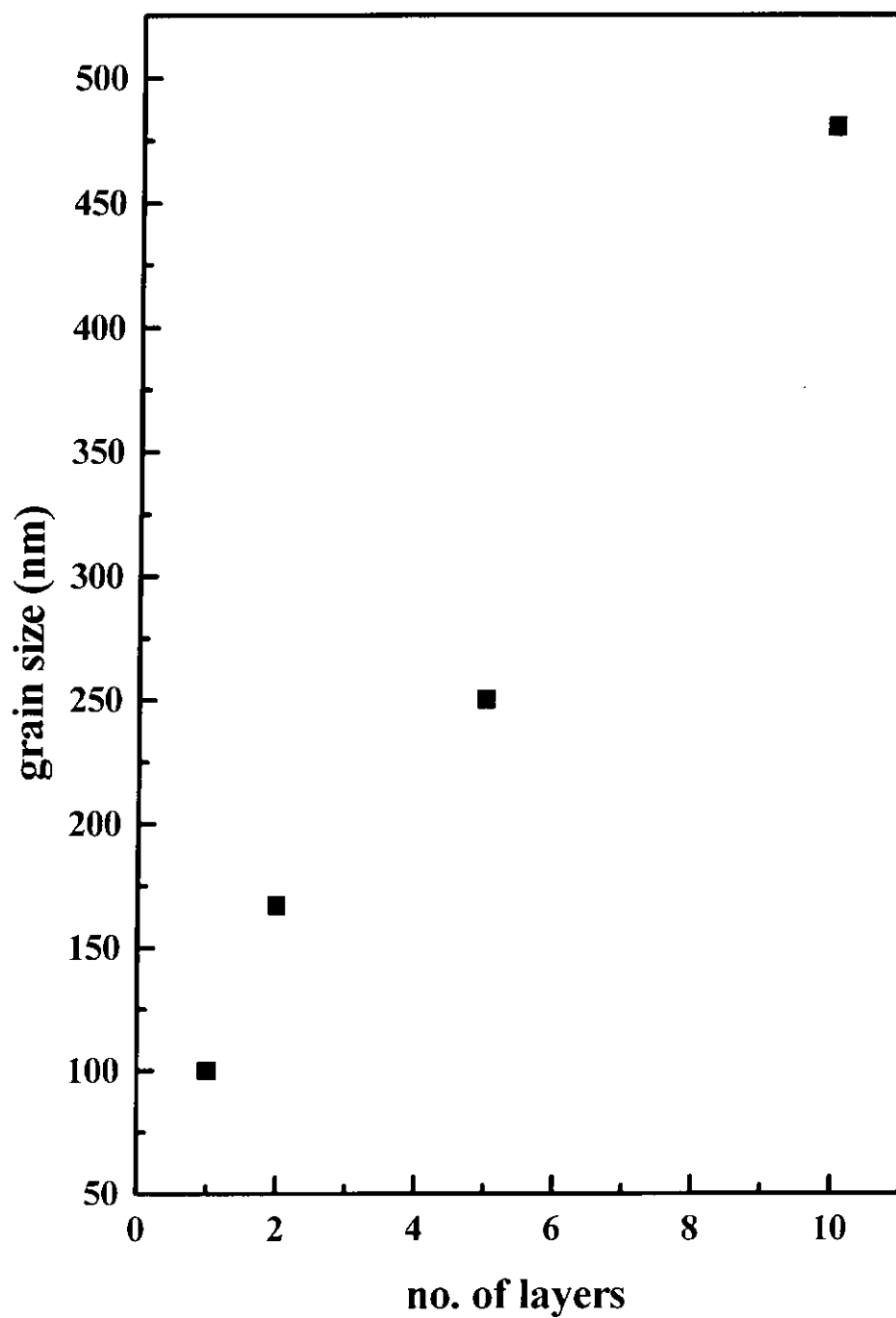


Figure 4.10 The relation between number of layer and grain size.

4.4 Concentration effect

Figure 4.11 is the XRD spectra of single layer KNSBN films with sol concentration of 0.18 M. The films had a drawing rate fixed at 0.3 cm/sec and were annealing at 700 °C for 2 hours. However, with the small thickness of the films, the XRD patterns of lower sol concentration are too weak to be observed. Similar to the thickness effect, we believe that TTB type KNSBN should be obtained in all of the films.

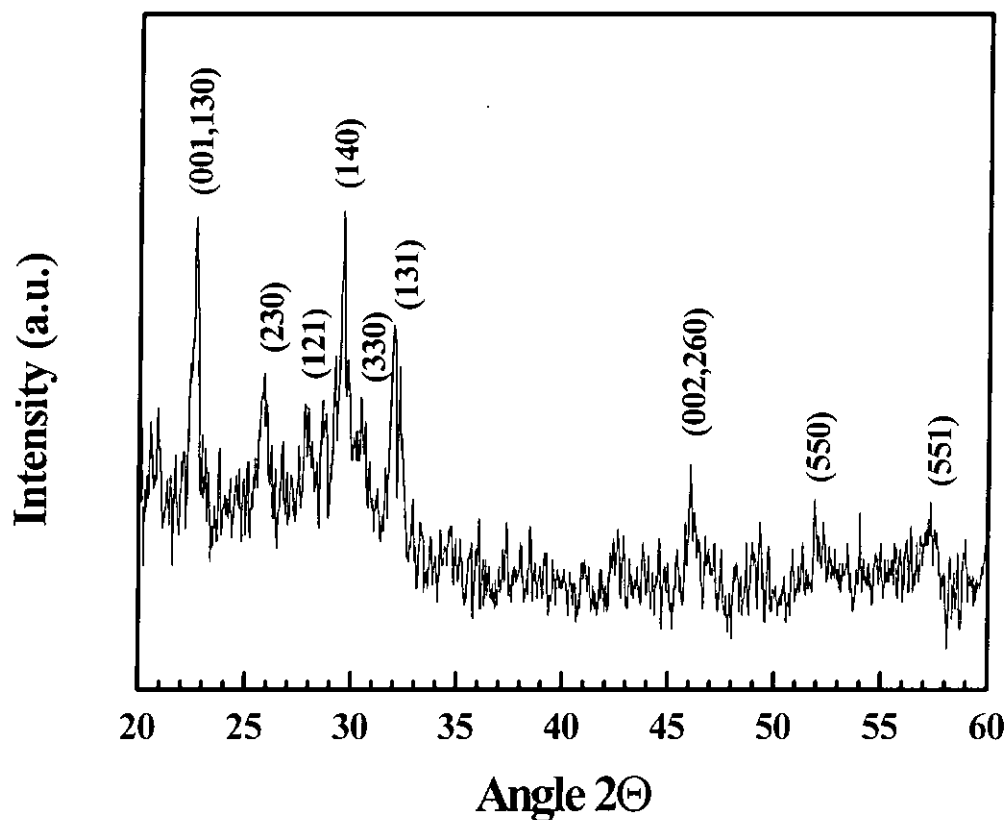


Figure 4.11 XRD spectrum of single layer KNSBN films with sol concentration = 0.18 M for dip coating. The annealing temperature is 700 °C for 2 hours.

Figure 4.12 shows the AFM images of these KNSBN films using different scan areas of $25\ \mu\text{m} \times 25\ \mu\text{m}$, $10\ \mu\text{m} \times 10\ \mu\text{m}$, $5\ \mu\text{m} \times 5\ \mu\text{m}$ and $2\ \mu\text{m} \times 2\ \mu\text{m}$. Similar to previous section (p.88), we measured the surface roughness as well as the grain size of the KNSBN as a function of sol concentration. Figure 4.13 are the graphs showing the relationship between sol concentration and the surface roughness (R_q) for large scanning areas. The relation between sol concentration and grain size is plotted in Figure 4.14.

From Figure 4.12(a), we can see that when the sol concentration (η) is larger than 0.18M, i.e. $\eta \geq 0.18\text{M}$, micro-cracks are observed in the sol-gel films. The reason account for this phenomenon is possible due to the fact that (1) with high concentration, the thickness of sol coated on the substrate will be increased. In the drying and annealing process, the volume change will be much larger resulted in a large internal stress built within the film; (2) the grain size seems to be increase with sol concentration. The increase of grain size may be due to agglomeration or coarsening of small grain. This coarsening of small grain may result in microcracks. Comparing the AFM images with different scan areas, we observed that as the sol concentration increases, the grain size, in general, increases (Figure 4.14). At the same time, the grains become more irregular with wider size distribution. For smaller sol concentration, the grains are smaller, more spherical with a more uniform size distribution. No sign of grain agglomeration is observed. Hence, films with smaller sol concentration have a smoother surface with a lesser surface roughness. From Figure 4.13, we notice that the surface roughness increase with sol concentration. The steep rise of surface roughness for film with sol concentration 0.18 M is due to the microcracks.

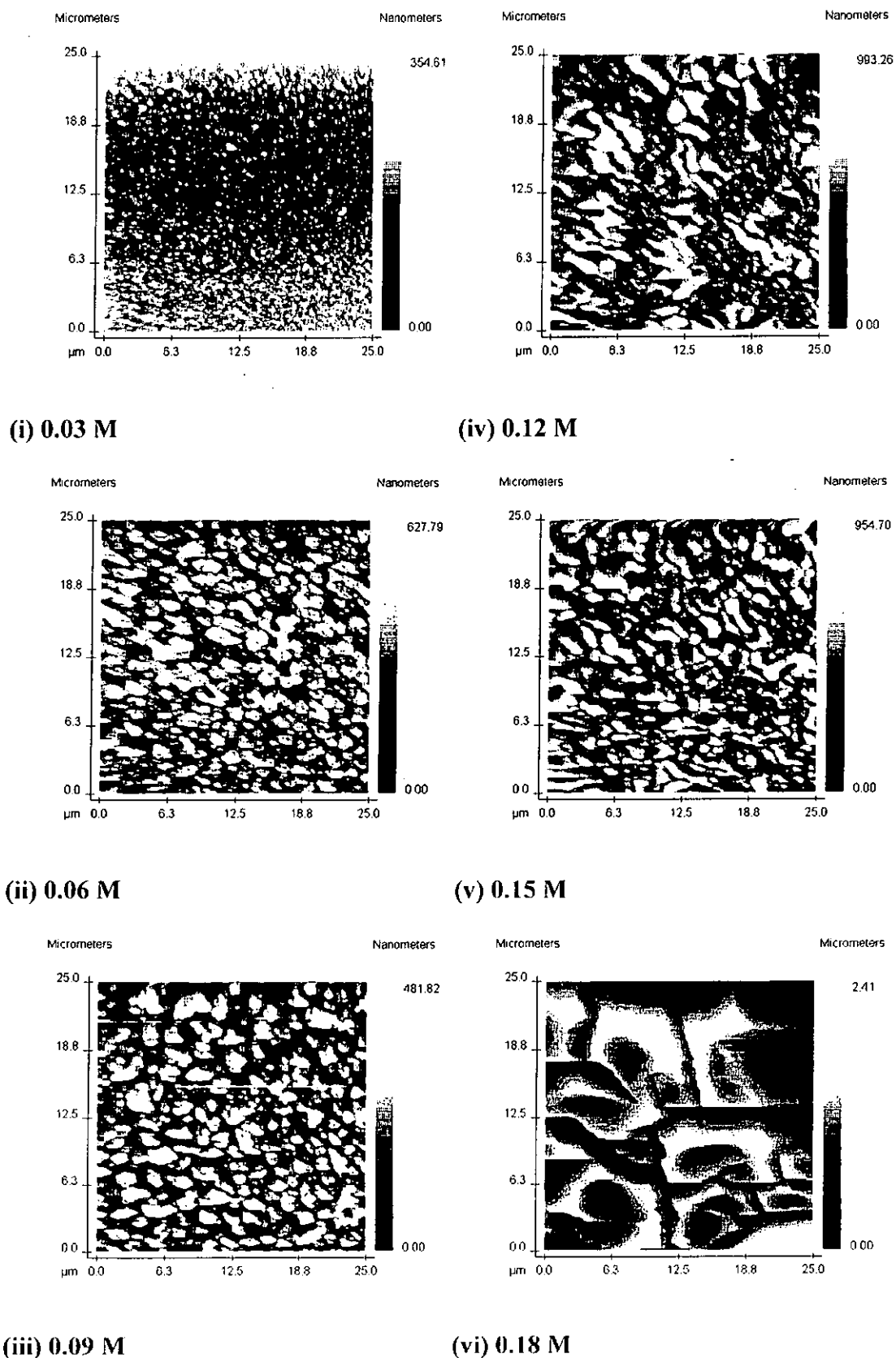
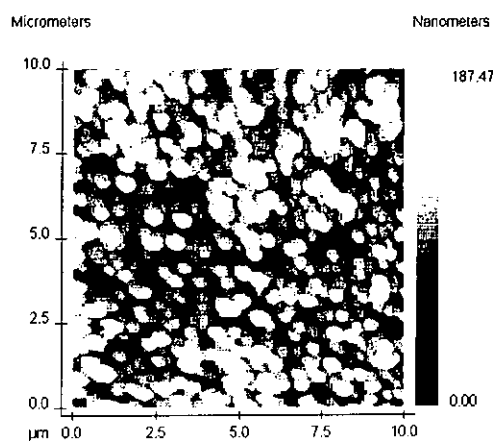
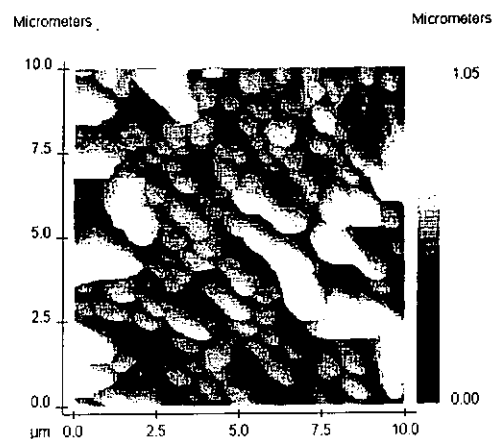


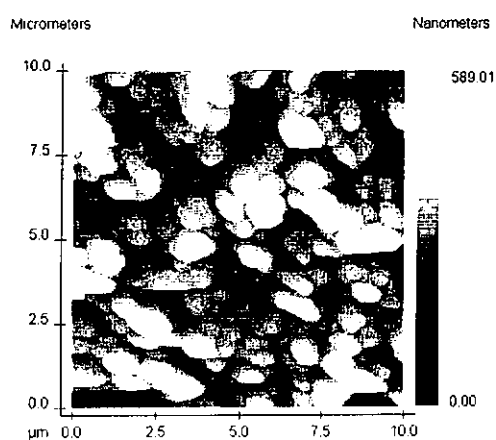
Figure 4.12(a) AFM images of KNSBN single layer films with different sol concentration of (i) 0.03 M (ii) 0.06 M (iii) 0.09 M (iv) 0.12 M (v) 0.15 M and (vi) 0.18M. The scan area is 25 μm × 25 μm.



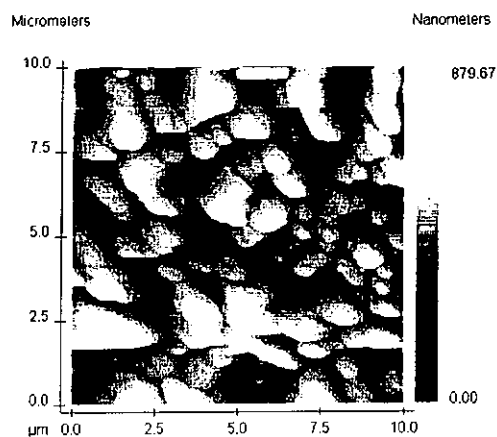
(i) 0.03 M



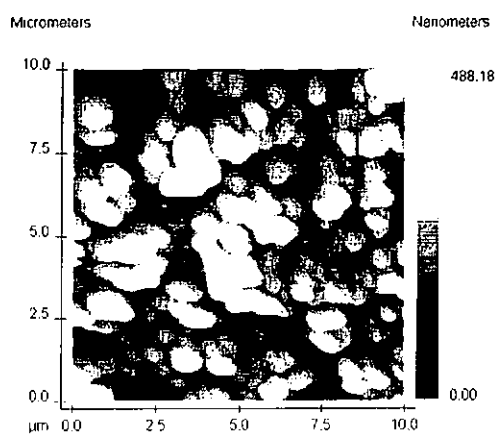
(iv) 0.12 M



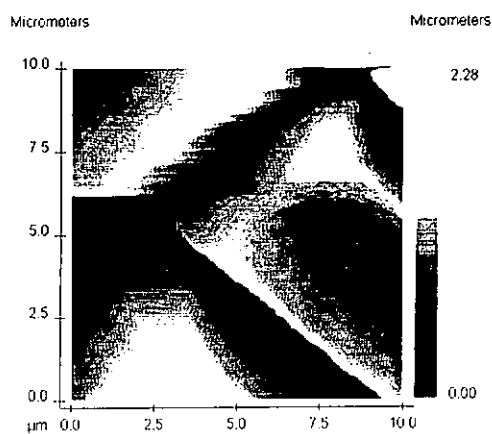
(ii) 0.06 M



(v) 0.15 M

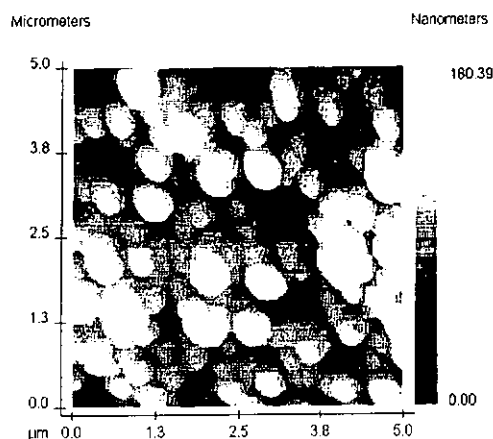


(iii) 0.09 M

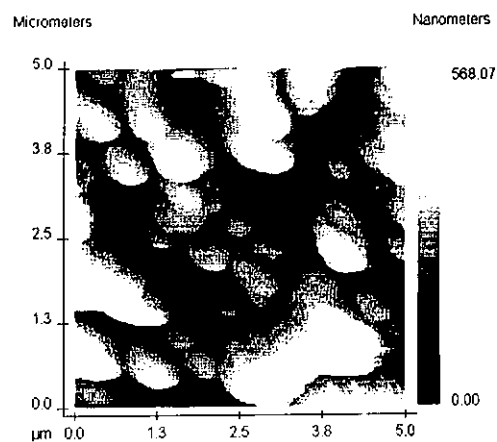


(vi) 0.18 M

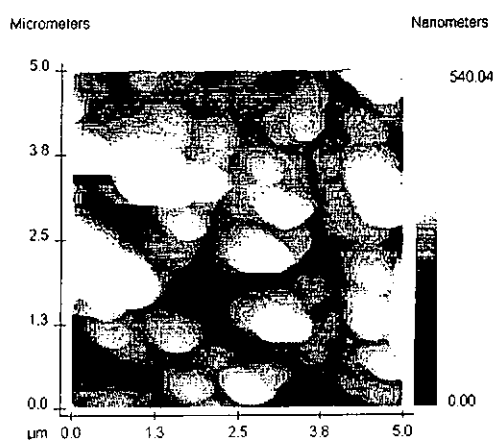
Figure 4.12(b) AFM images of KNSBN single layer films with different sol concentration of (i) 0.03 M (ii) 0.06 M (iii) 0.09 M (iv) 0.12 M (v) 0.15 M and (vi) 0.18 M . The scan area is $10\ \mu\text{m} \times 10\ \mu\text{m}$.



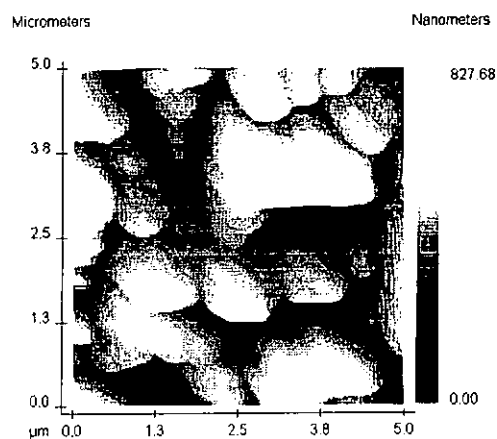
(i) 0.03 M



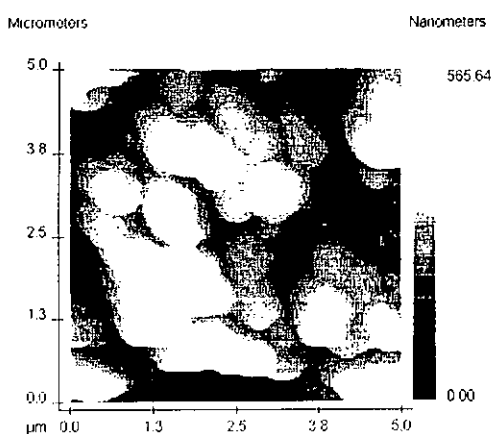
(iv) 0.12 M



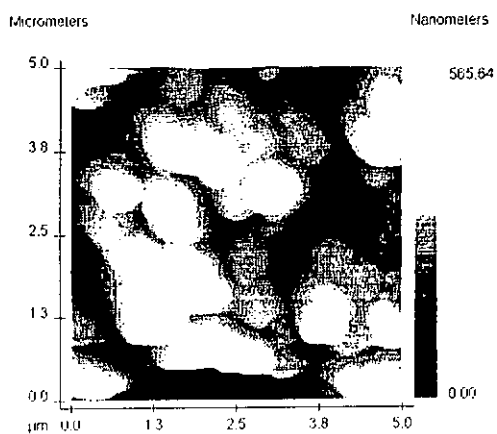
(ii) 0.06 M



(v) 0.15 M

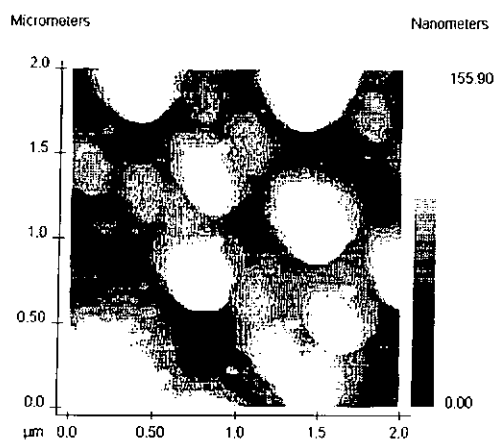


(iii) 0.09 M

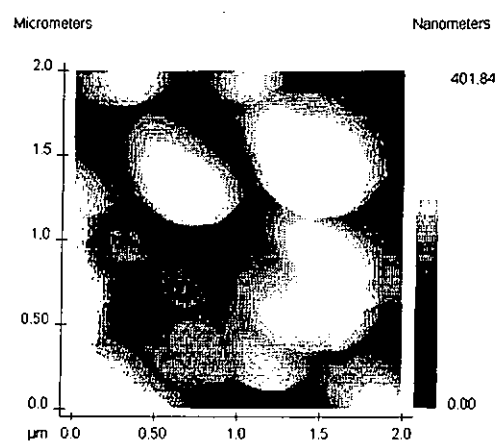


(vi) 0.18 M

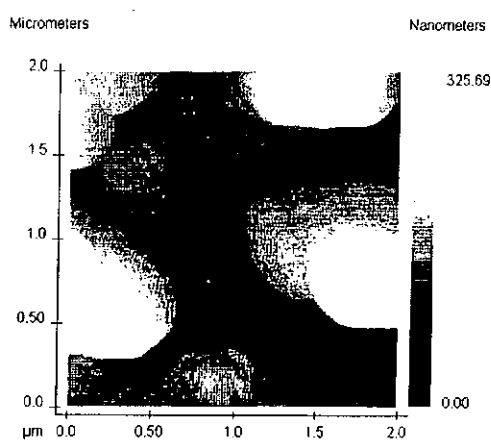
Figure 4.12(c) AFM images of KNSBN single layer films with different sol concentration of (i) 0.03 M (ii) 0.06 M (iii) 0.09 M (iv) 0.12 M (v) 0.15 M and (vi) 0.18 M. The scan area is $5\ \mu\text{m} \times 5\ \mu\text{m}$.



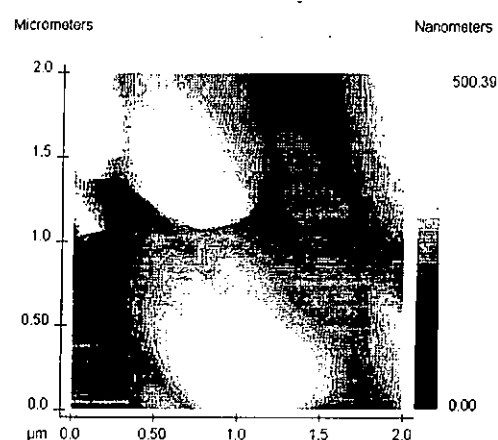
(i) 0.03 M



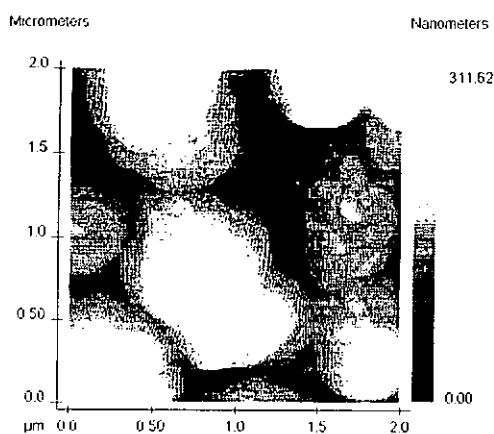
(iv) 0.12 M



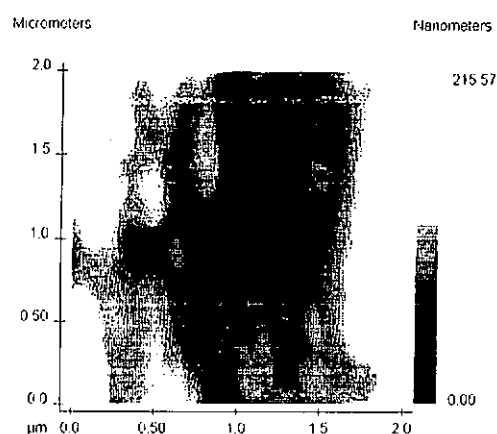
(ii) 0.06 M



(v) 0.15 M



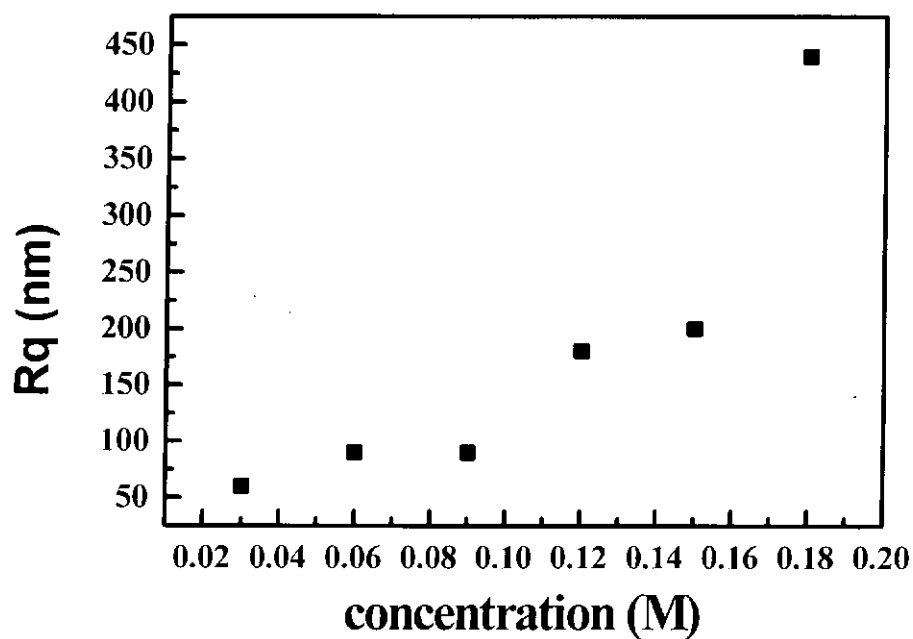
(iii) 0.09 M



(vi) 0.18 M

Figure 4.12(d) AFM images of KNSBN single layer films with different sol concentration of (i) 0.03 M (ii) 0.06 M (iii) 0.09 M (iv) 0.12 M (v) 0.15 M and (vi) 0.18 M. The scan area is $2\ \mu\text{m} \times 2\ \mu\text{m}$.

(a)



(b)

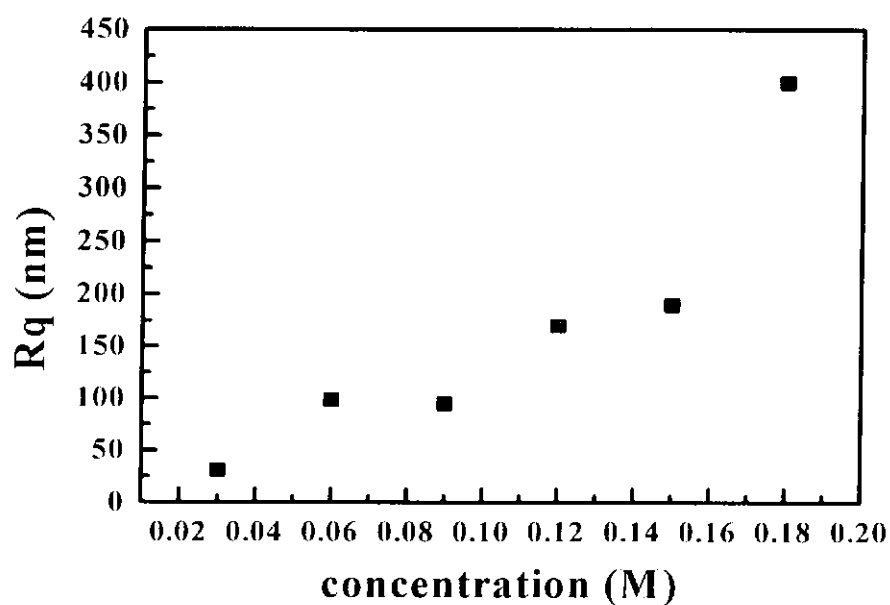


Figure 4.13 The relation between sol concentration and surface roughness. The scan area is (a) $25 \mu\text{m} \times 25 \mu\text{m}$ and (b) $10 \mu\text{m} \times 10 \mu\text{m}$.

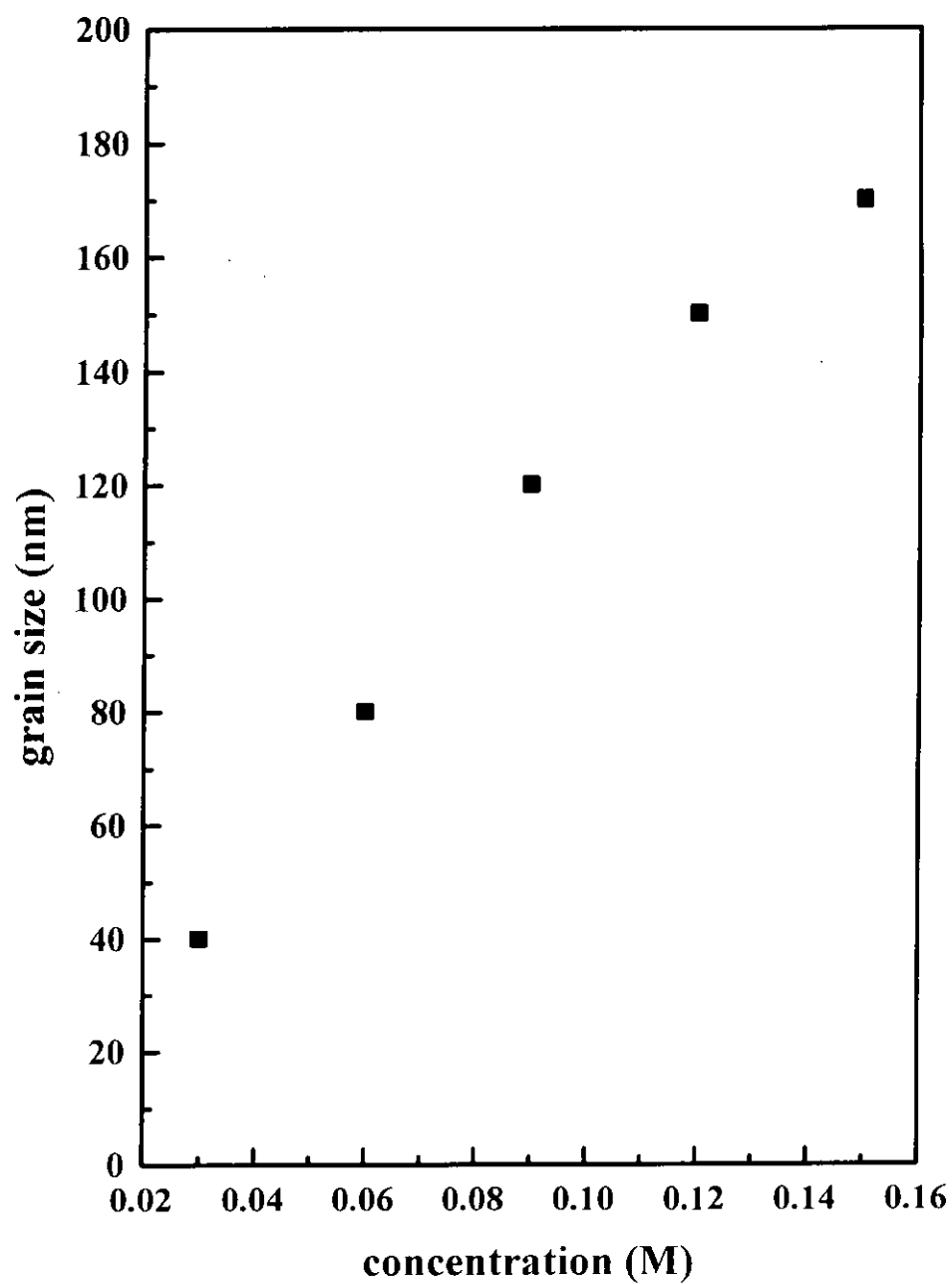


Figure 4.14 Relation between sol concentration and grain size. The data are measured by AFM and based on the scan area of $5\ \mu\text{m} \times 5\ \mu\text{m}$.

Reference 4

- [4.1] C.H. Luk, C.L. Mak and K.H. Wong, "Characterization of strontium barium niobate films prepared by sol-gel process using 2-methoxyethanol". *Thin Solid Films*, 298, pp.57-61 (1997).
- [4.2] Melanie M.T. Ho, C.L. Mak and K.H. Wong, "Raman Scattering and X-ray Diffraction Investigations of Sol-Gel Derived SBN Powders". *Journal of European Ceramic Society*, 19, pp.1115-1118 (1999).
- [4.3] Hyo Seok Joo, Yu Min Kim, Heegang Ryoo and Gwangseo Park, "The dielectric properties of $(K_xNa_{1-x})_2(Sr_yBa_{1-y})Nb_{10}O_{30}$ ". *New Physics (Korean Physical Society)*, 32, number 4, pp. 570-574 (1992).
- [4.4] E. Amzallag, T.S. Chang and R.H. Pantell, "Raman scattering by $Sr_xBa_{1-x}Nb_2O_6$ ". *Journal of Applied Physics*, 42, pp.3254 (1971).
- [4.5] Jih-Mirn Jehng and Israel E. Wachs, "Structural Chemistry and Raman Spectra of Niobium Oxides". *Chemistry Materials*, 3, pp.100-107 (1991).
- [4.6] Y. Replin, E. Husson and H. Brusset, "Etude par spectroscopies d'absorption i.r. et de diffusion Raman des composés $A''B_2^V O_6$ de structure de type "blocs 1×2 "---I. Etude du niobate de baryum $BaNb_2O_6$ ". *Spectrochimica Acta*, 35, pp.937-948 (1979).
- [4.7] H.R. Xia, K.X. Wang, B.Y. Zhao, C.H. Chen, X.L. Lu, Q.Z. Jian, P.J. Sun, and L.J. Hu, "Study of Raman spectra for ferroelectric tungsten bronze-type crystals SBN and KNSBN". *Acta Physica Sinica*, 45, pp.232-237 (1996).
- [4.8] Shin-ichi Hirano, Toshinobu Yogo, Ko-ichi Kikuta and Ko-ji Ogiso, "Preparation of Strontium Barium Niobate by Sol-Gel Method". *Journal of American Ceramics Society*, 75 [6], pp.1697-1700 (1992).
- [4.9] Geoffrey K.H. Pang, C.H. Luk, C.L. Mak and K.H. Wong, "Fabrication and Structural Properties of Sol-Gel $Sr_{0.4}Ba_{0.6}Nb_2O_6$ (SBN60) Films", *Ferroelectrics* (in printed).
- [4.10] C.L. Mak, C.H. Luk and K.H. Wong, "Thickness dependence of the structural properties of sol-gel derived $SrBaNbO$ films", *Thin solid films*, 325, pp.79-82 (1998).

Chapter 5

Optical Characterisation

5.1 The optical properties of sol-gel derived KNSBN films

In order to study the effects of sol concentration on the optical properties of our sol-gel KNSBN films, variable angle spectroscopic ellipsometry was employed. The object of ellipsometric measurement is to measure the ratio of the complex Fresnel reflection coefficient, ρ , where

$$\rho = \frac{r_p}{r_s} = \tan \psi \, e^{i\Delta} \quad (5.1)$$

The quantity r_p (r_s) is the Fresnel reflection coefficient for light polarized parallel (perpendicular) to the plane of incidence, and ψ and Δ are the traditional ellipsometric angles.

In our experiment, spectroscopic phase modulated method was used. In this method, the incident arm consisted of a light source and a polarizer. After reflection on the sample, the emerging beam went through an modulator, an analyzer and a monochromator before detection. The respective orientation of the polarizer, modulator and analyzer, referred to the plane of incidence, here are respectively denoted P, M and A. The photoelastic modulator consisted of a fused silica block sandwiched between piezoelectric quartz-crystals oscillating at the frequency of ~50 kHz. This generated a periodic phase shift $\delta(t)$ between orthogonal amplitude components of the transmitted beam. The detected intensity, in this case, would take the general form [5.1];

$$I(t) = I[I_0 + I_s \sin \delta(t) + I_c \cos \delta(t)] \quad (5.2)$$

where

$$I_0 = 1 - \cos 2\psi \cos 2A + \cos 2(P - M) \cos 2M(\cos 2A - \cos 2\psi) + \sin 2A \cos \Delta \cos 2(P - M) \sin 2\psi \sin 2M \quad (5.3)$$

$$I_s = \sin 2(P - M) \sin 2A \sin 2\psi \sin \Delta \quad (5.4)$$

$$I_c = \sin 2(P - M)[\sin 2M(\cos 2\psi - \cos 2A) + \sin 2A \cos 2M \sin 2\psi \cos \Delta] \quad (5.5)$$

and I being a constant. For a suitable choice of angle A , M and P , a simple determination of the ellipsometric angles from I_0 , I_s and I_c could be obtained.

In our experiment, we set

$$P - M = +45^\circ ; M = 0^\circ \text{ and } A = +45^\circ \quad (5.6)$$

$$\begin{aligned} I_0 &= 1 \\ \text{so } I_s &= \sin 2\psi \sin \Delta \\ I_c &= \sin 2\psi \cos \Delta \end{aligned} \quad (5.7)$$

Therefore, by obtaining the I_s and I_c , we could calculate ψ and Δ .

Figure 5.2(a) to (f) show the I_s and I_c dispersion curves for single-layer KNSBN films with different sol concentration. Spectroscopic ellipsometry (SE) measurements were performed at a 70° angle of incidence over the spectral range from 2 to 4.5 eV (620 nm to 275 nm) with 50 meV spectral resolution. General speaking, the samples present an inhomogeneity in the perpendicular axis to the substrate. The best fits of ellipsometry data are obtained by linear graded sample structure using double amorphous model. Based on this model, we assume that the film consists of two layer i.e. upper and bottom KNSBN layer. Shown in figure 5.1 is the fitting model used in the SE spectral analysis.

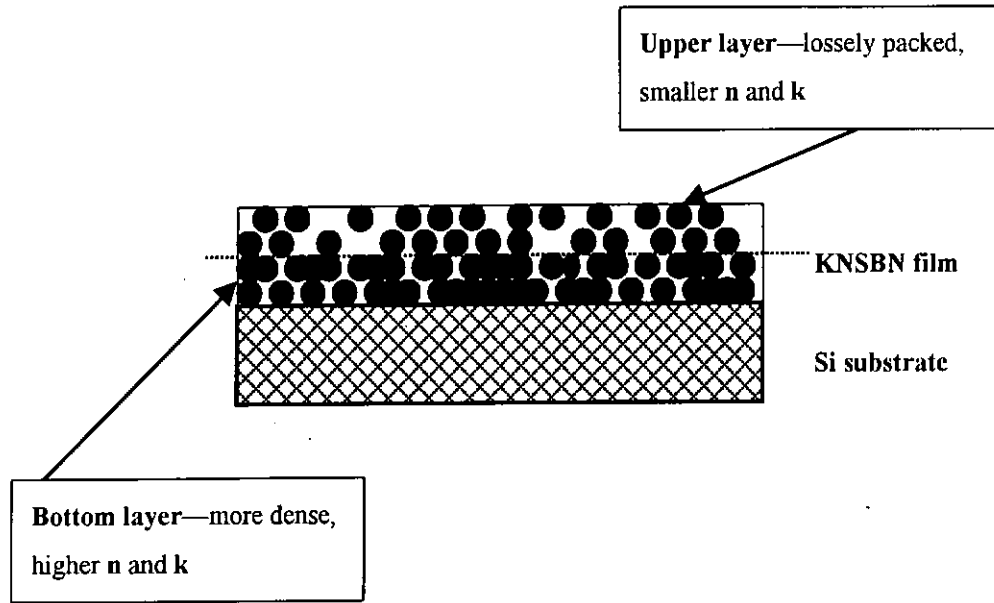


Figure 5.1 The fitting model of KNSBN film used in the SE spectral analysis.

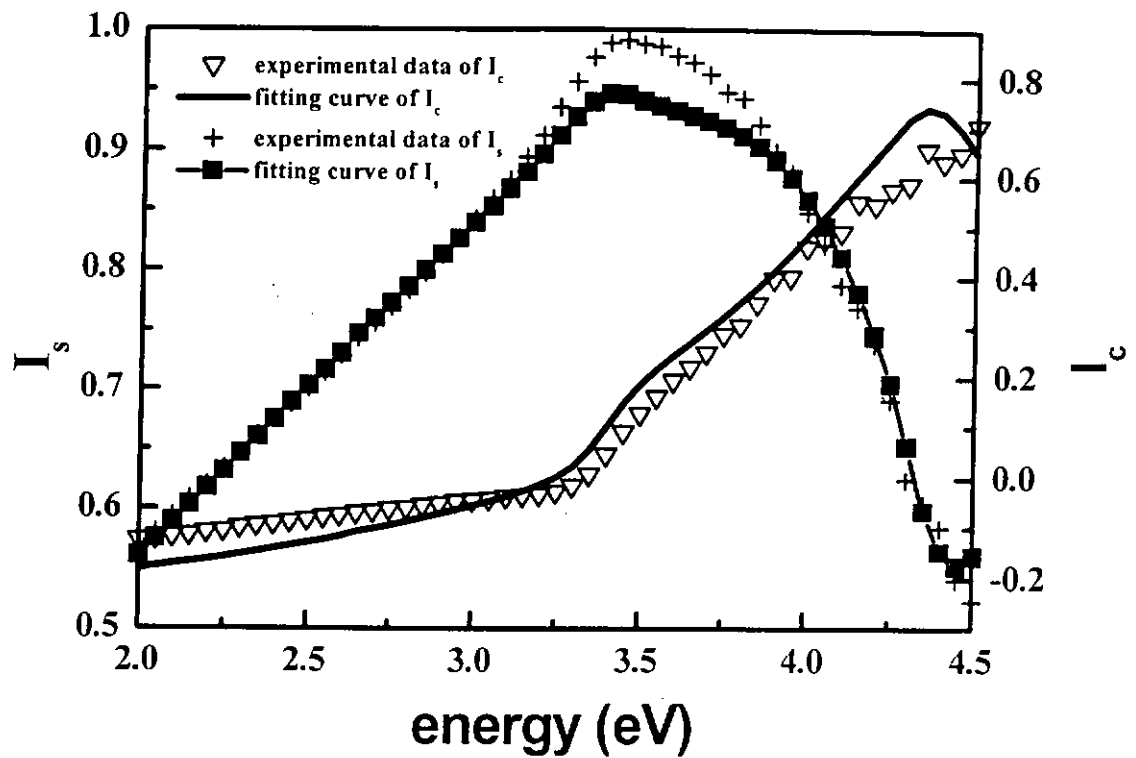
For amorphous model, the following dispersion relations are used

$$K(E) = \frac{A(E_g - E)^2}{E^2 - BE + C}$$

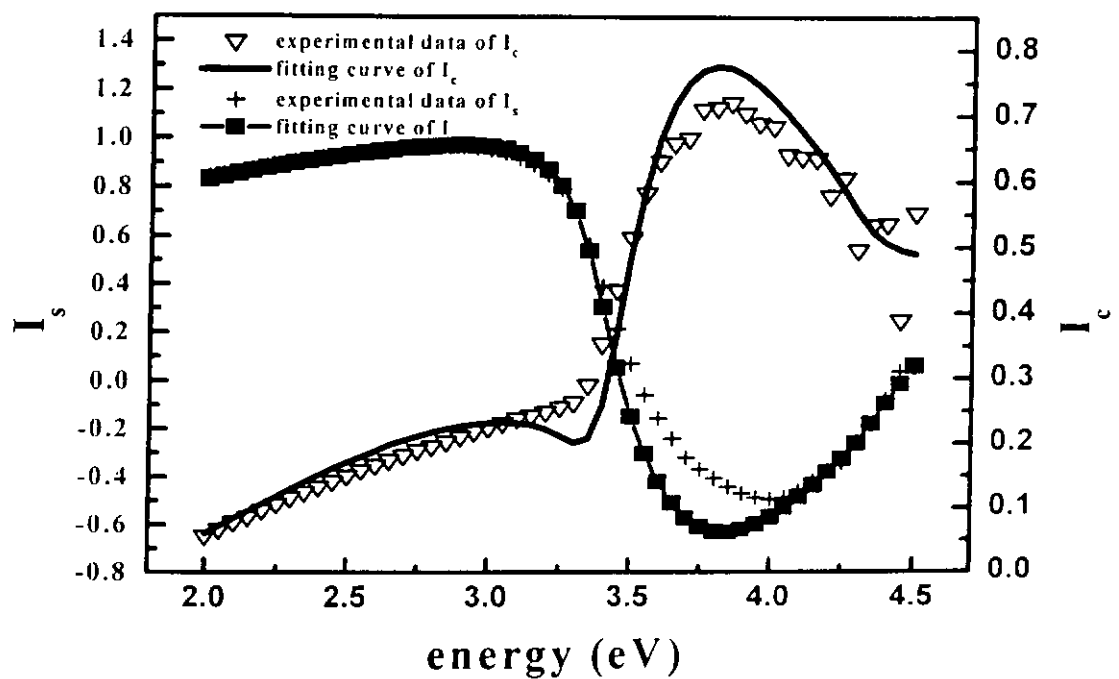
$$n(E) = n(\infty) + \frac{A(-B^2E + 2E_gBE - 2E_g^2E + 2CE + E_g^2B + BC - 4E_gC)}{\sqrt{4C - B^2(E^2 - BE + C)}} \quad (5.8)$$

The five-fitted parameters are the gap E_g , the refractive index at infinity $n(\infty)$ and positive constants A , B and C . We have fitted the optical constants according to the five-parameter model. Figure 5.3 and Figure 5.4 show the dispersive curves derived from the model stimulation of n and k for KNSBN films of different sol concentration respectively.

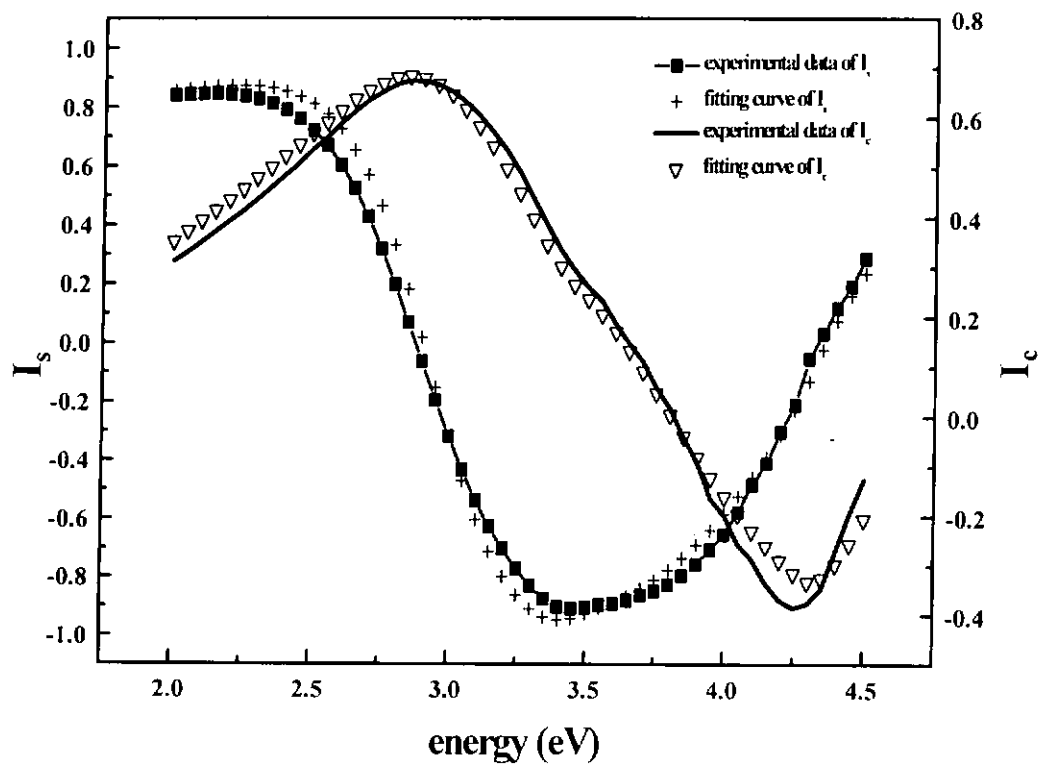
(a)



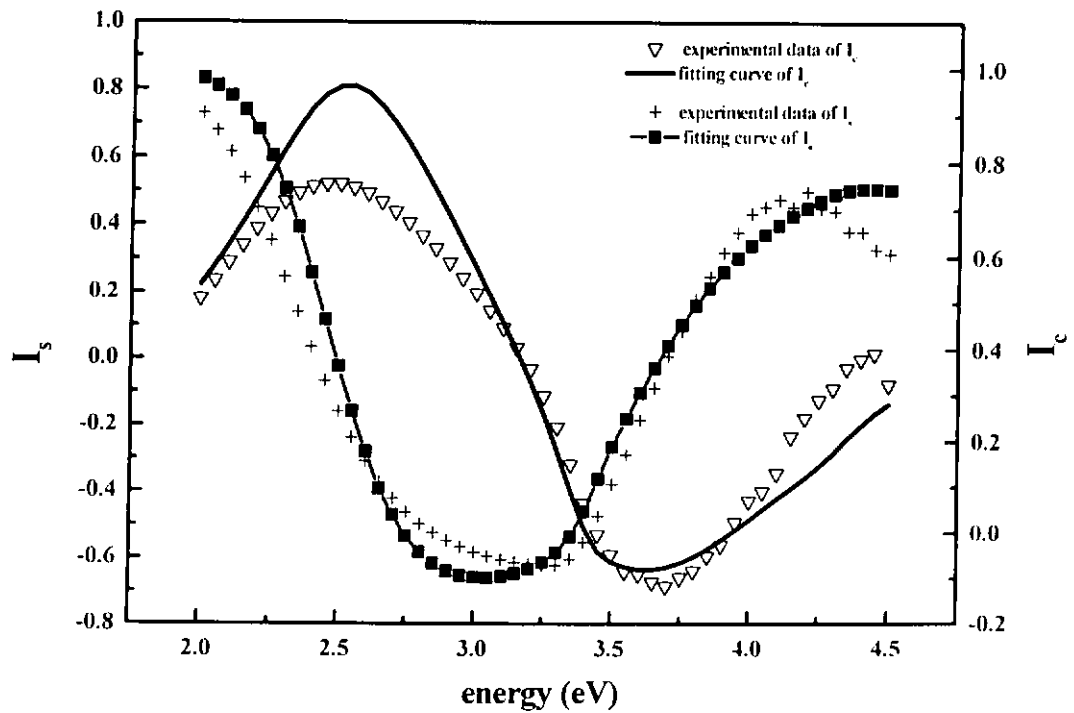
(b)



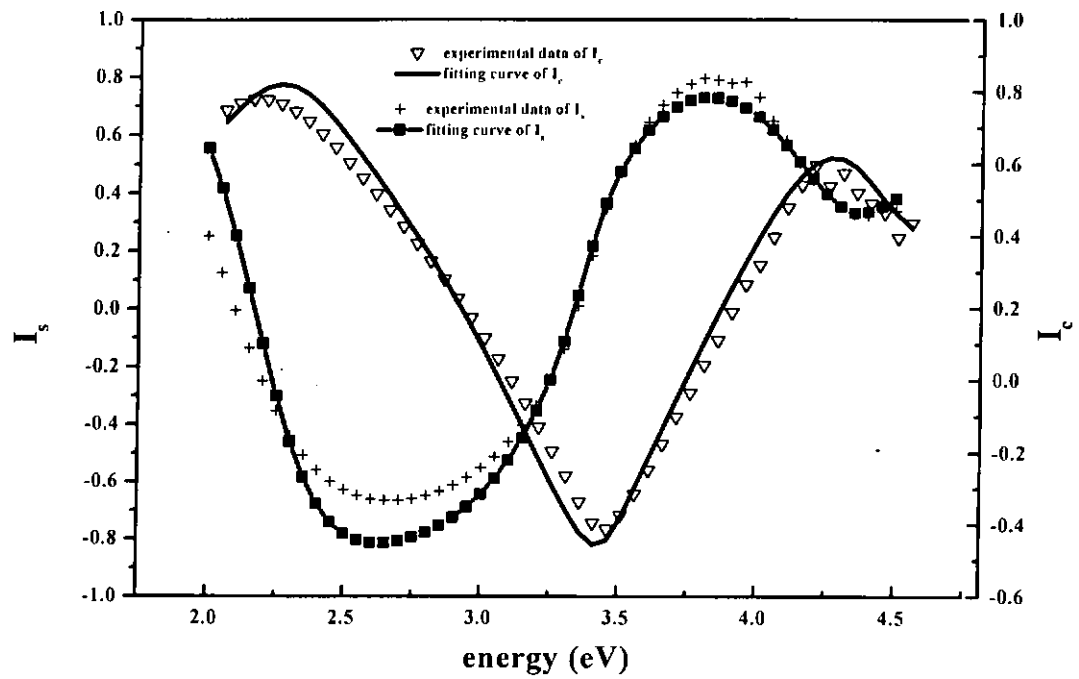
(c)



(d)



(e)



(f)

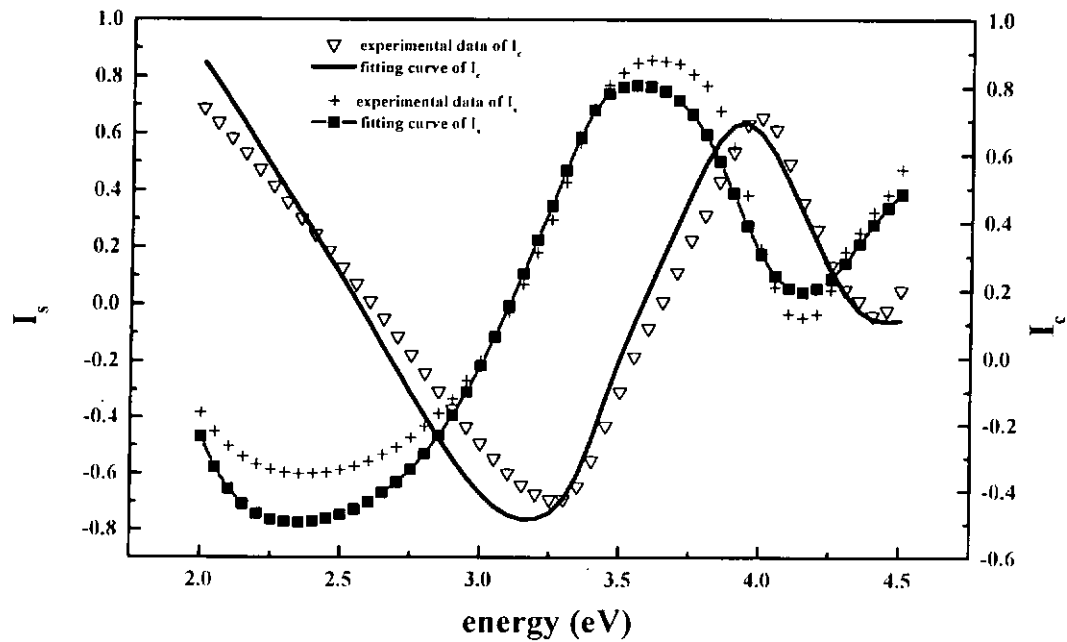


Figure 5.2 The spectra of the ellipsometric parameters I_s and I_c as function of photon energy, obtained from SE experiments for KNSBN films with sol concentration of (a) 0.03M, (b) 0.06 M, (c) 0.09M, (d) 0.12 M, (e) 0.15 M and (f) 0.18 M.

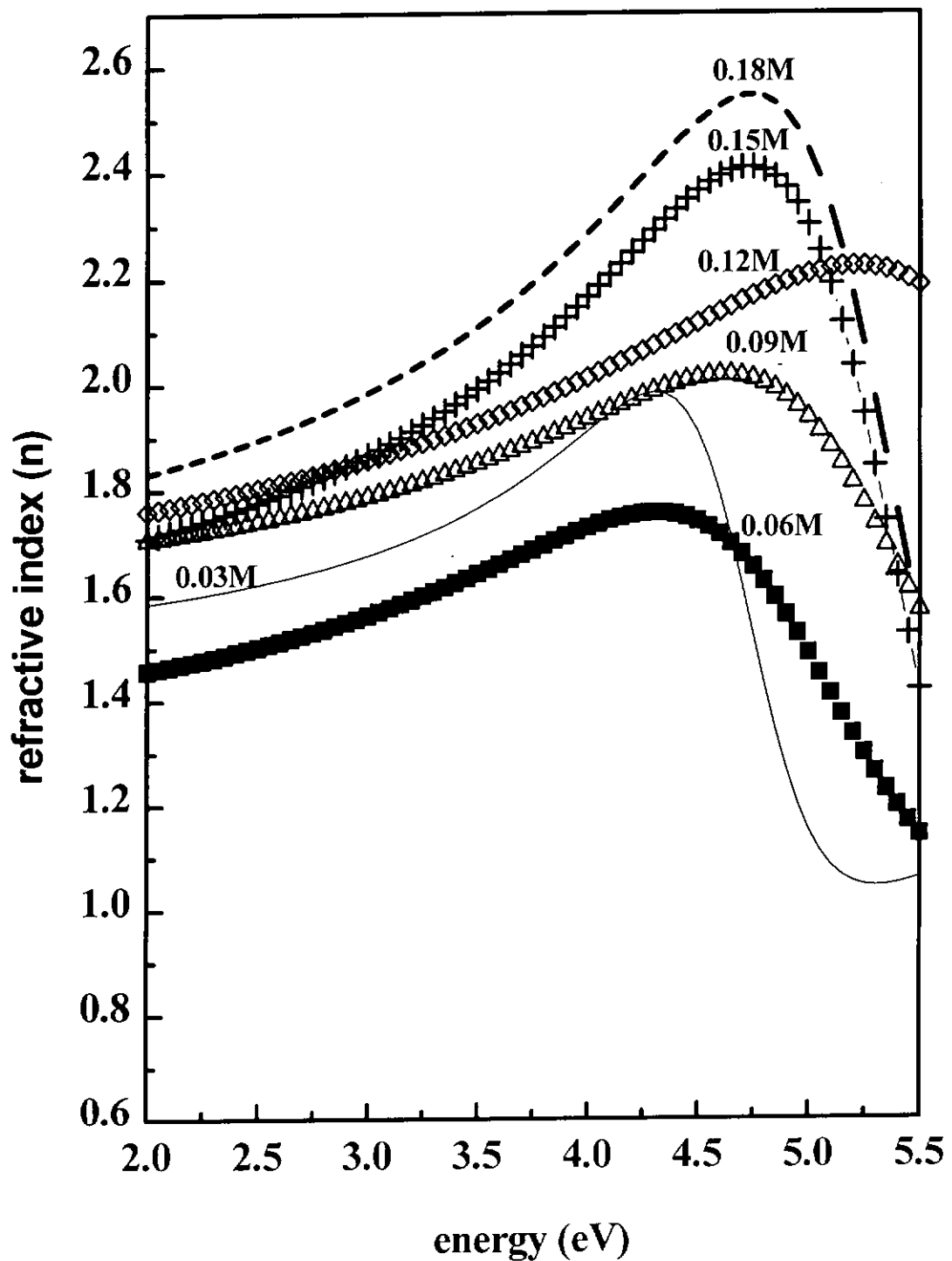


Figure 5.3 The refractive index (n) of the KNSBN films, with sol concentration of 0.03 M, 0.06 M, 0.09M, 0.12 M, 0.15 M and 0.18 M obtained by the two layer amorphous model.

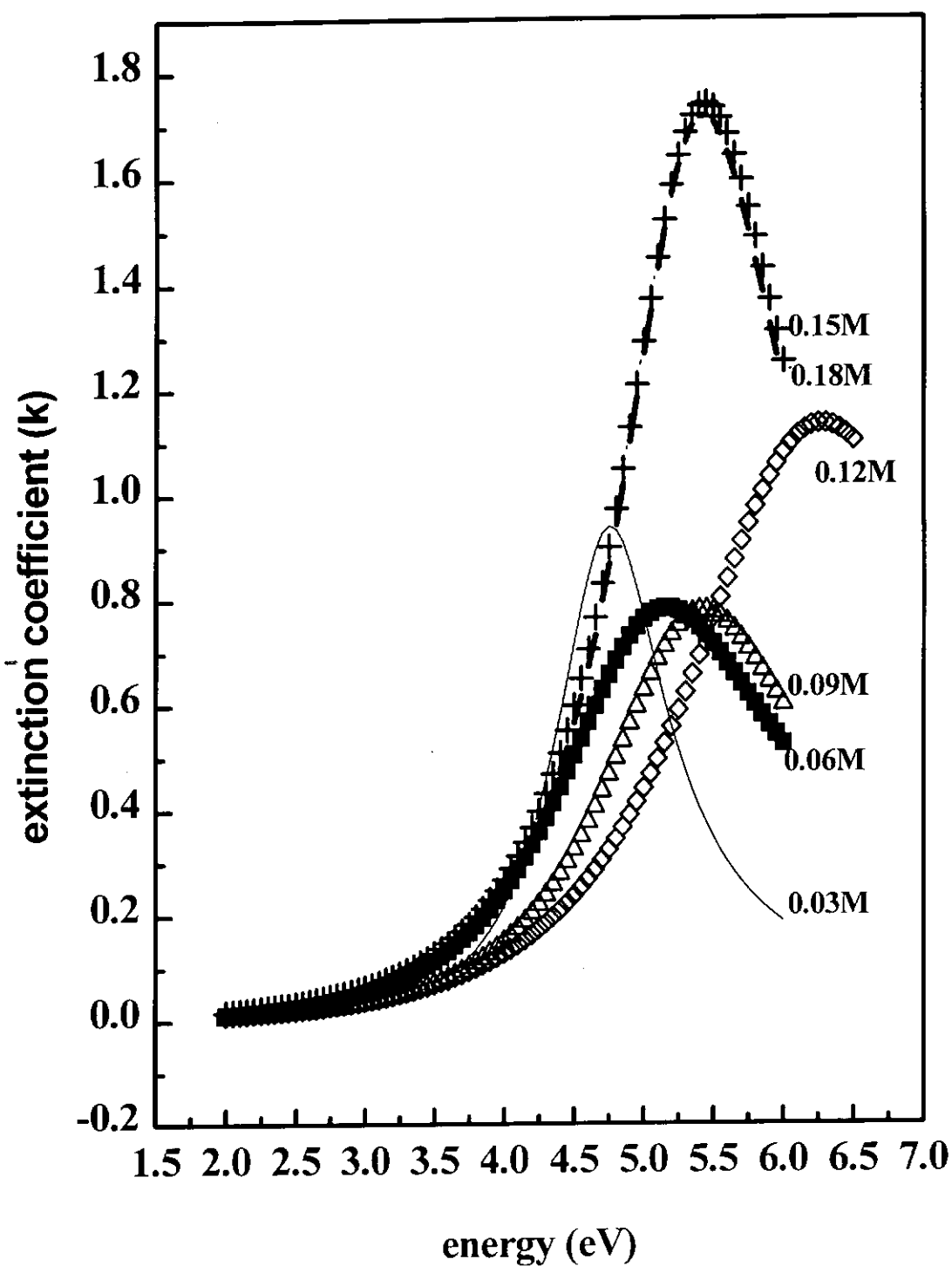


Figure 5.4 The extinction coefficient (k) of the KNSBN films, with sol concentration of 0.03 M, 0.06 M, 0.09M, 0.12 M, 0.15 M and 0.18 M obtained by the two layer amorphous model.

From Figure 5.2, the spectra of I_s and I_c show oscillations which are related to the film thickness. General speaking, the higher sol concentration, the thicker of the film obtained and hence more cycles will be observed in the spectrum. Initially, single layer amorphous model was applied in fitting the data. However, the fitting is not good. Therefore, we modified the single layer model into a double layers model. In this double amorphous model, we assume that the films consist of two layers - a bottom KNSBN layer and a surface layer composed of KNSBN as well as voids. In this model, it was assumed that the inhomogeneity was mainly caused by surface roughness and porosity resulting from the sample preparation. According to the Bruggeman effective medium approximation, a large void fraction leads to a lower refractive index for the upper layer. The void fraction f , effective thickness of surface layer d_2 and bottom layer d_1 , and the other five parameters obtained by amorphous model and EMA models are shown in table 1.

After achieving the fitted parameters, both n and k were stimulated from equation 5.8. Figure 5.3 and 5.4 shows the n and k dispersion spectra for the bottom KNSBN layers of different sol concentrations. In general, the refractive indices of the KNSBN films increase with energy and peak at about 4.5 eV. For example, the refractive index of 0.06 M sample rises from 1.46 (at 2.0 eV) to 1.75 (at 4.4 eV), and then decreases to 1.56 when the photon energy is 5.5 eV. As the sol concentration increases, the spectra shift upward while the maximum shifts to high photon energy. For instance, when the sol concentration is risen to 0.18 M, the peak occurs at 4.8 eV. The escalation of n with higher concentration may be a result of denser films. In addition to the refractive index, the extinction coefficient k was also determined. Figure 5.4 plots the extinction coefficient of different sol concentrations versus photon energy. As the sol concentration increased, the absorption edge moved to higher energy indicating that the transparent ranges of the KNSBN films with higher sol concentration is wider than those with lower one.

From our fitting, we see that both the ratio of thickness of surface layer/bottom layer and the void percentage increase with the sol concentration. These results indicate that the roughness of the films increases when the sol concentration increased. Similar results can be obtained when atomic force microscopic was used for analysis of the films' roughness (Figure 4.13). We clearly observed that the root mean square surface roughness R_q increased with the sol concentration which is consistence with our ellipsometric analysis.

Figure 5.5 plots the relation between the fitted films' thickness and sol concentration. The fitted results were compared with those measured by surface profiler. Obviously, the thickness of the film, as expected, increases with the sol concentration. The two sets of data are comparable to each other. However, the discrepancy seems to be increased as the film thickness increased.

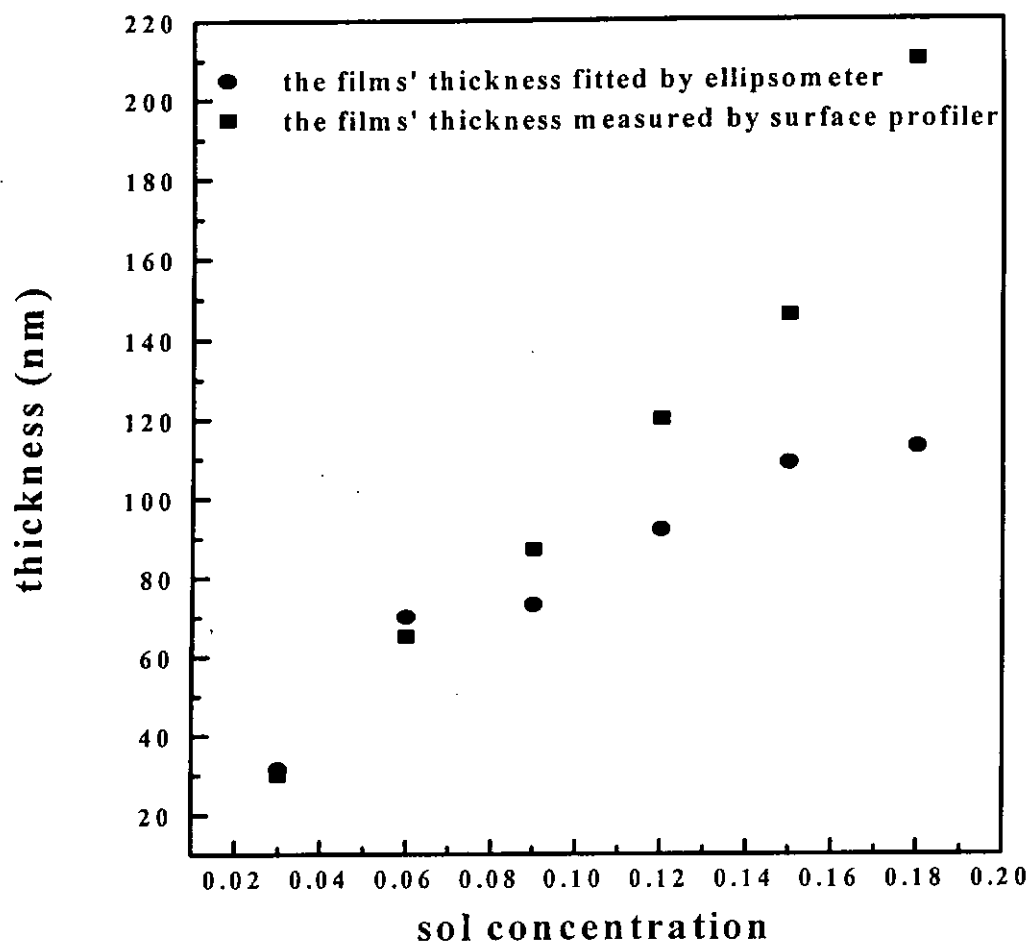


Figure 5.5 The relation between sol concentration and the fitted thickness of the films.

Reference 5

- [5.1] R. Benferhat, " Design of a new in situ spectroscopic phase modulated ellipsometer", ISA Jobin-Yvon, 16 rue du Canal, 91163 Longjumeau Cedex, France.

C h a p t e r 6

Conclusions

6.1 Conclusions

In this project, we have identified a sol-gel route using new recipe in preparing KNSBN sol. The use of methoxyethanol eliminates some major difficulties in the fabrication of the sol-gel KNSBN films using ethanol as solvent. Previously, ethanol was used as the solvent for preparation of metal alkoxides. For example, the formation of the strontium ethoxides from strontium metal and ethanol took a long time to complete. Besides, these ethoxides sol required careful handling because of their readiness to hydrolysis during exposure to air and a chelating agent was needed to stabilize the sols. In this work, we have shown that methoxyethanol is a superior solvent in minimizing these problems. As a result, high quality KNSBN powders as well as films were fabricated using methoxyethanol as solvent. High degree of crystallinity in tetragonal phase was obtained in both powders and films.

KNSBN powders starts to crystallize at 600 °C and is fully converted into TTB phase structure with temperatures higher than 1000 °C. On the other hand, KNSBN films can be crystallized at a lower temperature of ~500 °C. while its orthorhombic-tetragonal phase transition temperature (annealing temperature required for fully convert into TTB phase) occurs at ≥ 600 °C. In comparison, these temperatures are lower than those of SBN by 50 °C.

In addition to the temperature, the effect of the number of dip-coated layer, which is related to the film thickness, is also studied. In these studies, we found that the surface roughness as well as the grain size increases with the film thickness. This roughness is a result of the multi-dipping process. In order to minimize the roughness, layer-by-layer growth method is preferred.

Besides the temperature and film thickness effect, we also measured the effects of sol concentration on the surface morphology of sol-gel derived KNSBN films. In these studies, we found that both the surface roughness and the grain quality of these films depend on the sol concentration. As the sol concentration increases, the surface roughness increases. When the sol concentration is low enough, small and uniform spherical grains are formed with no apparent grain agglomeration. However, when the sol concentration used is higher than 0.18M, micro-cracks are observed on the surface of the films. So, films with smaller sol concentration have a smoother surface with a lesser surface roughness. This indicates that in order to fabricate high quality film with smooth surface, low sol concentration should be used.

Beside the surface morphology, the effects on the optical properties as a function of sol concentration were also studied using variable angle spectroscopic ellipsometry. From single layer KNSBN films with different sol concentration, a remarkable result is gained from their thickness-inhomogeneity relation. In general, the single layer film consisted two sub-layers: the upper layer which composed of KNSBN and void, and a bottom layer which composed of KNSBN only. The upper layer had a smaller refractive index and extinction coefficient than that the of the bottom layer indicating that the bottom layer has a larger degree of crystallinity. This may be due to the substrate effect. Also, we notice that as the sol concentration increased, the refractive indices as well as the extinction coefficients of KNSBN

films increased. However, the values of all our films are smaller than that of the single crystal KNSBN. That means the density of our films is less than that of single crystal.

6.2 Suggested Further Work

Although several processing parameters have been studied in order to optimize the fabrication process of KNSBN, there are still a lot of different processing parameters to be studied. For example, (i) the heating rate of the annealing process which affect the grain size of the samples, (ii) choice of substrate because different substrate will lead to different degree of lattice matching, (iii) composition which affects the physical properties of the KNSBN and (iv) acidity of the prepared sol which affect the hydrolysis as well as condensation rate.

Another direction of studying on these KNSBN films is to measure their electrical and ferroelectric properties (like Currie temperature, spontaneous polarization, etc.). These data are essential for device applications (e.g. electro-optical devices). Also, some optical spectra such as FTIR spectra can also be determined. They can be used to compare with the Raman spectra for studying the symmetric and anti-symmetric structural property of KNSBN. Measuring their non-linear optical properties is also necessary before their application in optical devices. Besides, transmission electron microscopy will be a useful tool to monitor the interfacing structure of the films.